Sensing and Actuation in Monolithic Electroactive Elastomeric Bodies

by

Richard James Morrin Ellingham

A thesis submitted for the degree of
Doctor of Philosophy

in

Mechanical Engineering

at the

UNIVERSITY OF CANTERBURY

September 2024

Declaration of Authorship

I, AUTHOR NAME, declare that this thesis titled, 'Sensing and Actuation in Monolithic Electroactive Elastomeric Bodies' and the work presented in it are my own. I confirm that:

- This work was done wholly or mainly while in candidature for a research degree at this University.
- Where any part of this thesis has previously been submitted for a degree or any other qualification at this University or any other institution, this has been clearly stated.
- Where I have consulted the published work of others, this is always clearly attributed.
- Where I have quoted from the work of others, the source is always given. With the exception of such quotations, this thesis is entirely my own work.
- I have acknowledged all main sources of help.
- Where the thesis is based on work done by myself jointly with others, I have made clear exactly what was done by others and what I have contributed myself.

Signed:

Date:

"When do you think you can submit your thesis?"

T. Giffney, April 2024

"Today."

R. Ellingham, September 2024

UNIVERSITY OF CANTERBURY

Abstract

College of Engineering
Mechanical Engineering

Doctor of Philosophy

by Richard James Morrin Ellingham

Some of the world's most advanced technology is rigid due to various factors such as; manufacturability, miniaturisability, physical linearity, and more ideal physics in general. In parallel industries is also looking to use automation to improve and replace laborious tasks whether they be domestic, commercial, or industrially related tasks. Their is a growing need for new innovations in technology to utilise the soft robotic solutions that mimic biological solutions seen in nature. This thesis is part of many to improve an understanding of the electroactive polymer subset of soft robotics and the limitations of specific implementations of artificial skin and artificial muscle technologies.

This thesis explores the integration of Electrical Impedance Tomography (EIT) with advanced soft sensing technologies, focusing on carbon black silicone rubber (CBSR) elastomer composites and Dielectric Elastomer Actuators (DEAs) to enhance pressure mapping, strain sensing, and actuation.

CBSR elastomer composites, noted for their high stretchability and biocompatibility, were investigated to understand their resistance relaxation behavior. This research contributes to optimizing the design of flexible dynamic strain sensors by modeling the response of resistance to transient strain inputs. The study developed an EIT-based pressure mapping system using a silicone CB nanoparticle sensing domain that mimics pressure mapping qualities human skin. This system was evaluated for its spatial and temporal resolution, showing potential for creating artificial pressure-sensitive skin with practical applications. Furthermore, the integration of EIT with DEAs was examined to improve the mapping of compressive forces across electrode surfaces. Despite some trade-offs in accuracy due to electrode compliance, this approach offers promising advancements for applications requiring precise actuation and pressure mapping. This work has majorly contributed towards filing a patent for an DEA-EIT actuator-sensor device. Additionally, the research uncovered unintentional power generation in DEAs, which could function as Dielectric Elastomer Generators (DEGs) due to mechanical strain. This finding highlights the dual functionality of DEAs and suggests opportunities for energy harvesting applications. Finally, a portable, low-cost EIT-based hardware system for pressure mapping was introduced. This system enables comprehensive characterization of various sensing domains and supports advancements in EIT-based soft sensor technology, with implications for biomedical devices, robotics, and energy harvesting.

Overall, this research advances the field of soft sensors by integrating EIT with innovative materials and technologies, providing new insights and applications in dynamic sensing and actuation.

Acknowledgements

People to thank:

- UC Bioengineering office - Lung lads, Lung Ladies, IPC, Hamish for infinite beers, Nic's abstract art.
- Geoff Chase - for a constant stream of stories and advice always within earshot.
- Other office - for ping pong madness, bikkies and fruit.
- Supervisor Tim - for time, money, lack of time, and support on a project that slightly diverged from his research till the end.
- Co-supervisors Chris, and late comer Lui - for advice and casual yarns.
- Summer students Toby and Yeni - for great work towards my PhD topic.
- UC mechanical and electrical department technicians (Julian Murphy, Julian Phillips, Tony Doyle, Scott Lloyd, amongst others) - for general support and yarns throughout my maddness.
- Juan Jose and Anastasia at IMDEA Materiales - for help with me going down a wonderful materials science rabbit hole.
- Markus Vorrath and co. at TU Dresden - for giving me a home to type out words and a group to discuss soft robotics with.
- Johannes Mersch - For helping with some final (hopefully groundbreaking) experiments when I was in strife towards the end of my PhD.
- Tess - for general oddities, support, and love.
- Friends - for constantly questioning "so when are you finishing again?"
- Family - for being supportive.

Contents

List of Figures

(a) z_{ce} = 0.5 mm 80

(b) z_{ce} = 1 mm 80

(c) z_{ce} = 2 mm 80

(d) Scale 80

(a) z_{ce} = 0.5 mm 81

(b) z_{ce} = 1 mm 81

(c) z_{ce} = 2 mm 81

(d) Load locs 81

(a) z_{ce} = 0.5 mm 82

(b) z_{ce} = 1 mm 82

(c) z_{ce} = 2 mm 82

(d) Load locs 82

(a) V_{DEA} = 3 kV 83

(b) V_{DEA} = 4 kV 83

List of Tables

Abbreviations

ADC	**A**nalog-**t**o-**D**igital **C**onverter
CAD	**C**omputer **A**ided **D**esign
CB	**C**arbon **B**lack
CFA	**C**artesian **F**orce **A**pplicator
CE	**C**ompliant **E**electrode
CoM	**C**enter **o**f **M**ass
DE	**D**ielectric **E**lastomer
DEA	**D**ielectric **E**lastomer **A**ctuator
DEG	**D**ielectric **E**lastomer **G**enerator
DUT	**D**omain **U**nder **T**est
EIT	**E**lectrical **I**mpedance **T**omography
ERT	**E**lectrical **R**esistance **T**omography
FEA	**F**inite **E**lement **A**nalysis
FEM	**F**inite **E**lement **M**odelling
FPC	**F**lexible **P**rinted **C**ircuit
IDF	**I**oT **D**evelopment **F**ramework
MUX	**M**ultiplexer
PCB	**P**rinted **C**ircuit **B**oard
PCBA	**P**rinted **C**ircuit **B**oard **A**ssembly
PDMS	**P**oly**dim**ethyl**s**iloxane (AKA silicone)
PNEC	**P**iezoresistive **N**anoparticle **E**lastomer **C**omposite
SMU	**S**ource **M**easure **U**nit
SMD	**S**urface-**M**ount **D**evice
SR	**S**ilicone **R**ubber
THT	**T**hrough-**H**ole **T**echnology

Symbols

A	Area	[m^2]
C	Capacitance	[F]
ε	Permittivity	[Dimensionless]
K	Bulk Modulus	[Pa]
ν	Poisson's Ratio	[Dimensionless]
Q	Electrical Charge	[C]
U_E	Electrical Potential Energy	[J]
U_ϵ	Elastic Potential Energy	[J]
R	Resistance	[Ω]
σ	Stress	[Pa]
S	Strain	[Dimensionless]
V	Voltage	[V]
Y	Young's Modulus	[Pa]
z	Thickness	[m]

Dedicated to tinned baked beans in all their glory…

Chapter 1

Introduction and Motivation

Rigid robotic systems often have multiple rotary motors and various sensors integrated together for precise control of the robot, this is mirrored in biology with the animals having many actuator units in the form of muscles and a multitude of various receptors for sensing their environment. The rigidity of rotational motors is stifling creativity in the creation and development of devices amongst many other unforeseen future technology. Engineers are often constrained to solving problems and designing solutions using typical rigid sensors and actuators due to their current ubiquity and their evolved increased efficiency. With the rise of research into soft sensor and actuator devices, these such device need to follow suit of the traditional rigid sensors and actuators and become ubiquitous and viable option for general and specialised engineering design solutions.

This thesis has developed methods and tools for creating and characterising artificial pressure sensitive skin technology. The thesis then continues to explore the integration of this artificial skin technology into an artificial muscle technology. The work in this thesis has ultimately contributed towards a patent for DEA-EIT actuator-sensor technology in a quest to bring this work out of the academic realms into real-world applications.

1.1 Why Go Soft and Not Rigid?

The requirement for soft robotics in general has been driven by the limitations of current rigid robotic solutions to interact with natural organic material. Manipulation of natural organic objects such as animals, plants, fruit, vegetables, and meat have traditionally been handled by humans by hand due to our ability to use our dexterity and intelligent control systems to ensure minimal undesirable damage. With the advance in in technology in various soft robotic actuators[23–27], sensors[28], and soft robotics control[29, 30]. The use of soft robotics in place of rigid alternatives, amongst other benefits, has the opportunity to be more sustainable by decreasing waste products during fabrication, using biodegrabale or recyclable materials, shelf life, and use of renewable resources[25]. The use of soft robotics brings opportunity of creating devices with a reduced bill of materials size and less moving parts for maintenance. The use of soft robotics in biomedical and aerospace applications is especially desirable due to the difficulties experienced when designing with regular motors in the outer space and near sensitive biological tissue environments such as heat dissipation, lubrication, and mass[31–34].

The most common rigid actuator is the rotary electric motor and the global market was valued at USD 142.2 billion in 2020, with a predicted growth rate of 9.5% until 2032[?]. Although this market is dominated by automobiles which currently require the traditional form of rotary electric motors, growing sectors of this market such as medical, factory automation, and aerospace have potential interest in adopting soft actuator alternatives for the reasons given above. In parallel, rigid strain sensors of types metallic foil and semiconductor, was given a global market value of USD 190.66 million in 2022 with a compound annual growth rate of 3.9% until 2029[?]. Adjacently the pressure mapping global market value, focused mainly on the health sector, was valued at USD 480 million in 2023 with an expected growth rate of 5.1%[? ?]. Many soft actuator technologies could be used in these growing medical, aerospace, factory automation, and agricultural sectors.

Soft robotic actuation can be achieved through various mechanisms including thermal, electrochemical, fluidic, magnetic, and electrostatic. Similarly soft stress-strain sensing can be achieved through various physical principles such as resistive, capacitive, magnetic, and optical sensing methods. Often the function of soft actuators can be inverted such that the deformation of the actuator can produce a signal used for self sensing, in electroactive polymer (EAP) technologies such as dielectric elastomer actuators (DEAs)[35–38] and ionic polymer-metal composites (IPMCs)[39]. EAPs have the benefit of electronic control over other soft actuator and sensor technologies controlled by fluids, heat, or light which contain the complexity of another energy transfer process.

Proprioception in artificial muscle technology has been made a reality. This is seen in the self-sensing of one dimensional strain of DEAs usually through capacitive measurement between the compliant electrodes during operations to obtain the magnitude of a contraction. However, the pressure mapping done similar to the mechanosensation performed by cutaneous mechanoreceptors on an artificial muscle device has not been explored as of writing this thesis.

Publications towards this thesis include three conference papers, one journal paper, and one provisional patent filed. This thesis has converged on the use of conductive particle based elastomer composites and their use in sensors and actuators, in particular an electrical impedance tomography (EIT) based artificial skin and it's integration into the artificial muscle technology, dielectric elastomer actuators. The composite type used throughout the thesis is simple to fabricate but not well understood in terms of its electromechanical transient and dynamic characteristics. The modelling of such conductive particle composites would elucidate the feasibility of inverting the model to create a responsive strain sensor. This composite has been characterised in one-dimension several times in literature already however, if a two dimensional sensing application of this composite is desired the characterisation of the sensor in two dimensions must be completed. A method to do such 2D sensing is using EIT. EIT has been used in the past for a huge range of applications, with few exploring the use of EIT as a pressure mapping sensor. Although EIT-based pressure mapping was first discovered 30 years ago, the technology is still in its infancy with several problems needing to be resolved before the technology can be used reliably in real-world applications.

1.2 Research Objectives

The research objectives and questions for this thesis are given below:

1. Quantify and analyse static, dynamic, and transient phenomena seen in conductive particle composites.
2. From the characterisation in objective 1 mitigate the effects of the transient phenomena.
3. Create a set of metrics for quantifying the performance of an electrical impedance tomography based artificial skin.
4. Simulate and integrate an electrical impedance tomography based artificial skin onto a dielectric elastomer actuator.
5. Investigate the energy harvesting of a device that is both a dielectric elastomer actuator and electrical impedance tomography device.

1.3 Chapter Contributions

Chapters 3 - 8 contain the core novel research contributions. Chapters 2 and 9 provide essential background knowledge and future research directions for the thesis respectively.

Chapter 2 - Literature Review: This chapter explores the nature of biological skin and muscle from an engineering perspective, quantifying necessary functions and properties desired to replicate or supersede for their artificial equivalents. The thesis then describes state-of-the-art soft sensors and actuators and their function.

Chapter 3 - A Simple Conductive Elastomer Composite Material with Complex Behaviour: This chapter uncovers the electromechanical tensile and compressive properties of carbon black silicone composites, in order to understand the material before it's use in sensors and actuators.

Chapter 4 - An Improved an Electrical Impedance Tomography Based Artificial Soft Skin Pressure Sensor: This chapter discusses the use of electrical impedance tomography to create a pressure mapping sensor and provides tools for analysing the suitability to various applications and choosing a suitable sensing domain.

Chapter 5 - Giving Artificial Muscles the Sense of Touch: This chapter describes the integration of the pressure mapping technology discussed in the previous chapter, how it can be integrated into dielectric elastomer actuators, and the trade-offs.

Chapter 6 - Unintentional Power Generation in a DEA-EIT Sensor-Actuator Device: This chapter discussed the unintended power generation of the simultaneous sensor actuator device discussed in the previous chapter.

Chapter 7 - A Portable Electrical Impedance Tomography Based Pressure Mapping Sensor and Validation System: This chapter discusses the small form factor, low-cost hardware design for a hybrid artificial muscle - artificial skin based device.

Chapter 8 - ?? Modelling of DEA-EIT Capacitively driven Hybird Sensing and Actuation Device: The is chapter models the a DE-EIT device in order to find an optimal range of parameters at which capacitive shunting can be used to improve the DE-EIT pressure mapping device responsiveness.

Chapter 9 - The Biomimmetic Re-Evolution: This chapter discusses the future direction of the technology discussed in the thesis and acknowledges the future of the broad field of soft robotics.

Chapter 2

Literature Review

To replace and supersede tasks that can currently only be performed by humans due to their dexterity, physical makeup, and intelligence; the skin and muscles completing these tasks can first be understood and quantified. Subsequently a review of various electrically driven artificial skin and muscle technologies was completed. Finally, background theory on piezoresistive elastomer composites and two specific technologies of soft sensing and actuating devices is given to setup a foundational knowledge base and reference for the rest of the thesis.

2.1 Biological Skin form and function

Skin is the largest organ in the human body with many functions, however this thesis only aims to replicate some pressure-sensitive functions of skin. Two pressure-sensitive categories of skin and muscle tissue transducers which allow for dexterous manipulation of objects are:

1. Proprioceptors: respond to internal mechanical stimuli in a joint capsule, tendon, or muscle to give the sense of motion.

2. Cutaneous mechanoreceptors: respond to mechanical stimuli usually external to the body, including pressure and vibration, for the localisation of sensations.

Locations of both proprioceptors and cutaneous mechanoreceptors are shown diagrammatically in Figure 2.1. Proprioceptors aid in determining pose estimates of body parts in space, acting as sensors providing feedback closed-loop control for the neurological motion control of body parts. Whereas cutaneous mechanoreceptors have various roles including object recognition, manipulation control, as well as motion control.

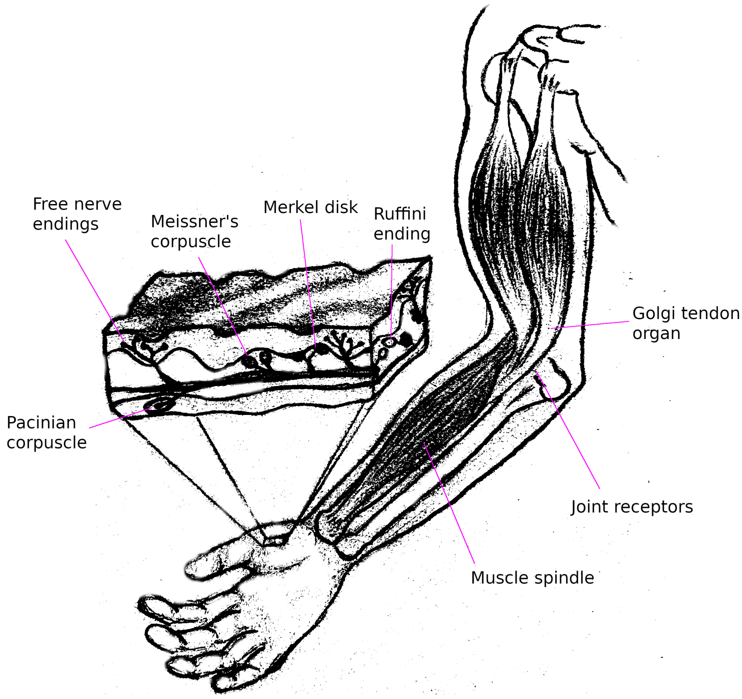

FIGURE 2.1: Examples of the locations of proprioceptors and cutaneous mechanoreceptors in the human body.

The function of both kinds of receptor have been mimicked by certain device technologies. For example proprioceptors have been mimicked in wearables and human assistive devices where joint motion has been estimated by sensors such as rotary/linear encoders, IMUs, and stretch sensors fixed adjacent to joints to calculate pose estimates of limbs[1–4]. Examples of such devices are displayed in Figure 2.2

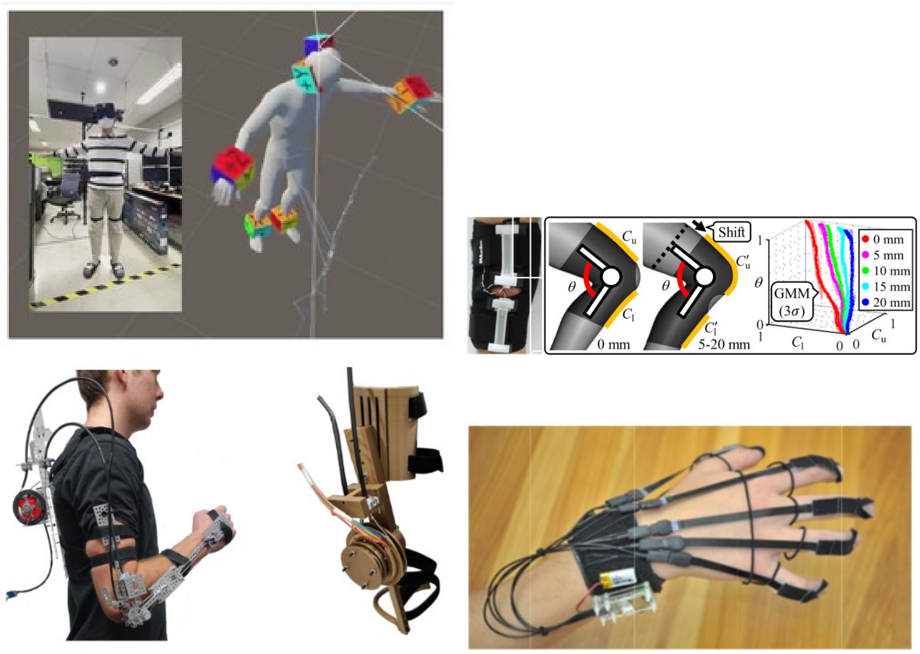

FIGURE 2.2: Clockwise from top left: IMU pose estimation[1], stretch sensor knee joint pose estimation[2], stretch sensor hand joint pose estimations[3], encoder elbow pose joint estimation[4].

Cutaneous mechanoreceptors have been mimicked by the development of pressure mapping of flexible surfaces. Examples of such technologies include, foot pressure based gait analysis, wheelchair seat pressure mapping. Examples of these sensors are shown in Figure 2.3.

FIGURE 2.3: Various pressure mapping devices. From top-left clockwise: Xsensor wheelchair pressure mapping sheet[5], Pressure Profile Systems pressure sensors on a robotic hand[6], Soft pressure mapping gripper[7], Tekscan thin pressure mapping platform[8], Tactilus seat pressure mapping system[9]

Many of these pressure mapping technologies don't accurately mimic desirable qualities of regular biological skin and are specialised for their specific use cases. The following sections quantify characteristics of pressure sensitive skin.

2.1.1 Skin Construction and Types

Skin is a laminate structure consisting of three main layers, the epidermis, dermis, and hypodermis. The top two layers the epidermis and dermis are a subset of the cutaneous layer which contain the majority of the pressure-sensitive mechanoreceptors [].

The skin can be categorised as glabrous/hairless or non-glabrous/hairy. Glabrous skin contains many of the mechanoreceptors given in Figure 2.1 whereas non-glabrous skin will also contain C-tactile afferent receptors for obtaining sensations through hair follicles. However this work is exploring simple monolithic bodies so will not be replicating the sensor function of non-glabrous skin.

Depending on the region of skin different force resolution and spatial resolution will incur. The tensile properties of skin is governed by skin tension lines, also called Lager's lines, which show the direction in which the maximal stretch can occur.

Cutaneous mechanoreceptors and their functions are given in Table 2.1.

TABLE 2.1: Comparison of typical mammalian mechanoreceptors characteristics [22].

Receptor	Meissner corpuscle A1	Ruffini Corpuscle A2	Pancian Corpuscle B1
Perceptual sensory functions	Skin movement, handling objects	Skin stretch, movement direction, hand shape, and finger position	Fine tactile discrimination, form and texture perception
Skin stimulus	Dynamic deformation	Skin stretch	Indentation depth
Localisation	Dermal papillae	Dermis	Basal layer of epidermis / around guard hair
Conduction velocity	35 - 70 m/s	35 - 70 m/s	35 - 70 m/s
Receptive field	22 mm^2	60 mm^2	9 mm^2
Receptor density	150 / cm^2	10 / cm^2	100 / cm^2

2.1.2 Characterising skin

The sensing qualities of skin is crucial for the sensory feedback in complex manipulation tasks. To aid the creations of technology that mimics qualities of biological pressure sensitive skin, the mechanical properties of must be characterised. Biological human skin is highly variable in terms of its mechanical and sensing properties depending on the region of skin, giving large variation in skin characteristics. Skin can be characterised in terms of the following mechanical characteristics:

1. Elastic modulus - The static elastic properties determined by a linear region of stress and strain of the material [Pa]

2. Storage and loss modulus - The dynamic elastic and viscoelastic properties determining the relationship between stress and strain [Pa]

3. Shear modulus - The relationship between the shear stress and shear strain in the linear region of the stress-strain characteristic curve [Pa]

4. Ultimate tensile stress (UTS) - The maximum tensile stress that a material can tolerate before breaking [Pa]

5. Life cycle - The time or number of actuation cycles in which it takes for the actuator to degrade such that it cannot perform its intended purpose to specified standards

6. Viscoelastic creep and relaxation - All viscoelastic materials will experience strain creep and stress relaxation to varying degrees depending on the viscoelastic properties of the material [mm.s^{-1} and s]

7. Skin thicknesses - the thickness of all layers of skin the cutaneous epidermis and dermis and thickness of the hypodermis [mm]
8. Skin surface area - Biological skin has a large surface area and can also be regionalised to map skin function and sensitivity [m^2]
9. Isotropy/Anisotropy - The directionality of skin properties, also known as skin tension lines, give a topological map of the maximal stretch (i.e. minimal elastic modulus) direction of regions of skin.

Some of the functional properties in terms of pressure mapping include:

1. Spatial resolution and touch acuity - The spatial resolution of biological skin, which is mainly dependent on the innervation, mechanoreceptors density, and thickness of the cutaneous layers of skin [40–42]
2. Static force resolution - This is the detection resolution of static or slow-acting forces acting upon the skin [42]
3. Temporal resolution - This is the detection resolution of fast-acting forces acting upon the skin often required for texture recognition [40, 42]

A numerical characterisation of mechanical and pressure sensing functional skin properties include:

1. Elastic modulus - varies largely depending on test method, test skin type, and subject. Values found in literature include 83.3 $\pm$ 34.9 MPa [43], 0.1 - 2.4 MPa [44], and 10.4 - 89.4 kPa [45].
2. Storage and loss modulus - varies largely depending on test method, test skin type, and subject. Values found in literature range include 141.9 $\pm$ 34.8 Pa and 473.9 $\pm$ 42.5 Pa at 0.8 Hz [46], 473.9 $\pm$ 42.5 Pa and 32.3 $\pm$ 10.0 Pa at 205 Hz [47].
3. Shear modulus - Shear modulus has been reported to be 100 times that of elastic modulus for upper most layers of skin (epidermis and stratum corneum) [48]
4. Ultimate tensile stress - 21.6 $\pm$ 8.4 MPa [43]. 28.0 $\pm$ 5.7 MPa [49]
5. Life cycle - Skin cells are constantly growing, dying, and shedding. Skin is always actively remodelling based on external stimuli.
6. Strain creep - The strain creep was found to be 2.7 kPa.s for a 10 Pa step input on a dermis skin sample [46].
7. Stress relaxation -
8. Skin thicknesses - The thickness of human cutaneous skin ranges from 0.6 to 2.6 mm with an average skin thickness of 2 mm [40].
9. Skin surface area - The average surface area of skin in adult humans is 1.7 $\pm$ 0.1 m^2 [40].

10. Isotropy/Anisotropy - The tension lines in skin are determined by collagen fibre orientation and dynamic stretch events [50, 51]. The elastic modulus of human skin was reported to be 160.8 ± 53.2 MPa parallel to the skin tension lines and 70.6 ± 59.5 MPa perpendicular to the tension lines [49]. The UTS of human skin was reported to be 28.0 ± 5.7 MPa parallel to the tension lines and 15.6 ± 5.2 MPa perpendicular to the tension lines [49].

1. Spatial resolution and touch acuity - The tactile field area increases with indentation depth for certain mechanoreceptors with a range of 5 - 12.6 mm^2 [52]. Two point discrimination is another metric for determining spatial resolution an has been determined as 3.7 ± 0.7 mm [53]. The receptive field varies depending on the mechanoreceptors used so has been reported to be between 1 and 60 mm^2 as another methods of inferring spatial resolution [22].

2. Force resolution - Minimum force detection on various regions of human skin was found to be between 67 - 1007 mg [54], and various mechanoreceptors 0.73 - 122.6 mN [55].

3. Temporal resolution - Depending on the mechanoreceptor sensing the force input, a frequencies ranges of 0 to 800 Hz can be perceived by human skin [52]

2.1.3 Skin Modelling

Developing robust mechanical models for human skin is non-trivial for three main reasons:

1. high degree of viscoelasticity
2. regenerates and heals
3. made from various types of cells in a laminate structure

To solve the complexity of modelling such a material a review by Landry et al.[40] shows that many researchers have applied various non-linear mechanical models including Ogden, Mooney–Rivlin, Neo-Hookean, Yeoh, Humphrey, and Veronda–Westmann. When recreating an artificial muscle it is desirable to minimise the mechanical material model complexity so that the material can be more easily integrated into a control system with known behaviour. Similar modelling techniques can be used to model conductive particle elastomer composites due to the similar hyper-elastic and visco-elastic behaviours observed.

2.1.4 Electrical Impedance Tomography

2.1.5 Electric Field Imaging

2.1.6 EIT-based Skins

2.2 Biological Muscle form and function

Note: This section was taken from literature reviews from 3 years ago, when I was going to research DEAs. Needs a re-review ASAP.

Biological muscles are a product of millions of years of evolution and the motion and other mechanical characteristics of biological structures is yet to be outperformed by artificial muscle technology. To determine how to quantify the performance of a biological muscle this section gives foundational knowledge about muscle function, structure, and how it can be characterised from an engineering perspective.

Biological muscle is a naturally occurring tissue comprised of muscle fibres bundled together to apply a contractile force on connecting tissue or, in the case of smooth muscle, applying a force on itself. The base actuator units of muscle are proteins myosin and actin filaments, which effectively slide against each other to produce a contractile motion. The root cause of a muscle contraction is an electrochemical signal sent form the central nervous system to a motor neuron/s which travel to the muscle where electrochemical reactions take place for the contraction to take place. The sliding motion of the myosin

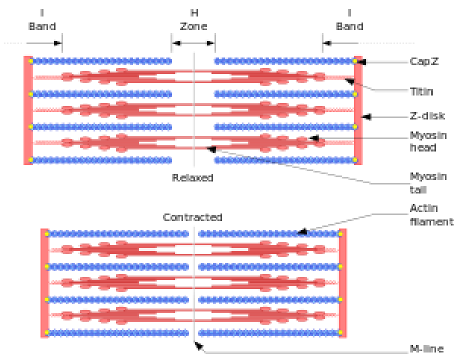

FIGURE 2.4: Components of a biological muscle contractile unit [10]

and actin filaments is due myosin heads attaching to the actin and pulling the actin towards a middle line (M-line) in multiple stroke actions. These filament actuators are stacked in three dimensions within a muscle fibre to amplify contractile stress and strain as shown in Figure 2.4.

The anatomy of a human skeletal muscle can be seen in Figure 2.5. The muscle is made up of bundles of fasicles connected together with a tissue called perimysium. Within the fasicles are many muscle fibres (i.e. muscle cells) which are surrounded by a connective tissue called endomysium. Within the muscle fibres there are many sacromeres stacked within a cyclindrical-like structure called a myofibril. Each sacromere contains a contractile unit of myofilaments.

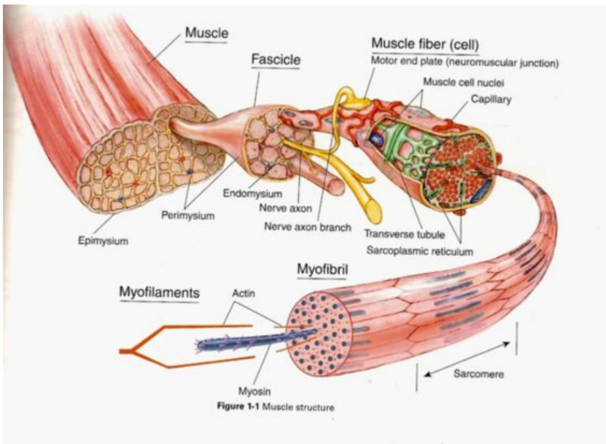

FIGURE 2.5: Diagram of the internal structures of a skeletal muscle[11]

2.2.1 Characterising a muscle

To be able to quantify the performance of a biological muscle there must be certain metrics characterising muscles such that both artificial and biological that can be compared. An artificial muscle can be characterised using typical mechanical material parameters such as:

1. Stress - Force that is applied to the normal of the cross section of the muscle through various states of muscle excitation. $[N.m^{-2} or Pa]$
2. Strain - The muscle change of length due to the stress applied through various states of muscle excitation.
3. Elastic modulus - The elasticity determining the relationship between stress and strain for the linear region of the stress strain characteristic curve. $[Pa]$
4. Shear stress - Force applied parallel with a cross sectional area plane due to a state of muscle excitation. $[N.m^{-2} or Pa]$
5. Shear strain - The change in deformation perpendicular to the direction of loading to the due to a state of muscle excitation.
6. Shear modulus - The relationship between the shear stress and shear strain in the linear region of the stress strain characteristic curve. $[Pa]$
7. Energy density - The work done by the muscle per unit volume or mass. $[J.kg^{-1}]$
8. Power density - The work done by the muscle per unit volume (or mass) per unit time. $[J.kg^{-1}s^{-1} or W.kg^{-1}]$
9. Yield stress - Stress at which the stress strain curve of the muscle begins to become non-linear and the material strain may not return to it's resting (original) length. $[Pa]$
10. Ultimate tensile strength - The maximum tensile stress that a material can tolerate before breaking. $[Pa]$
11. Efficiency - The work done by the muscle compared to the energy put into the system, known as metabolic cost in biological muscles. [%]

12. Actuation frequency - The frequency range of actuation cycles using the system's method of excitation. $[Hz]$

13. Stroke - The maximum displacement an actuator can achieve $[m]$

14. Drift - Change in actuation displacement over time given the same excitation input value each actuation cycle. $[m]$

15. Life cycle - The time or number of actuation cycles in which it takes for the actuator to degrade such that it cannot perform its intended purpose to specified standards.

    As well as commonly used medical/biology muscle metrics such as:

16. Maximum isometric contraction force - the maximum force a muscle can apply without changing strain. This is also related to the ratchet-like mechanism and muscle locking where a muscle can apply a much larger force in a static state, as seen in the myosin binding[57].

17. Muscle force direction and architecture - Biological muscles can have varying contraction force directions determined by pennation angle of the muscle and the muscle fibre configuration.

Other qualities of muscle should be quantified on a case by case basis depending on the artificial muscle technology being investigated. For example, a major issue with dielectric elastomer actuators is the excitation voltage required for actuation is too large for many applications. Hence this could be another parameter considered for some artificial muscles.

Some of the biological muscle metrics have been quantified by previous research as seen below:

- Energy density - Biological muscle can have energy densities ranging from 0.4 - 40 $J.kg^{-1}$[58].
- Power density - Biological muscle can have energy densities ranging from 9 - 284$W.kg^{-1}$[59]
- Actuation frequency - The range of natural actuation frequencies for both vertebrate and invertebrate muscles ranges 1 - 180Hz[59].
- Strain - Biological muscle can have strains ranging from 5-30%[60].
- Efficiency - Thermodynamic efficiency of human muscle is typically between 20-35%[61]. However other biological muscle has been seen to reach efficiencies of up to 77%, such as in tortoises[61].

2.2.2 Muscle Mechanics

Before attempting to recreate a bio-mimetic actuator it is important to acknowledge the numerous simplified electro-mechanical system models of parts of the muscle actuation process. These models need to be understood to gain an understanding of the application of biomimetic actuators can be used in assistive soft robotic devices. From here we will present basics of the subject of bio-mechanics.

The stress and strain involved in muscle contraction is more complex than uniform materials and is non-linear. The stress and strain of a passive muscle (i.e. contractile units are not producing internal muscle tension) can be modelled with the following equation;

$$\frac{d\sigma}{d\varepsilon} = \alpha.(\sigma + \beta) \tag{2.1}$$

Where ε & σ are strain and stress respectively. A solution for this is first order ODE is;

$$\sigma = \mu e^{\alpha\varepsilon} - \beta \tag{2.2}$$

Where μ is a free parameter determined empirically. The stress-strain of a passive muscle can be likened to tension being applied yarn. As more strands of the yarn are pulled into tension the stress increases, then as the last strands are brought into tension a maximum stress is reached, until the yield stress is reached. Linear approximations can still be made over regions of elongation depending on accuracy required for application. The stress-strain of an active muscle (i.e. when it is tetanised) is approximated to a piece-wise quadratic function or bell curve. It is important to note that the stress for both active and passive muscle is zero when the strain is less than 0.4, demonstrating the yarn-like nature of the muscle stress-strain.

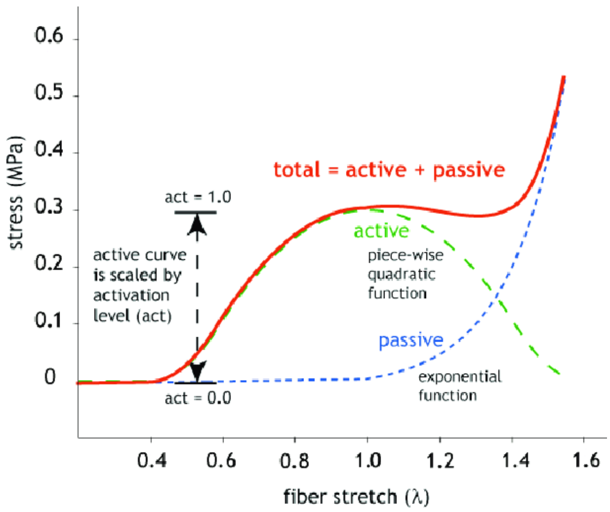

Figure 2.6: Plot showing the stress and strain of active and passive muscles [12]

Hill's muscle models commonly refer to a mechanical three element model [62] composed from, one parallel non-linear spring element, one series non-linear spring element, and a contractile unit, displayed as a free-body diagram in Figure 2.7 with the corresponding Equation 2.3.

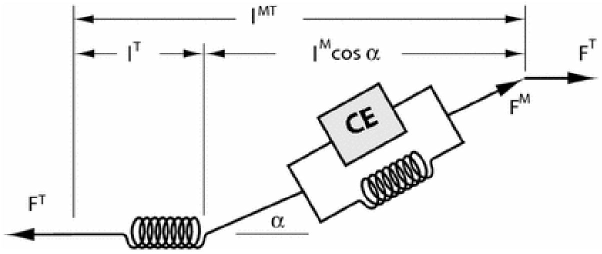

FIGURE 2.7: Hill muscle model[13]

Where F^{KT} and F^{KM} are the spring forces of the tendon and muscle respectively, which are a function of extension length. $F^C E$ is the contractile force and F^T is the total contractile force as observed at the end of each tendon either end of the muscle. Where F^T is the tendon force; F^M is the muscle force; the l^T, l^M, l^{MT} are muscle length, tendon length and their combined lengths respectively; α is the pennation angle (i.e. zero if parallel muscle); The left and right non-linear spring elements represent a tendon and muscle spring characteristic respectively; The CE box represents the contractile element that generates contractile force.

$$F^T = F^{KT} + (F^{CE} + F^{KM})cos(\alpha) \tag{2.3}$$

2.2.3 Electrical Muscle Models

Similar to EAP-based artificial skin and artificial muscles, biological muscles also require electrical stimulation to function. The main method for providing an artificial electrical stimulation to a muscle, to simulate the signal a motor neuron would give to a muscle, is functional electrical stimulation (FES). Due to the biochemical nature of the motor neuron signal transport and the purely electrical stimulation provided by the FES device, the process isn't as efficient as the naturally occurring electro-chemical muscle activation, often resulting in increased muscle fatigue when compared to equivalent voluntary muscle contractions [63]. FES applies a voltage across between two electrodes on the user's skin above a specific muscle. The voltage simulates the signal form and frequency of action potentials between 4 - 12Hz[64]. The threshold for a muscle action potential to cause a muscle contraction is approximately 70 mV [65]. EMG also commonly uses two

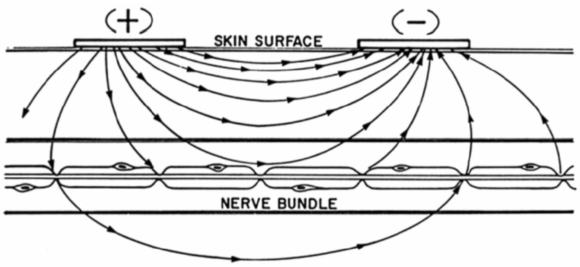

FIGURE 2.8: Electric field generated by two electrodes on the surface of the skin above a specific muscle and hence it's activating nerve bundle[14]

electrodes on the surface of the skin above a desired muscle. EMG senses the nerve impulses sent to the muscle and propagated through action potential.

2.2.4 Artificial Muscle Technology

There are many types of electrically actuated artificial muscles technology. Artificial muscle actuator technology that has gained particular interest in recent years include, the ionic polymer-metal composite (IPMC) actuator, the hydraulically amplified self-healing electrostatic (HASEL) actuator, magnetorheolgical elastomer (MRE) actuators, and dielectric elastomer actuators (DEAs). Each of these having qualities very similar to that of biological muscle usually with a trade-off in actuation response time, actuation force, and actuation strain for their various possible topologies. This section gives a brief overview of four state-of-art soft electromagnetically driven actuator technologies.

2.2.4.1 Ionic polymer–metal composite actuator

Ionic polymer-metal composite actuators (IPMCs) are soft actuators that can be actuated at a much lower excitation voltage than DEAs, commonly being less 10V. IPMCs are also desirable as artificial muscles as they can display large bending deformations, simple to fabricate, light weight and thin in design, and can have a fast actuation response time (¿15Hz) at small displacements[66]. IPMCs also have a high work density and maintain a constant volume during actuation like biological muscles. An IPMC is

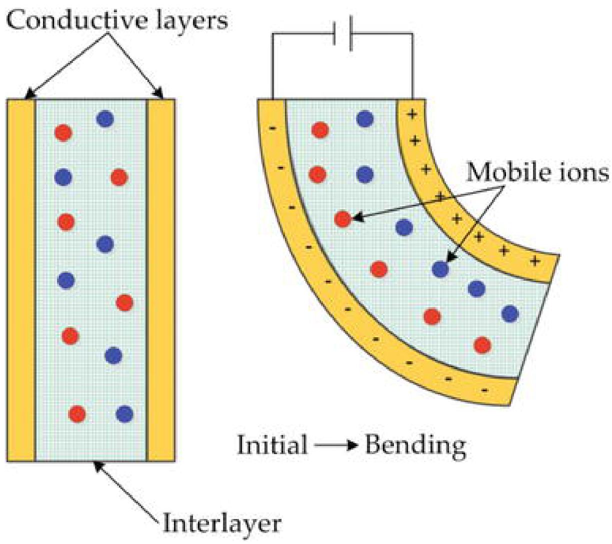

FIGURE 2.9: Diagram of the typical architecture of an IPMC actuator[15]

made up of an ionic polymer interlayer, two electrode conductive layers, and a voltage source. The ionic polymer interlayer allows for ionic transport and is typically made of treated Nafion or Flemion. These materials are typically used as ion exchange membranes so have the characteristics desired for the transporting ions during the actuation of the IPMC actuator. The two electrodes are made of a suitably conductive and flexible material. The interlayer is treated such that it is filled with water molecules and cations, with the chemical backbone of the interlayer being slightly negatively charged. When a voltage is applied across the electrodes the cations are repelled from the cathode and travel towards the anode while the water molecules are displaced in the opposite direction towards the cathode. The ionic polymer then swells as the cations repel each other along the anode side of the interlayer, while the polymer elements on the cathode side effectively shrink[67]. This swelling adjacent to the cathode provides the device's bending actuation.

There are many variations of the design and manufacturing of IPMCs to optimise the actuator for an application as shown by [68].Although the process of manufacturing IPMCs is simple, it takes a long amount of time (often can be over 48hours[66]) for the ionic polymer interlayer to absorb the necessary ions and undergo the necessary reactions. There has been much research into the optimal manufacturing of an IPMC [68–70]. The use of additive manufacturing has been used successfully to generate more complex geometries using fused filament deposition[71].

IPMCs can also be used as sensors. When an IPMC undergoes bending due to an external force there is a potential generated across the electrodes, which indicates bending direction and magnitude[72].

Two key deficiencies of current IPMC actuator technology are the maximum force output achievable and the life cycle of the actuator in a dry (non-aqueous) environment.The force output optimisation of IPMCs has been investigated by several researchers, all of which having a maximum actuation force in the milli-newton scale [72–74]. Because the IPMC actuators rely on hydrated ionic transport to actuate this means if the IPMCs are in a dry environment then over time they will decrease their maximum actuation force.

The applications of this actuator is limited to applications requiring a small actuation force and a wet environment. Current applications include flexible catheters [75], small biomimetic robotics [76, 77], aquatic robotics[78, 79], with many other applications yet to be discovered.

2.2.4.2 HASEL actuator

A hydraulically amplified self-healing electrostatic (HASEL) actuator is a recent soft actuator technology developed in 2018[16] which displays many qualities that are better than current artificial muscle technology. HASEL actuators are made up of three main components: electrodes, dielectric fluid, and an elastomeric shell. The electrodes need to be highly conductive, able to handle high electric potential, and can be solid or flexible. Hydrogel electrodes have been proven to be a good material for the electrodes because of their elasticity while still maintaining a high conductivity[80]. In one application the hydrogel material is bonded to a polydimethylsiloxane (PDMS) substrate for mechanical strength and for ease of bonding to the actuator biaxially-oriented polypropylene (BOPP) shell[16, 81]. HASEL actuators use high electric potential across two electrodes to create an electrostatic force. This force induces a 'zipping' effect which pulls the electrode together from one end to the other as the electric field strength increases. The zipping of the two electrodes pushes the dielectric fluid into the reservoir increasing the pressure which alters the shape of the reservoir bounds providing an actuation motion. When the electrodes have displaced all of the fluid between them the actuation displacement is at a maximum. The electrostatic zipping action allows a large force to be generated due to snap-through transition. Snap-through transition is an actuation instability which has been discussed in previous research as a means of amplifying DEA actuation strain[82]. Recorded efficiency values of HASEL actuators of 21% are comparable to that of human muscles of 20 - 35% [61]. The actuators have had a frequency response of up to 20Hz. Large strains of 124% have been recorded, but can only

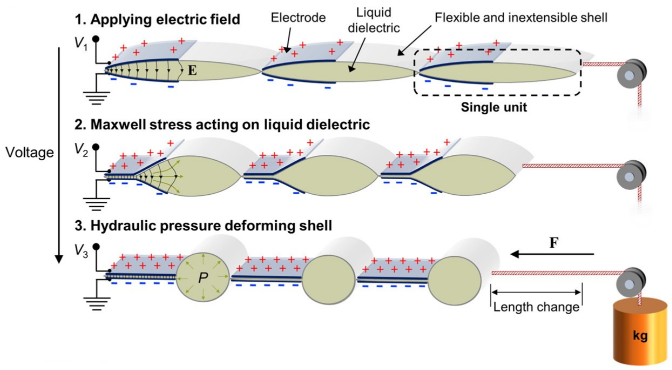

FIGURE 2.10: Diagram of the typical architecture and the contraction stages of a HASEL actuator[16]

be achieved when actuating at a resonant frequency. Strains of up to 79% have been recorded using a linear planar HASEL actuator configuration and DC voltage stepping. Else, strains of only 10% have been recorded for static steady strain[16]. Because there is a relationship between the motion of the actuation and capacitance between the electrodes, this means self sensing can be achieved through the electrodes. Although due to the flexible and fluid nature of the device, modelling of the HASEL is difficult and limited in accuracy.

The simple and commonly used manufacturing process for HASEL actuators is completed in six steps as shown by the diagram below:

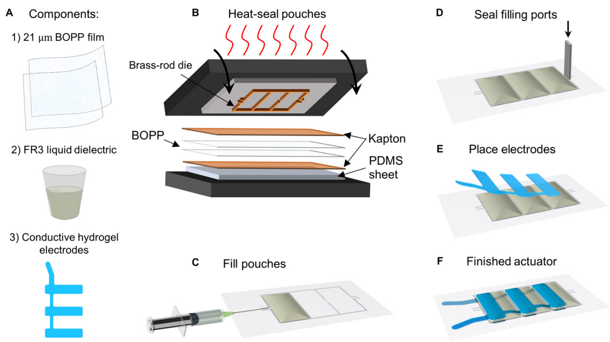

FIGURE 2.11: Diagram of the simplified stages of HASEL actuator production[16]

Other attempts have been made to use polyjet inkjet based additive manufacturing to make the whole HASEL actuator and have been successful with proof of concept, but are yet to be developed from prototype stage[83].

The cyclic life of HASEL actuators are high, because of their 'self-healing' properties. When there is a dielectric breakdown through the liquid dielectric the damage caused is not permanent like when a DE breaks down. The liquid may form some small air bubbles, however these may not effect the operation of the actuator, instead this can increase the likelihood of a another dielectric breakdown. The cycle life of the HASEL actuator was seen to be larger than one million with a given torus shaped HASEL actuator[80].

The number topologies possible with HASEL actuators is limitless. Some topologies of HASEL actuators include torus, planar linear[80], scorpion metasoma[84].

2.2.4.3 Magnetorheological Elastomer

Magnetorheological elastomer (MRE) actuators are a relatively new form of actuator however the theory reinforcing operating principle has been known since at least the 1980s [85]. The structure of an MRE actuator generally consists of a ferromagnetic elastic composite and a driving magnetic field. An example of this is a composite of iron-carbonyl powder and PDMS. The The operating principle of these are that magnetic flux travelling through the the MRE will change mechanical characteristics within the elastomer (i.e. stiffness or displacement of the body). The operation of a MRE actuator is similar to a DEA however instead of having an electric field cause a contraction it is a magnetic field causing a deformation. An MRE is typically made of silicone rubber containing magnetic ferrite based particles uniformly distributing throughout its volume. This kind of actuator is current controlled and can hence operate at a low voltage. This helps mitigate the risk of electric shock of a device in close proximity to humans (unlike HASEL actuators and DEAs).

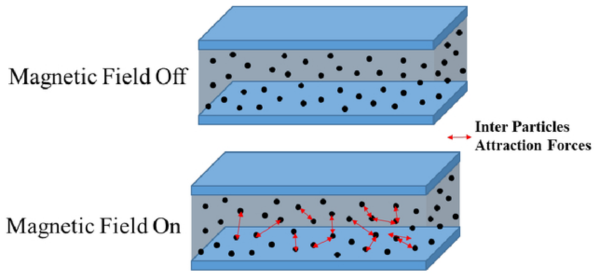

FIGURE 2.12: Diagram showing MRE contraction actuation when a magnetic field is applied[17]

A key issue with using magnetorheological elastomers as soft actuators is that they require heavy gauge conductors for the high current they require for generating a magnetic field. The high current requirement means that actuators have only been created that have a solid electromagnet driving a soft MRE[86].

When manufacturing MREs, uncured liquid silicone rubber is mixed with magnetic (commonly carbonyl iron) particles to form a 3 dimensional matrix of crosslinks with the magnetic particles fixed between the crosslinked polymers. A key issue when creating an MRE is the conglomeration of magnetic particles due to residual water within the mixing operation. The magnetic particles can be processed to have a hydrophobic quality to mitigate this issue. During the curing process a magnetic field can be applied to align the particles within the elastomer as it becomes more rigid.

There have been attempts to use additive manufacturing to make MREs[87], however the method described has not optimsied the structure of MRE for any application and the dipersion of MRE is not uniform throughout the print volume.

The current applications of MRE actuators are limited, however magnetorheological fluid (MRF), is a fluid which becomes more viscous with an applied magnetic field as currently has many modern applications. This fluid substance is largely used in applications where damping control is desired such as vehicle suspension[88], medical assitive devices[89] and helicopter seat damping [90]. Potential MRE actuator applications include fluid valve control[86] and active vibration control similar to that mentioned for MRFs[88].

2.2.4.4 Dielectric Elastomer Actuators

The dielectric elastomer actuator (DEAs) are often called artificial muscles because they share similar characteristics to biological muscle such as, the large strains achievable, the high elastic energy density, many topologies/configurations achievable, and constant volume during its contraction.

A DEA consists of a dielectric elastomer (DE) film sandwiched between two compliant electrodes. To excite the actuation, a high electric potential is applied to across the electrodes creating an electrostatic force between the two compliant electrodes. This force pulls the two electrodes together applying stress (known as Maxwell's stress) to the elastomer and hence strain parallel and perpendicular to direction of the electrostatic force. When the DEA is contracted the surface area of the electrodes increases and the thickness of the DE decreases causing a change in capacitance and Maxwell's stress. A

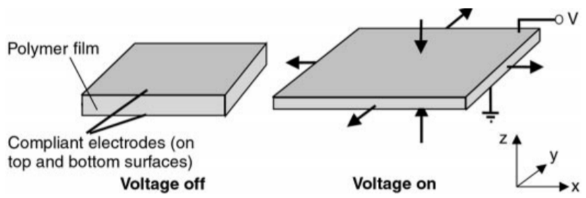

FIGURE 2.13: Diagram of a DEA with a with no voltage and a voltage applied across the electrodes. [18]

dielectric elastomer actuator can be modelled as a flexible parallel plate capacitor in its simplest form. Using this we can determine the electrostatic pressure to be:

$$\sigma_{es} = \varepsilon_0 \varepsilon_r \frac{V^2}{z^2} \tag{2.4}$$

Where p_{ES} is the electrostatic pressure, ε_0 and ε_r are the vacuum and relative permittivity constants, V is the voltage potential applied across the electrodes and z is the thickness of the DE. The electrodes used for a DEA need to be made of a conductive material, but require similar elasticity to the dielectric material. An ideal material for these electrodes would have high conductivity. This conductivity would change minimally and predicatively under large strains. Many composites have been used in practice for these electrodes, with the most common in early development being a silicone rubber and carbon powder composite. However, the unpredictable nature of carbon powder elastomer composites has lead to research into many other materials/silicone additives such as hydrogels, graphene sheets, metallic nanostructures, carbon nanotubes, liquid metal[91–94]. The ideal material for the dielectric elastomer should have a high elastic modulus and a high electric breakdown voltage. The elastic modulus needs to be sufficiently high so that less electrostatic pressure can create a larger strain. While the breakdown voltage of the material needs to be sufficiently high such that the material will not break down at the maximum desired strain. If a material can be found with a high enough electric breakdown strength at a smaller thickness than current research prototypes then a higher stress can be achieved giving a larger or equivalent actuation force at a lower voltage.

Many other topologies exist to generate different actuation motions using the same electrostatic pressure generation principle. These include actuator topologies such as stack[95, 96], helical[97], bending[98], lens[99], cylindrical, and rolled shaped actuators[100]. Each of which having a range of applications.

DEAs are often fabricated in a laboratory environment using a pre-strained elastomer. The pre-straining does three key things; stores elastic strain energy, ensures DE is planar within the bounds of the jig, and controls the initial thickness of the elastomer. There is no standard practice for the fabrication of DEAs, other methods such as additive manufacturing have also been explored to generate more complex geometries and to increase production speed[101, 102].

As well as actuating, DEAs can also be used for sensing. DEAs can be used as sensitive capactive sensors, where any strain applied to the DE will relate to the effective capacitance between the two electrodes[35, 103, 104].

Currently dielectric elastomer actuators all require voltages within the kilo-volt range to generate what can be called a useful stress and strain for many applications. A key problem encountered by researchers designing DEAs is the trade-off between actuation force and strain magnitude [95]. This high voltage requirement makes the technology dangerous for use where there is a possibility that a human may come into physical contact with the high voltage electrodes.

2.3 Pressure Mapping Artificial Skin Devices

This section will be outlining some of the main technologies which are flexible and/or soft and can map force events throughout a two dimensional surface. A particular focus on electro-active polymer (EAP) based sensing is present due to the potential of miniaturising the technology and the range of miniaturised electronics currently available. Electroactive polymers are essentially polymer materials which can be used as transducers which change electrical properties based on a mechanical input, vice versa.

2.3.1 Soft Pressure mapping technology

Pressure mapping devices can be categorised into their various sensing technology, such as resistive, capacitive, inductive, magnetic, optical, and acoustic. Examples have been gathered by [] showing the limits and trade-offs between each sensing technology.

2.3.1.1 Resistive

Soft resistive pressure mapping has been commonly achieved in the past by using arrays of piezoresistive sensor elements []. The resistive elements can be made using several different flexible piezoresistive materials.

- Conductive particle polymer composites [105–107]
- Intrinsically conductive polymers [106, 108]

- Microfluidic metals [109–111]
- Hydrogel structures [81, 112, 113]
- Flexible piezoresistive semiconductors [114, 115]

	Conductivity	Piezo-resistivity	Change stiffness	Fabrication	Cost	Environmental Stability	Toxicity
Intrinsically conducting polymers	- Dependent on polymer used. (S/cm [108])	- Dependent on polymer used - Exponential relationship with strain[?]					
Electrolytic hydrogels							
Conductive particle polymers					$		
Conductive particle paste					$		
Conductive textiles				Complex			

A commonly used piezoresistive material is conductive particle polymer composites.

2.3.1.2 Capacitive

Similar to resistive pressure mapping, capacitive pressure mapping has more commonly been done using arrays of capacitive elements. Many capacitive touch sensors use the human body to shunt the electric field between the capacitor electrode(s) to a common ground. However the operating principle of capacitive-based strain sensors rely on the deformation of the capacitor dielectric and/or the capacitor electrodes.

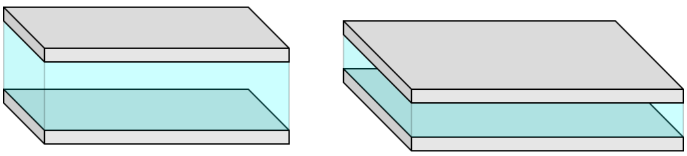

FIGURE 2.14: Two grey electrodes across a blue dielectric medium. Left: Uncompressed state. Right: Compressed state exhibiting larger electrode areas and a thinner dielectric thickness.

2.3.1.3 Magnetic

Magnetic strain mapping devices can be achieved using several methods. One method is to have a three layer stack with hall effect sensors [116]. The stack is made up of a the bottom layer full of rigidly connected three dimensional hall effect sensors, the second layer is made from an elastomer, and the top layer has a magnetic particle unit placed at a set distance above each of the hall effect sensors. The movement of the magnets alters the magnitude and direction of magnetic field sensed and data can be interpolated to create a map of strain deformation. The main advantages of this method is that each hall sensor can detect in three dimensions, hence normal and shear forces can be detected, and using magnetismfor sensing means less electrical noise in the system. The main disadvantages of this method of sensing is the added complexity in scaling the system and the electronics required and the rigid surface required.

2.3.1.4 Optical

There are various methods for making a optically driven artificial skins. A recent review has been curated by Lee et al. [117] all of the different methods of using optics for creating tactile sensors. The main advantages of optical sensors include the high speed sensor response, immunity to electrical noise, and their non-invasive nature. The main disadvantages include, the bulky hardware required for driving the optics and signal processing, the potential interference of external light sources, and the materials that can carry optical signals.

2.3.1.5 Acoustic

Acoustic soft tactile sensing has not been explored much compared to the other forms of sensing given. Park et al., Hughes and Correll [112, 118] have created a system which uses passive acoustic tomogrpahy (PAT) to localise and and classify different types of touch. This form of tactile sensing is the most similar to the biological system of mechanoreceptors which are specialised to detect certain frequencies of vibration.

2.3.1.6 Pressure mapping technology comparison

2.4 Soft Conductive Particle Piezoresistive Composites

Soft sensors and actuators require low-stiffness materials for their active sensing/actuation domains. The requirement of softness is governed by the mechanical modulus values depend on the application requirements. The use of conductive particle elastomer composites is explored in this work due to the customisability of the electromechanical characteristics.

A core part of this work is understanding the behaviour of conductive particle elastomer composites beause of their use as EAPs which can be used for a range of sensing and actuating purposes. The characteristics that make conductive particle elastomer composites (CPECs) ideal for soft sensor and actuator devices often include:

- Low stiffness
- Changeable conductivity
- Piezoresistivity
- Mouldable
- 3D printable
- Low toxicity
- Durable
- Inexpensive
- Easy to obtain
- Simple fabrication process
- Sustainable

2.4.1 Fabricating Conductive Particle Elastomer Composites

Before exploring the known conduction and piezoresistive mechanisms and models for CPECs, it is important to understand how the fabrication process of a CPEC may affect its physical structure.

CPECs are made by dispersing conductive particles through a curable liquid elastomer matrix. To change the electromechanical properties of the material, the dispersion of the conductive particles throughout the matrix can be optimised through various methods. To minimise the agglomerations of primary conductive particles often a sonication step is completed. This involves a mixture of the conductive particles and a liquid, usually in the form of a solvent, to be placed in a sonication bath. The sonication bath performs a frequency sweep whereby the resonant modes of the agglomerates are met causing separation of the agglomerates into their primary particles []. The degree of dispersion is governed by the time in the sonication bath, the sonication frequencies, and sonication amplitudes []. This sonication usually occurs before the the particles are added to the elastomeric matrix due to the large viscous damping effects of liquid elastomers. The next step involves mixing the dispersed conductive particles throughout the liquid elastomer, this can be done using a variety of mixing methods, including a planetary mixer, magnetic mixer, screw mixer, static mixers, amongst others []. During the mixing process often the liquid solvent used in the dispersion stage is evaporated, leaving only the curable elastomer and the conductive particles. When sufficient mixing of the liquid elastomer and conductive particles have been completed the material is formed into a desired final shape using advanced additive manufacturing methods [] or traditional moulding [] or film making techniques []. During the moulding process the material undergoes a form of curing, such as UV curing, catalysed curing, or moisture curing[]. If the composite material has not already been integrated into a device containing electrodes and other mechanical support structures these are integrated at the end of the process [].

2.4.2 Modelling Conduction mechanism

The typical fabrication process stated in Section 2.4.1 for CPECs shows that the dispersion of conductive particles will always vary.

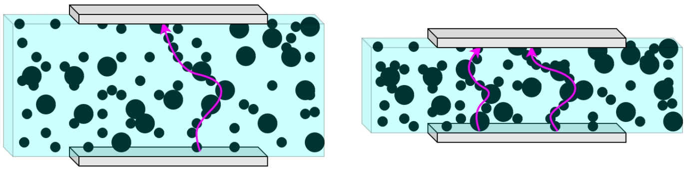

FIGURE 2.15: Two grey electrodes across a CPEC cuboid showing enlarged black conductive particles within a blue polymer matrix. Left: An uncompressed CPEC. Right: A compressed CPEC.

Some of the physical features of these conductive percolation networks can be quantified and directly relate to the macro-level electromechanical properties of the material. Such characteristics of a conductive percolation network include:

1. Conductive particle(s) used
    (a) Aspect ratio [119, 120]
    (b) Inherent particle conductivity
2. Conductive particle dispersion [121]
    (a) Inter-particle distance distribution
    (b) Particle agglomeration distribution [122]
    (c) Isotropy/anisotropy [123]
    (d) Sedimentation [124]
3. Elastomeric matrix
    (a) Viscosity
    (b) Elastic modulus
    (c) Dielectric permittivity
4. Impurities
5. Voids

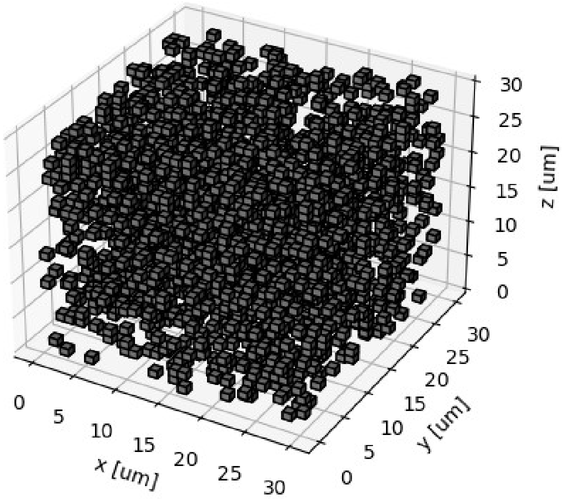

FIGURE 2.16: Example of a randomised cube percolation with a volume percentage of 8% of particles

Microscale models for CPECs and the relationship between particle and electric charge motion are often computationally heavy, overly idealised, and non-invertible [125]. A microscale model example can be seen in Figure 2.16. However, microscale modelling of CPECs may give insight into understanding complex physical phenomena that may relate to the macroscale models made for CPECs. An alternate method for modelling CPECs is the formation of macroscale models[126].

Electrical DC conduction through a CPEC occurs using two main mechanisms, Coulomb conduction and quantum tunneling [127–130]. Coulomb conduction uses the conduction band electrons are shared by adjacent atoms allow conduction throughout chains of cascading conductive particles. The second mechanism of conduction is through quantum tunneling which is stochastic in nature and allows for conduction through insulative boundaries between the percolative network of conductive particles [131, 132].

Electrical AC conduction can occur through a CPEC through capacitive means depending of particle spacing[**?**].

2.5 It Has Been Done Before

Chapter 3

A Simple Conductive Elastomer Composite Material with Complex Behaviour

3.1 Introduction

As discussed in Section **??** conductive particle elastomer composites are desirable for soft sensor and actuator applications for a variety of reasons. However, it is crucial to understand the electromechanical behaviour of these composites if we wish to create complex control systems with such materials. Although conductive particle elastomer composites are a simple concept of dispersing particles throughout an elastomeric matrix, the electromechanical behaviour is not well understood on a macro or micro-scale. This section endeavours to understand the material behaviours of carbon black silicone rubber composites on a macro-scale to help create better inverse models so that the material can be used more accurately as a stress and/or strain sensor.

3.2 Material Imaging

3.3 Stress and Resistance Relaxation For Carbon Nanoparticle Silicone Rubber Composite Large-Strain Sensors

From a conference paper presented at IDETC-MESA 2021

Carbon nanoparticle-silicone elastomer composites are stretchable conductive materials with diverse applications such as, highly elastic strain sensors [107, 133, 134], dielectric elastomer actuators [135, 136] and electromyography electrodes[134, 137, 138]. Understanding the dynamic resistance relaxation characteristics of carbon black (CB) polydimethylsiloxane (PDMS) elastomer composites would improve performance in fields which require high efficiency of space, power and accuracy, such as the devices used in biomedical and aerospace fields. Unlike many common strain gauges, CB-PDMS composites can have strains of over 300% without yielding[139] depending on the type of PDMS and CB used and the method of fabrication.

Some characteristics of CB-PDMS composites which make it suitable for strain sensors include that, the material is relatively inexpensive and readily available; non-toxic and is bio-compatible; and has a significant and readily measurable resistance change when stretched. Whereas, alternatives to CB nanoparticles, such as carbon nanotubes[140, 141] and metallic particles[94, 142], have been seen to be more carcinogenic than the CB alternative[143–145]. The fabrication of the CB-PDMS composite requires a degree of optimisation to ensure that the carbon particles are adequately dispersed to ensure high conductivity and high yield strength of the material. More importantly the homogeneous dispersion of carbon black particles means better repeatability of experimental results and more accurate models for the eventual applications of CB-PDMS composites. A sufficiently comprehensive model of how the resistivity changes with strain has not yet been developed. A limitation of using this material as a strain sensor is the non-linearity of the material above a certain strain value, at which the composite's resistivity diverges towards a highly insulative value within the giga-ohms range. This non-linear behaviour of CB-PDMS can be used as a mechanically activated switching device[135]. If modelled, this non-linearity could extend the range of strains that can be measured.

While previous work from our research group [146, 147] has focused on the response to quasi-static and low speed behaviour, these materials show dynamic effects where resistance depends on the speed of stretching. The characterisation investigated for the CB-PDMS sensor involves understanding the relationship between the mechanical stress relaxation, electrical resistance relaxation and strain in time. A difference in time constants between the stress and resistance relaxations have been noted before in literature[140, 141, 148, 149], but never accurately modelled with the physical theory explained. The current limitations of predictability and repeatability of resistance relaxation hinders the accuracy of fitting models. An understanding of this resistance relaxation phenomena would mean an accurate model could be made to predict the relationship between stress, strain and resistance within a CB-PDMS composite. Finding this relationship model would also allow us to understand the limitations of using this composite in sensing applications and also the use of the material in dielectric elastomer actuators, whereby the material can be used simultaneously as an actuation excitation electrode and a strain sensor. The composite material can also be used in human motion measurement as a skin stretch sensor. Understanding these characteristics may give rise to new applications of the composites material, for example, if the resistive relaxation properties of the material were known, it could be used as a mechanically activated timing device. An oscillatory flexible dynamic circuit has been demonstrated when mimicking the motion of a caterpillar as shown by Henke et al.[135], where the resistance relaxation modelling is be useful for more accurate electrical circuit dynamics. The theory behind mechanical stress relaxation is widely known and has been modelled using a variety of mathematical models [19] depending on the material modelled. The research discussed will focus primarily on only tensile stress of the specimen, and how it relates to the electrical resistive relaxation.

BACKGROUND

The Composite

The CB-PDMS composite was composed of carbon black powder(Vulcan XC 72R, average particle size: 50 nm, typical bulk density: 96 kg/m^3) and two part Pt cured

PDMS(Smooth-On Dragon Skin 10 NV). This grade of PDMS was chosen due to the following characteristics [150]:

1. Low elastic modulus, E, of 186 kPa
2. Tensile strength, σ_y of 2.75 MPa
3. Low mixed viscosity, η, of 6,000 cps

The volume resistivity of pure carbon black powder itself is between 10^{-1} and 10^{2} Ωcm depending on how densely the particles are packed and the purity of the CB[107]. The ability of a carbon black matrix embedded within a highly insulative PDMS substrate to become conductive is determined mainly by the dispersion of the CB particles, and the tunneling that occurs between conductive CB and insulative PDMS bodies within the material volume[107, 141]. The composite being created must be highly conductive without compromising the elastic modulus and yield strength of the material. From percolation theory observed in literature [107] there is a threshold volume percentage of CB required to ensure that conductivity is maintained with certainty throughout the composite volume within the linear volume resistivity region. The percolation threshold for our composite was is difficult to predict analytically due to the unknown configurations of aggregates and agglomerations formed by the CB within the composite material. Experimentally we found that a CB volume percentage of 7.5% or greater meant the composite material had a resistivity of less than 3.5 kΩcm consistently with the fabrication method used.

The Mechanics

It is known that PDMS composites are viscoelastic materials and clearly exhibit the three traits of a viscolelastic material[19]: stress relaxation, strain creep and stress-strain hysteresis. Stress relaxation is effect observed when a step input of strain is applied to a material and there is a transient stress decay response which converges to a steady state value. A commonly used model for viscoelasticty is the generalized Maxwell body model of order n shown in Fig. 3.1.

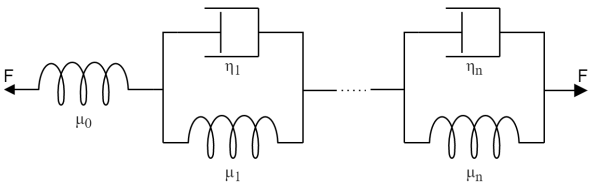

FIGURE 3.1: MECHANICAL SPRING DASHPOT DIAGRAM OF THE GENERALIZED MAXWELL BODY MODEL ADAPTED FROM FUNG ET AL.[19]

In Fig 3.1 F is the force applied to the material and μ and η values represent the spring and damping component constants, respectively. The stress relaxation function for this model is found in Eqn. 3.1, for, n, serial repeating units.

$$G(t) = a_0 + \sum_{i=1}^{n} a_i e^{-t/\tau_i} \tag{3.1}$$

Where a_0, a_i are the magnitudes of relaxation and τ_i are the relaxation decay time constant components. All of the constants a_0, a_i, and τ_i are functions of η and μ.

We initially assume that there is a relationship between the stress relaxation and resistance relaxation of the material. However the generalized model can easily over-fit the data, if n is too high, due to it's generality.

MATERIALS AND METHODS

Composite Fabrication

The first step in fabrication was to mix the CB nano-powder with the silicone part A (the liquid PDMS elastomer) using a Kurabo KK-50S planetary mixer. A mixing function was used with specific rotational velocities and times for each axis, which was well suited towards de-aeration and viscous particle mixing. The material was then mixed with the silicone part B (the liquid PDMS elastomer cross-linker) using the same planetary mixing function to ensure adequate dispersion of the CB particles throughout the PDMS volume as well as de-aeration.

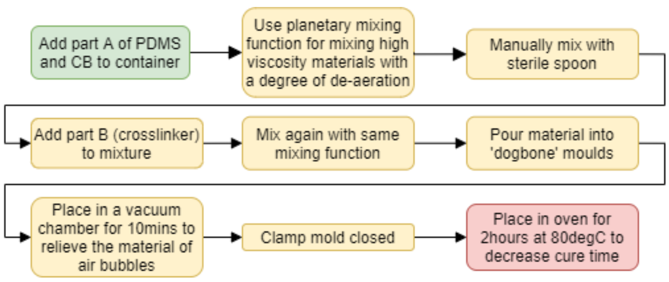

FIGURE 3.2: THE STEPS INVOLVED IN CREATING THE CB-PDMS COMPOSITE MATERIAL

For the fabrication of the CB-PDMS specimens, a standard dog-bone shaped mould was developed for the mixed CB-PDMS to cure in, based on ASTM standard D412[151]. Before the mould was clamped shut the composite filled mould was immediately placed in a vacuum chamber for ten minutes to de-aerate the still liquid, curing CD-PDMS mixture. The specimen was placed in a controlled oven at a temperature of 80 °C for a two hours to maintain the repeatability of the curing stage of the fabrication process. The temperature at which the silicone contributes towards the elastic modulus and yield strength of the material, with increasing curing temperatures giving increasing elastic moduli and decreasing yield strength values.

Measurement

A custom test measurement device was made for measuring the desired characteristics of the CB-PDMS material, so that parameters driving the data collection could be easily altered. The strain, stress and resistivity of the specimen were measured in in parallel. The setup included the use of a 500 gram loadcell (HT sensor - TAL221) in combination with a linear actuator stage driven by a NEMA23 stepper motor and an source measurement unit (Keithley 2634B SMU). A custom electrode clamp mechanism was designed to fix the electrodes onto the test specimen during the straining of the specimen. This consists of two copper plates sandwiching the composite material at each end of the dogbone test specimen.

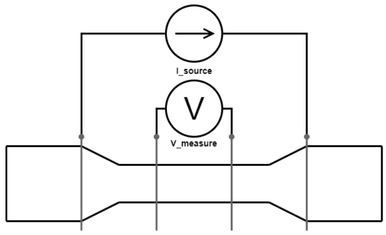

FIGURE 3.3: THE COMPOSITE DOGBONE TEST SPECIMEN PIERCED BY 4 PIN ELECTRODES. THE OUTER AND INNER ELECTRODES CONNECTED TO AN SMU CURRENT SOURCE AND VOLTMETER RESPECTIVELY

Two configurations of resistance measurement were tested, a two wire and a four wire method. The two wire measurement method used two electrodes which also clamped the test specimen at each end. It was observed that compressive strain applied to CB-PDMS composite will increase the resistivity of the specimen in a similar fashion to tensile stress. Only a compressive strain was applied to the material by the clamps such that the material would not slip during tensile testing and not deform giving erroneous resistance results. The Poisson's ratio of the material which was found experimentally to be 0.29 for both CB percentages. The two wire method used a controlled current source in parallel with a voltmeter attached to the same two electrodes to derive a resistance. The four wire method uses four pin electrodes as seen in Fig. 3.3. The four wire method applies a constant current source through the outer electrodes and uses a voltmeter on the inner two electrode to determine the resistance and hence resistivity of the material. The four wire electrode configuration meant that the resistivity had a smaller signal to noise ration compared to a two wire alternative.

Metallic pin electrodes were selected over copper clamp and conductive adhesive alternatives as they deformed the material the least, had a consistently low specimen-electrode contact resistance, and did not slip during test sequences. The inner pin electrodes were symmetric about the centre and placed 20 mm apart with the outer pin electrodes being 40mm apart as shown in Fig. 3.4.

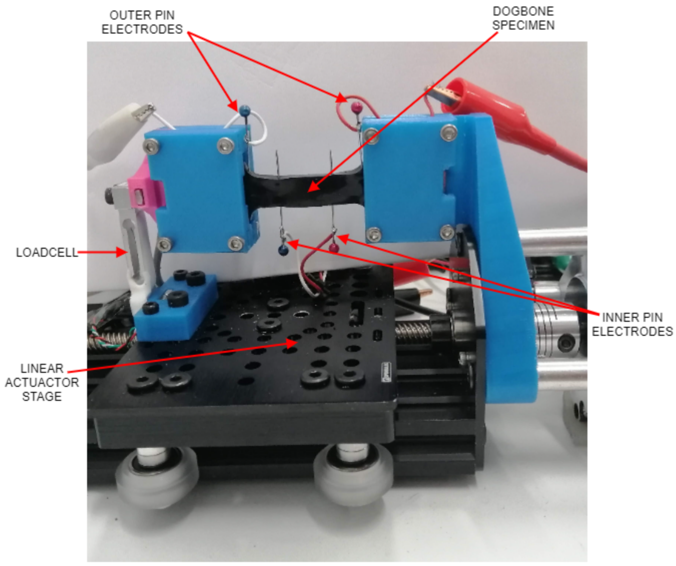

FIGURE 3.4: PHOTO OF TEST MEASUREMENT SETUP

The measurements were completed using finite pulse trains of strain to ensure repeatability of the models were consistent across varying experimental parameters. If this material is used as a sensor the model fitted to the stress relaxation must hold over many consecutive tensile strain events. As these materials are intended as large strain sensors, the strains tested in this work was 10%, 20%, and 30%. This strain percentage is higher than commonly used constantan strain gauges, which typically have a maximum strain of approximately ±3%[152], with traditional metal alloy based strain gauges often having significant plastic deformation after less than 10^4 cycles[152] at 3% strain.

RESULTS AND DISCUSSION

Viscoelasticity

All of the specimens fabricated indicated a degree of viscoelasticity shown by the hysteresis seen when loading and unloading the material with 30% tensile strain in Fig. 3.5. The 0, 7.5, and 10 w.t.% CB specimens have average elastic moduli, as measured in the loading phase, of 205.2 kPa[1], 321.4 kPa, and 342.1 kPa, respectively. The hysteresis loop seen in the 10 w.t.% CB sample has a larger hysteresis loop showing that there is increased viscous/damping compared with the other two specimens percentages of CB. The pure PDMS specimen had no discernible hysteresis from the data as shown in Fig. 3.5. The difference in hysteresis and hence viscolelastic properties, across the specimens will lead to different stress relaxation properties across the three composite materials.

[1]Different from the 186.2 kPa elastic modulus specified by the manufacturer due to the temperature accelerated curing method used

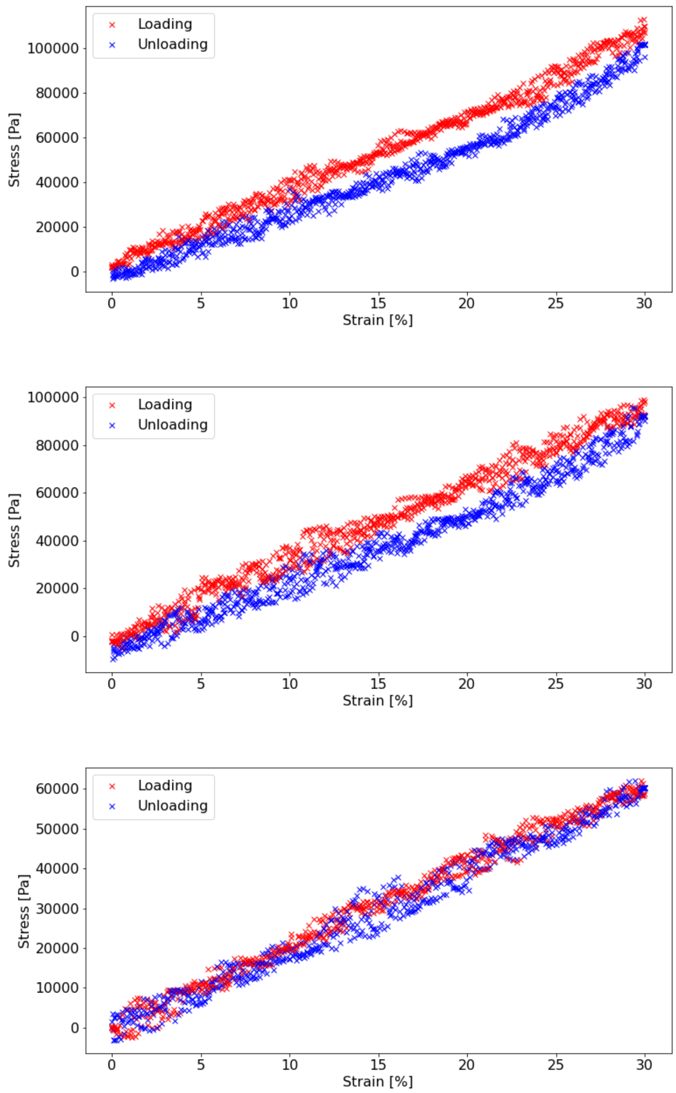

FIGURE 3.5: THE LOADING AND UNLOADING OF 30% STRAIN ON A COMPOSITE TEST SPECIMENS WITH CB WEIGHT PERCENTAGES FROM TOP TO BOTTOM OF 10%, 7.5%, AND 0% WITH DATA COLLECTED OVER FIVE LOADING AND UNLOADING CYCLES

Resistance Relaxation Model Fitting

The initial model chosen to fit the stress and resistance relaxation data was the generalized Maxwell body model shown in Fig. 3.1 with n = 3 cascading elements using Eqn. 3.2 to fit the model. Fitting the data using Levenberg–Marquardt non-linear least square algorithm over 30 data sets showed an instability with the algorithm using this model. When feeding the previously fitted stress relaxation model constants as initial conditions for the fitting of the next stress relaxation data set, the values of the constants diverged exhibiting signs of overfitting. This divergence of the model constants meant that they had a large standard deviation showing the model was changing significantly each iteration of fitting. Hence a more simple model using Eqn. 3.1 with n = 2 was used to fit the stress relaxation data to Eqn. 3.3 with lower standard deviation of the model constants. Conversely when the resistance relaxation model analogous to stress relaxation model, shown in Eqn. 3.4, was fitted to the resistance relaxation data there was a stable fit with a better goodness of fit.

The decay time constants of the two models are different with the resistance having an longer overall decay which can clearly be seen in Fig. 3.6. Below in stress relaxation models $G_{1,2}(t)$, shown in Eqn. 3.2 and 3.3, the constants a_{0-3} and τ_{S1-S3} represent the components of magnitude and time decay of the stress relaxation, respectively.

$$G_1(t) = a_0 + a_1 e^{-t/\tau_{S1}} + a_2 e^{-t/\tau_{S2}} + a_3 e^{-t/\tau_{S3}} \tag{3.2}$$

$$G_2(t) = a_0 + a_1 e^{-t/\tau_{S1}} + a_2 e^{-t/\tau_{S2}} \tag{3.3}$$

Analogously for the resistance relaxation function $H(t)$, the constants b_{0-3} and τ_{R1-R3} represent the components of magnitude and time decay of the resistance relaxation, respectively.

$$H(t) = b_0 + b_1 e^{-t/\tau_{R1}} + b_2 e^{-t/\tau_{R2}} + b_3 e^{t/\tau_{R3}} \tag{3.4}$$

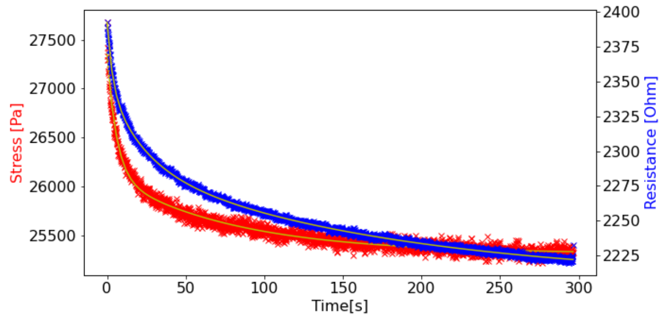

FIGURE 3.6: COMPARING THE RELAXATION DECAY TIME CONSTANTS OF STRESS AND RESISTANCE FOR A 7.5 W.T.% CB-PDMS COMPOSITE AFTER A 10% STRAIN STEP INPUT AND FITTING GENERALIZED MAXWELL BODY MODELS TO EACH.

The mean magnitude and decay time constants for the resistance and stress relaxations using 30 relaxation periods to fit the models to are given in table 3.3. The data gathered show that the stress relaxation time constant values decrease with an increasing carbon black percentage, indicating that all constants in Equations 3.4 and 3.3 are also functions of the carbon black percentage.

TABLE 3.1: FITTED CONSTANTS AND THEIR MEAN, μ, STANDARD DEVIATION, σ, AND COEFFICIENT OF VARIATION, CV, VALUES FOR 0%, 7.5%, AND 10% CB-PDMS COMPOSITE SPECIMENS USING EQUATION 3.3.

Stress Model

0 % CB Specimen			
Constant	μ	σ	CV
a_0	20344.71	42.61	0.20%
a_1	387.28	59.86	15.45%
a_2	526.82	57.65	10.94%
τ_{S1}	72.08	23.46	32.54%
τ_{S2}	5.77	1.48	25.75%
7.5 w.t.% CB Specimen			
Constant	μ	σ	CV
a_0	25363.89	33.62	0.13%
a_1	802.32	43.59	5.43%
a_2	1242.32	52.67	4.24%
τ_{S1}	71.01	9.49	13.37%
τ_{S2}	5.79	0.65	11.32%
10 w.t.% CB Specimen			
Constant	μ	σ	CV
a_0	32303.01	165.62	0.51%
a_1	1071.38	54.32	5.07%
a_2	1649.82	47.31	2.86%
τ_{S1}	84.07	10.55	12.54%
τ_{S2}	6.52	0.74	11.35%

TABLE 3.2: FITTED CONSTANTS AND THEIR MEAN, μ, STANDARD DEVIATION, σ, AND COEFFICIENT OF VARIATION, CV, VALUES FOR 0%, 7.5%, AND 10% CB-PDMS COMPOSITE SPECIMENS USING EQUATION 3.4.

Resistance Model

7.5 w.t.% CB Specimen			
Constant	μ	σ	CV
b_0	2154.31	52.68	2.44%
b_1	81.13	5.39	6.65%
b_2	56.37	3.67	6.52%
b_3	42.16	3.42	8.12%
τ_{R1}	181.10	33.57	18.54%
τ_{R2}	22.84	3.81	16.71%
τ_{R3}	3.46	0.56	16.35%
10 w.t.% CB Specimen			
Constant	μ	σ	CV
b_0	1649.55	97.44	5.90%
b_1	55.19	8.85	16.04%
b_2	77.39	12.23	15.80%
b_3	38.35	9.47	24.69%
τ_{R1}	169.63	61.72	36.38%
τ_{R2}	21.85	9.66	44.21%
τ_{R3}	3.02	1.59	52.72%

Our aim was to prove the hypothesis that the stress relaxation time constant is different to that of the observed resistance relaxation and able to be modelled mathematically. The apparent difference in time constants and the fitting of the data to two different equations show that the stress relaxation is not linearly related to the resistance relaxation shown clearly in Fig. 3.6. To display the non-linear relationship between the stress and calculated resistance within the material they are plotted against each other over 30 sequential relaxation periods of 300s. The non-linear relationship between stress and resistance changes over time for each relaxation as shown in Fig. 3.7, where the data for the first relaxation is displayed in green and the last relaxation in blue.

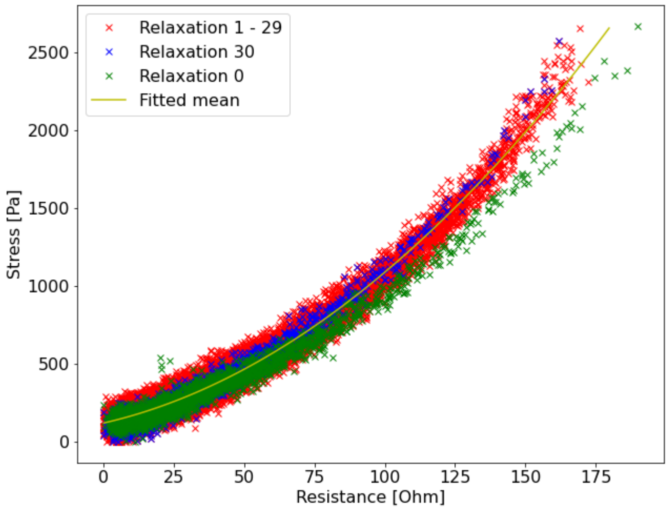

FIGURE 3.7: COMPARING RESISTANCE AND STRESS RELAXATION DATA AGAINST EACH OTHER OCCURRING DURING 30 PULSES OF A 10% STRAIN STEP INPUT FOR A 7.5 W.T.% CB-PDMS COMPOSITE

The stress-resistance relaxation data was fitted to a generic second order polynomial of the form,

$$\sigma(R) = aR^2 + bR + c \tag{3.5}$$

where σ is stress, R is the calculated resistance. When fit to the latter 15 cycles of a 30 cycle 10% strain pulse train of stress relaxation data we get the constant values for a, b and c.

TABLE 3.3: FITTED CONSTANTS AND THEIR MEAN, μ, STANDARD DEVIATION, σ, AND COEFFICIENT OF VARIATION, CV, VALUES FOR 7.5%, AND 10% CB-PDMS COMPOSITE SPECIMENS USING EQUATION 3.5

7.5 w.t.% CB Specimen			
Constant	μ	σ	CV
a	0.055	0.006	11.1%
b	4.146	1.058	25.5%
c	121.845	16.338	13.41%
10 w.t.% CB Specimen			
Constant	μ	σ	CV
a	0.098	0.007	7.48%
b	6.374	0.757	11.87%
c	155.812	38.753	24.87%

Strain Velocity Resistance Relationship

A narrow peak in the apparent resistance has been observed in the collected data when changing from 10% strain to a zero strain. This peak is not present in the stress plot, hence is a proposed characteristic of electrical behaviour only as a function of strain. In previous literature, the effects of the rate of change of strain on apparent resistance of the CB-PDMS material has not been modelled or shown. When the material has finished a tensile cycle of strain and is returning a zero strain state the a component of the resistance, R_p, can be modelled with a second order polynomial. When differentiated, this peak gives a linear function in a similar form of the linear strain curve seen in Fig. 3.8. Hence we form an equation which relates a component of resistance,

$$\frac{dR_p}{dt} = E(\varepsilon)t + c \tag{3.6}$$

where E is a function of strain, $\varepsilon(t)$, and c is an offset bias determined by the initial strain condition. To show the strain velocity resistance relationship, more strain pulse

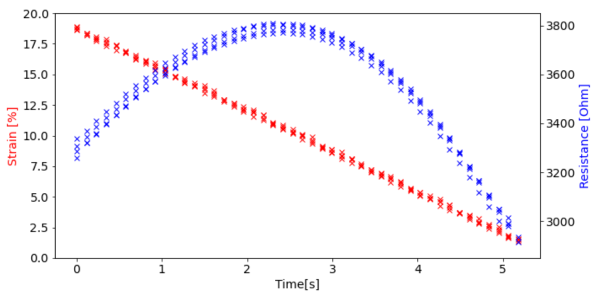

FIGURE 3.8: STRAIN VELOCITY RESISTANCE RELATIONSHIP SHOWING THE SPECIMEN IS RETURNING TO A 0% TENSILE STRAIN STATE FROM 10% AT A STRAIN RATE OF 80mm/s FOR FOUR TESTS FOR A 7.5% CB-PDMS SPECIMEN

train tests of 20% strain were completed. Using 20% strain allowed us to see a sufficient number of data points to observe a trend. The pulses had four repetitions with a range of strain velocities, $\dot{\varepsilon}(t)$, of 40, 80, 120 and 160 mms^{-1}. Using a 7.5 w.t.% CB-PDMS specimen we obtain a relationship that agrees with the strain resistance component equation 3.6. As $\dot{\varepsilon}(t)$ increases through strain speeds so does the magnitude of the resistance peak (i.e. maximum height of the resistance peak - the previous steady state of value resistance) of 400, 510, 569, and 641 Ω for $\dot{\varepsilon}(t)$ of 40, 80, 120 and 160 mms^{-1} respectively. A new model is required which can accurately reproduce the additional decay time constant and small peak features seen in the resistance relaxation data, so that the resistance can inversely calculate the strain in the material.

Repeatability

The resistance relaxation model must be predictable over many strain cycles for use within many high stretch strain sensor application. If the resistance relaxation changes over time this needs is to be modelled. Each test sequence showed that there was a downward trend in the calculated magnitude of resistance for each pulse over time. This downward trend is hypothesized to be due to the accumulation of charge within material over time generated by current source, and was mitigated by using an alternating polarity measurement technique. The reversible current source helped to mitigate the capacitive effects seen, but a general downward trend in resistance was still observed as shown in Fig. 3.9. For every sufficiently long test sequence the material reaches a steady state, after a finite amount of time. The capacitance read across the inner pin electrodes of the material decreased with increasing strain as shown in Table 3.4.

Table 3.4: AVERAGE INNER ELECTRODE CAPACITANCES, C_i, MEASURED FOR VARIOUS STRAIN, ε, VALUES USING A 7.5 W.T.% CB-PDMS COMPOSITE, MEASURED USING AN LCR METER AT 1kHz AND 10kHz

$\varepsilon[\%]$	0	10	20	30
$C_i[pF]$	53	32	24	20

The generalized Maxwell model has been applied to predict the stress relaxation of the CB-PDMS composite and analogously the resistive relaxation seen, which successfully explains a significant fraction of the resistance relaxation seen for a positive strain step input. However, a sudden peak of resistance when changing from +10% strain to 0% is not yet explained, and consideration of temperature and strain history[19] will be useful to confirm the simple mathematical model given as Eqn. 3.6.

In this work, mixing has been performed using a planetary mixer. It has been shown in other works [107, 153] that other mixing methods, such as using a sonication bath and the addition evaporateable solvents, can yield better particle dispersion. A higher degree of CB particle dispersion has also been shown to alter the viscoelastic creep properties [153], and is therefore likely to affect the time constant of resistance.

CONCLUSIONS

In order to improve the accuracy of dynamic strain measurements with CB-PDMS composites a stress and analogous resistance relaxation model was formed. The generalized

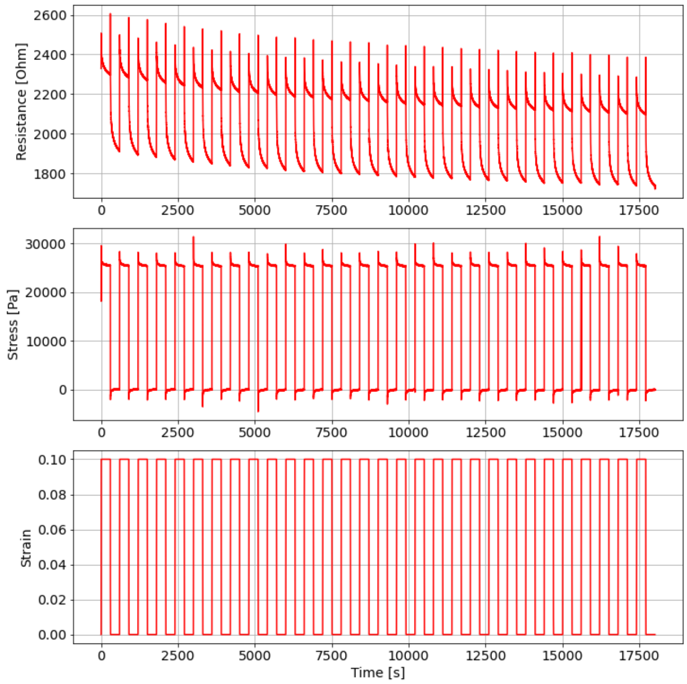

FIGURE 3.9: A TYPICAL TEST SEQUENCE OF A 30 PULSE STRAIN TRAIN RECORDING THE CALCULATED RESISTANCE AND STRESS OF A 7.5 W.T.% CB COMPOSITE

Maxwell model, Eqn. 3.3 was used to fit to the stress relaxation data for three specimen with CB weight percentages of 0, 7.5% and 10%. The CV of the stress relaxation magnitude constants $a_0 - a_2$ were found to be consistently smaller than the CV of the stress relaxation decay time constants τ_{S1} and τ_{S2}, with maximum CV values of 15.45% and 32.54% respectively. All of the stress relaxation model constants increased with increasing weight percentage of CB.

After modelling the stress relaxation, an analogous resistance relaxation model, Eqn. 3.4 was formed and fitted to, displaying similar attributes to the stress relaxation model fit with all of the model constants increasing with increased w.t.% CB. The CV of the analogous resistance relaxation magnitude constants $b_0 - b_3$ were found to be consistently smaller than the CV of the stress relaxation decay time constants $\tau_{R1} - \tau_{R3}$, with maximum CV values of 16.04% and 44.21% respectively.

A model relating the resistance and stress relaxation has been developed using a second order polynomial with all of the constants a, b, and c increasing with increased weight percentage of carbon black. With the models developed we have shown that the apparent resistance relaxation can be modelled, which will enable more accurate estimation of dynamic strain when these materials are applied as sensors.

3.4 A Piece-wise Approach to Modelling Carbon Black Silicone Rubber Composites

One method for understanding the transient behaviour of CPECs is to create a classification system and determine mathematical relationships that can be matched to these transient event. Mersch et al. have classified several shoulder events and the related deformation events, compressive, tensile, and bending. These transient peaks have been observed by several researchers using the similar CBSR materials, however there is no conclusive mathematical model relating these transient peaks to strain in time. This section aims to further classify these transient events and provide a mathematical relationship, for future use with model fitting methods.

3.4.1 Rising Edge Step Response

3.4.2 Falling Edge Step Response

As shown in Section 3.3 there has been a mathematical relationship observed between the falling edge of a strain input and the resultant resistance peak. Consequently a parameter fit study has been completed to determine how to predictably control the resistance peak through a controlled strain input. We can see a repeated property in Figure 3.8 whereby the derivative of the resistance signal seems to be equal to the strain curve.

To prove that there does exist a mathematical relationship between the two signals the relationship first each signal is given a generalised formula. The resistance signal is parabolic Equation 3.7.

$$R_p = A(t - H)^2 + K \tag{3.7}$$

Where strain rate changes the vertical shift, K, time shift, H, and concavity, A, of the parabola.

3.4.3 Strain Rate

3.4.4 Saw Tooth Response

3.5 Characterising Hysteresis

Chapter 4

An Improved an Electrical Impedance Tomography Based Artificial Soft Skin Pressure Sensor

The content from this chapter is predominantly from the manuscript published in the journal Sensors and Actuators A Physical - E-Skin special issue.

ABSTRACT

Using electrical impedance tomography (EIT) to drive a pressure mapping device shows great potential, due to the customisability of the sensing domain and the non-invasive nature of the boundary electrodes. A pressure mapping system has been developed in this work that uses a silicone carbon black nanoparticle sensing domain, giving the domain with a comparable softness to human skin tissue. To take this technology into a commercial application the performance of such an EIT-based sensor must be quantifiable and repeatable. In this work a series of experiments were repeated for various load locations, strains, and carbon black percentages. Capturing this data gave insight into the how the sensing domain performs over time and captured the transient events limiting the sensor. Metrics were determined to quantify the sensor's spatial resolution. A quasi-static conductance-force model of the material was developed with an accuracy of ± 0.78 N. One important metric is temporal resolution, as it is the least quantified performance metric in literature, however can be the most important for some applications. For the sensor domains tested, average settling times of between 19.0 - 44.5 s and 22.5 - 36.0 s were determined for 8 and 9 wt% CBSR samples. A series of randomised test loads gave similar spatial performance results to the structured experiments. This sensor platform shows promise for future applications, with further materials development and processing of data the rise of an artificial biomimmetic pressure sensitive skin is imminent.

4.1 INTRODUCTION

Approximately 1 billion years after the first animals developed mechanosensation [154], evolution has allowed humans to detect pressure through the use of many mechanoreceptors lying within the skin and other organs. Two mechanoreceptors which are desirable to emulate human touch are Merkel's disks and Meissner's corpuscles [155]. Both of which are ubiquitous in human hands and lips for high spatial resolution, low pressure and low frequency touch/pressure events [156]. These mechanoreceptors in a human hand enable object identification and closed loop fine motor control.

With the creation of pressure mapping technology which has the similar soft mechanical properties and sensing qualities to that of human skin many commercial applications requiring human-like touch could be directly fulfilled. This work presents characterisation of a soft mapping pressure sensor which utilises electrical impedance tomography to map resistance changes and subsequently stress changes throughout a soft material surface.

The number of applications that require 2D pressure sensing using a soft surface is extensive. Such applications include: robotic gripper object detection, medical mattresses and cushions, limb prostheses and wearable robotics, sport equipment, smart furniture, and rehabilitation devices. The following characteristics are desirable for each of these applications: force sensitivity, low toxicity, cost-effectiveness, repeatability, and high elasticity. In this work, a system showcasing each of these desirable characteristics has been developed.

The sensor platform utilises a piezoresistive nanoparticle elastomer composite (PNEC) in a thin sheet topology to create an artificial sensitive skin. This artificial skin is composed of a highly elastic piezo-resistive material, and its deformation can be identified through electrical impedance tomography (EIT) for the reconstruction of the material resistivity image. Using 16 boundary electrodes, EIT facilitates the mapping of applied forces on this monolithic homogeneous material. Subsequently, an inverse model is applied to estimate compressive force loads on the material.

Understanding the electro-mechanical properties of the PNEC material is essential for creating an accurate dynamic sensor. When elastomeric composites with conductive particles, such as the PNEC, exhibit viscoelasticity, the degree of hysteresis varies based on the constituents of the composite material [157]. This viscoelasticity is a major limiting factor when using PNECs for EIT-based pressure sensing due to the frequency response lag introduced by the large transient effects seen in the material. In this work these transient phenomena are captured and characterised in the 1D and 2D compressive stress cases.

Various methods and topologies of 2D pressure mapping sensors can be employed for a 2D resistivity measurement. However, many of these methods involve intrusive and intricate electrode placement within the material domain [158–163]. Since the materials utilised in this study are soft, the utilisation of relatively rigid metal electrodes distributed throughout the material would significantly alter the material's electromechanical deformation response. This necessitates use of the non-invasive method imaging method EIT.

4.1.1 EIT Background

To estimate the 2D resistivity of the PNEC a technique called electrical impedance tomography (EIT) was used. EIT allows the generation of a map of impedance values of a thin cross section of a domain under test (DUT). EIT uses a set of boundary electrodes to pass known electrical currents and measure voltages along the boundary of the DUT. From these known current injections and voltage measurements, an ill-posed inverse problem can be defined. To obtain an EIT image reconstruction three key steps are required: data acquisition, forward modelling, and inverse problem solving. A constant current can be employed to capture solely the resistance values of the DUT or as an AC signal to sweep through a range of frequencies to capture impedance data.

The forward problem in EIT is a well-posed mathematical problem, so linear algebra can be employed for obtaining electric field data for a DUT of known conductivity and a known current injection. Utilising a mesh-based coordinate system and FEM, proves to be an efficient solution for the forward model, accommodating diverse shapes. Solving the forward problem entails applying Maxwell's electromagnetic formulae to determine how an electric field would propagate through the DUT, considering the DUT conductivity. An initial estimate of the DUT resistivity is necessary for the first step of an EIT algorithm. Once the EIT forward model is solved, EIT inverse problem can be solved iteratively using the forward problem's solution. This inherently unstable problem requires optimisation algorithms and regularisation to create and linearise a solution [164–167].

Once the EIT reconstruction algorithm has been tuned for an application as desired, often post-processing is completed on the reconstructed EIT image for filtering and to capture data specific for the application. A consortium of experts in the field of medicine and biomedical imaging have constructed metrics for quantifying the quality of an EIT reconstruction as shown by Adler et al. [168] and their GREIT (Graz consensus Reconstruction algorithm for EIT) performance metrics. Researchers who have used EIT pressure sensing purposes have also developed performance metrics, most of which agree with the GREIT metrics [105, 160, 169**?** –172]

4.1.2 Related Work

Artificial skins are not a novel subject there are many different methods for localising loads in two-dimensions on a soft domain. The limiting factors found with non-EIT based methods of pressure mapping were the size discretely sensed regions, also known as sensels, is limited by various factors in the fabrication process and the bulk of electrode wires required. This bulk is exemplified high electrode-to-sensel ratio. Example load mapping technology include, optical [173–175], piezoresistive [162, 176, 177], capacitive [178], and magnetic [116]. Each of which have been compared in Table **??**.

Other attempts at creating artificial sensitive skins using EIT have been shown in a review by Silvera-Tawil et al. [160]. This review provides adequate evidence to display interest in the field; however, there is still no commercial EIT-based pressure sensor that is comparable in terms of spatial and temporal resolution, to commercially available non-EIT-based 2D pressure sensors. One of the earliest applications of EIT to an elastic piezo-resistive domain was achieved by Knight and Lipczynski [179] in 1990. Since this application, several other similar systems have been created using EIT and similar pressure sensitive fabrics or elastomeric materials[105, 160, 172, 180–183]. A comparison of similar devices is given in Table **??**. None of these researched devices focus on using a material with similar softness, and quantify the stress data captured in real-time like this work. All of the referenced 'EIT' soft sensors employ electrical resistivity tomography (ERT), however, the term ERT is most commonly associated with geological subsurface imaging applications, henceforth, EIT is be used in place of ERT in this work.

4.2 METHODOLOGY

To substantiate the applicability of Electrical Impedance Tomography (EIT) with a monolithic PNEC sample, we fabricated the material for testing. The material needed to adhere to specific requirements: highly elastic, high yield strength, low resistivity, high piezoresistivity, non-toxic, and be a low Shore hardness of 5A - 25A akin to human soft tissue [40, 160, 184, 185]. Additionally, a system of devices was devised to facilitate EIT measurements which concurrently captured force, strain, and timestamps for each measurement. Lastly, to evaluate the sensor's suitability for diverse applications, spatial, temporal, and localised force sensing performance metrics were quantified.

4.2.1 Fabrication

The fabrication of the piezoresistive composite materials, as described and justified in our previous work [157], involved dispersing 8 and 9 wt% of carbon black (CB) nanoparticles in a silicone rubber (SR) matrix. Because of the difference in fabrication processes seen in literature [186, 187] and degree of dispersion generating variability in the percolation, an iterative trial and error approach using the starting point found in literature was used to get 8 wt % and 9 wt % values for CB in SR. Within this range the material was sufficiently conductive while maintaining mechanical strength through sufficient elastomeric cross-linking. Previous research indicates that there is a weight percentage at which the gauge-factor/piezoresistivity is at a maximum within a similar range used in this work [188, 189]. The composite, designated as the domain under test (DUT), was created using 50 nm average diameter XC 72R CB nanoparticles (Cabot, Alpharetta, USA) in a Dragon Skin 10 NV silicone rubber matrix (SmoothOn, Macungie, USA). Homogeneous dispersion was ensured using an ARV-310 vacuum planetary mixer (Thinky, Tokyo, Japan).

TABLE 4.1: DUT mechanical characteristics and electrical characteristics

Sample	**CB wt** [%]	$\mathbf{R_{int}}$ [$k\Omega$]	**E** [kPa]
SR	0	$> 1 \times 10^9$	186.16
CBSR	8	18.1 ± 9.8	132.5
CBSR	9	4.5 ± 1.4	98.1

A CBSR sample showing the circular sensitive region with the pin electrodes developed is shown in Figure 4.1.

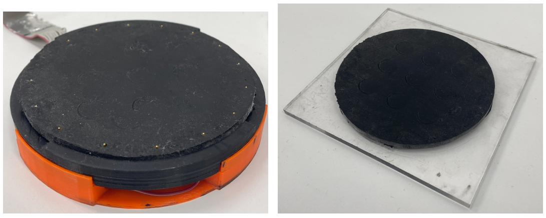

FIGURE 4.1: Left: Example of a CBSR sensing domain with gold pin electrodes penetrating material surface around the boundary on top of the rigid sensor holder (orange/black). Right: CBSR sensing domain.

4.2.1.1 Localised Stress Testing

Quantitative results are required for spatial quantification of the EIT image reconstructions. A cylindrical force applicator head with a diameter of 13 mm and area of 133 mm^2 was used to apply the nine compressive loads shown in Figure 5.8.

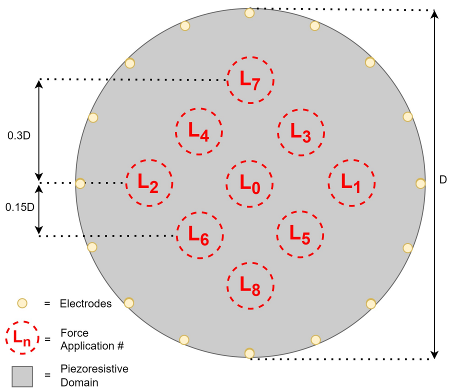

FIGURE 4.2: Load application areas used for compressive stress testing shown numerically in order of application.

4.2.1.2 EIT Measurement

At its core EIT usually requires a current or voltage source, one or multiple voltmeters, and a switching device. When integrating a mechanical pressure validation system a force applicator (CFA) and is also required to capture data simultaneously. The system architecture and DUT electrical connections are shown in Figure 4.4.

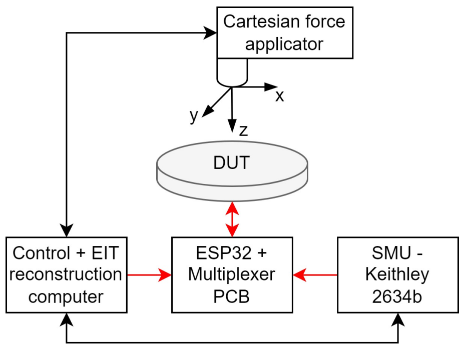

FIGURE 4.3: Architecture of the Cartesian force applicator setup with red arrows being analogue power lines and black arrows being digital data lines

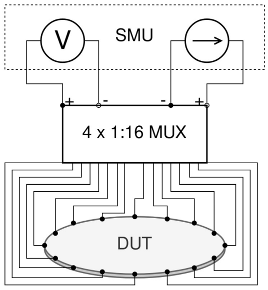

FIGURE 4.4: Wiring diagram for sensor connection to 4:16 multiplexer and SMU

4.2.2 1D Material Characterisation

Prior to utilising CBSR materials as a 2D pressure sensor, the piezoresistive properties were analysed in one dimension to establish resistance-stress/strain relationships for each CBSR sample. This 1D material testing was conducted using the Cartesian force applicator in conjunction with the SMU. The stress-strain relationship of the material was determined in previous work and shown in Table 4.1. The 1D analysis gave quantitative insight into the material resistivity response to strain in different known areas of the Device Under Test (DUT).

4.2.2.1 Quasi-static Piezoresistivity

To determine the piezoresistivity or gauge factor of the material, pin electrodes were pierced through the CBSR samples so that the pin electrodes were parallel and at a distance of 35 mm from each other. The pins were 2.5 mm from each end of the sample. A 2634b source measure unit (Keithley, Solon, USA) was used to apply a constant current of 1 mA between the two pin electrodes while ten compressive loading cycles were applied. The ten loading cycles were applied at strains of 5, 10, 15, 20, 25, and 30%, with a duty cycle of 50% and period of 120 s. Loads were applied using the Cartesian force applicator with a 20 mm x 20 mm square flat force applicator head. The strain rate was kept at a constant 16.67%.s^{-1} to dampen the amplitude of transient effects as proven in previous work [157].

When using this material to estimate stress based on resistance, any transient effects that are not correlated between resistance and stress must be accounted for. To obtain a stress reading from this PNEC CBSR material using the quasi-static model given in Equations 4.1 and 4.2, transient events were ignored, so only the steady-state conductance of the material was utilised.

$$\frac{\Delta\rho}{\rho_0} = \alpha_\sigma \sigma + \beta_\sigma \tag{4.1}$$

$$\frac{\Delta\rho}{\rho_0} = \alpha_\varepsilon \varepsilon + \beta_\varepsilon \tag{4.2}$$

Where α and β are the linear fit parameters, σ is the compressive stress, ε is the strain, $\Delta\rho$ is the change in conductance, and ρ_0 is the original material conductance.

4.2.2.2 Transient Piezoresistivity

There are two main piezoresistive events that occur during these compressive stress pulse response experiments. They are the compressive loading and unloading transients. Both of which result in stress relaxation and resistance relaxation behaviour until a steady-state resistance is reached. The stress relaxation can be approximated by a generalised Maxwell linear viscoelastic model [190]. A two component model was found to fit all curves without overfitting, the relaxation model from a step input is given in Equation 4.3.

$$G_2(t) = a_o + a_1 e^{-t/\tau_1} + a_2 e^{-t/\tau_2} \tag{4.3}$$

Where $G_2(t)$ is the stress relaxation function, a_0 is the relaxation offset, a_1 & a_2 are the magnitude weightings for each time constant τ_1 & τ_2. Equation 4.3 was used analogously for the resistance relaxation. To ensure repeatability of the experiment the ten loading and unloading events were fitted using equation 4.3 to the each relaxation, then the R^2 goodness of fit was compared for all of the relaxations.

An important temporal characteristic of this system is the settling time, t_s, given a strain step input. In this system the resistance step response settling time was the time taken to reach and stay within a specified tolerance about final steady-state resistance, given a strain step input. The tolerance chosen is about the steady state was $\pm$ 15%.

4.2.3 Sensor Performance Metrics

To ensure that the resistance/conductance image reconstructions which will form stress maps are valid solutions, the quality of the reconstructions needs to be quantified computationally. The purpose of this section is to describe various metrics used for sensor validation. These metrics measure the spatial performance, temporal performance, and localised force sensing performance. Many of the spatial and temporal performance metrics have been taken and adapted from Adler et al. [168] and their GREIT (Graz consensus Reconstruction algorithm for EIT) performance metrics.

4.2.3.1 Pre-processing

To ascertain the occurrence of a piezoresistive event in the material, it is necessary to identify a change in resistivity that surpasses the noise floor level. This precaution is taken to differentiate between a stress compression event and potential noise artefacts. A threshold was established to eliminate the noise floor, thereby isolating the loading signal and any noise or artefacts generated by the loading signal(s).

A second threshold filter was implemented to compensate for the regularisation of the reconstruction using a percentage of the largest peak observed in the sensor image domain. The percentage threshold value used in previous work has been 25, 50, 60, 70, 75% of the maximum domain amplitude [160, 168, 169]. In this work percentage threshold masking have been applied for comparison. To validate the best percentage threshold, these thresholds were completed for a CBSR 8 and 9 wt% PNEC under nine successive loading events comparing the mean of the three main performance metrics given in Section 4.2.3.2. After these threshold masks have been applied to the 2D EIT images, blob(s) are observed as the sensed regions-of-interest. In this work the term 'blob' refers to an amorphous 2D shape made of several aggregated finite mesh elements. These blobs are usually observed after percentage threshold masking of an EIT image reconstruction.

4.2.3.2 Spatial Performance

The three main metrics of spatial performance are the centroid or centre of 'mass' error, E_{CoM}, the detected area overlap A_{OL} value, and the fit of the detected blob relative to the force input, the shape distortion, *SD*.

The E_{CoM} was found using:

$$E_{CoM} = \sum_{i}^{N_b} e_{CoM_i} \times \frac{e_i}{e_{total}} \tag{4.4}$$

Where N_b is the number of elements in the threshold masked blob, e_{CoM_i} is each individual element centroid, e_i is the i^{th} blob element resistance value and e_{total} is the sum of all of the blob element resistance values. This equation can be easily be inverted for images containing conductance elements in place of resistance elements. The nearer the E_{CoM} value is to zero, the better the reconstruction in regards to localising the sensed region.

The A_{OL} was found using:

$$A_{OL} = 100 \times \left[\frac{\left(\sum_i^{N_b} A_{e_i}\right)}{A_{FA}} + \frac{\left(\sum_i^{N_b} A_{e_i}\right)}{A_b} \right] \Big/ 2 : e_{CoM_i} \in \Omega_{FA} \tag{4.5}$$

Where A_{e_i} is the area of an element and Ω_{FA} is the domain of the force applicator area. A_{FA} and A_b are the areas of the force applicator and sensed region respectively. The closer the A_{OL} is to 100%, the better the overlap of the estimated and actual load application.

The *SD* was found using:

$$SD = \left[\sum_{j}^{N_p} (\|F_{CoM} - P_j\|_2 - r_{FA})^2 \right] \Big/ N_p : P_j \in L_b \tag{4.6}$$

Where N_p is the number of mesh nodes on the perimeter of the blob, F_{CoM} is the force applicator CoM coordinates, P_j is a node in the set of blob perimetral nodes, L_b, and r_{FA} is the radius of the force applicator head. The *SD* is essentially the mean square error of the force applicator perimeter and sensed region perimeter taken radially from the force applicator centroid.

4.2.3.3 Temporal Performance

A core problem with using soft PNECs is the temporal resolution they can provide can be limited by the viscoelasticity in the material and how it interacts with the conductive network in the material. This section provides insight into how to determine the frequency response of the material, by observing the relaxation settling time of the material. The maximum time taken to reach a steady-state resistance after a stress event dictates the frequency at which the material can sense stress events. To determine the time taken to reach a steady-state, a variety of compressive stresses and strains at the loading locations, L_0-L_8, of each DUT are observed.

To determine whether the resistance relaxation observed in the 1D case matches the relaxation of the reconstruction in 2D, the 1D and 2D relaxation settling times were compared to validate whether similar frequency responses were being observed. The EIT measurement equipment was designed such that the reconstruction frequency of 0.4 Hz can capture these transient events observed triggered in the CBSR samples, which are typically in the order of tens of seconds.

From the blob localisation described in section 4.2.3.2 the resistance relaxation data was extracted by plotting the sum of the blob resistance. Similar to the 1D case, the relaxations for stress loading, resistance loading, and resistance unloading scenarios are captured and compared for each CBSR with CB weight percentages of 8 and 9 wt%. The blob resistance relaxation was compared to relaxation deduced from the total image domain resistance to ensure that the only the transient event from the area being loaded was being observed.

4.2.3.4 Localised Force Sensing Performance

As discussed in Section 4.2.2.1, a quasi-static function, Equation 4.1, has been generated that gives a stress based on 1D steady-state conductance measurements. This quasi-static function was applied to the DUT 2D reconstruction to obtain a stress map of the material. To determine the minimum detectable stress of the sensor the conductance noise floor values were input into the linear quasi-static Equation 4.1.

To obtain the stress estimate, $\hat{\sigma}_j$ and hence force estimate given a known input stress and force, the following steps were completed for each CBSR sample:

1. Determine the most likely sensed region:
   (a) An EIT reconstruction image of a loaded DUT of a particular strain, ε_j, at a steady-state conductance was found. Each element having a change in conductance value, $\Delta\rho$, in units mS.

(b) Complete threshold percentage mask on image to localise the sensed region blob(s).

(c) The centre of mass error, E_{CoM}, between each blob and the actual force application CoM was calculated. The blob domain with the smallest E_{CoM}, Ω_s, is chosen for the following steps.

2. Equation 4.1 was rearranged to get an original conductance estimate for each element:
$$\rho_0 = \frac{\Delta\rho}{\alpha\sigma + \beta} \tag{4.7}$$

3. The mean ρ_0 and standard deviation of all of the elements in Ω_s were found.

4. Steps 1 to 3 were repeated for each strain, ε_j, applied and the mean, $\rho_0(\varepsilon_j)$ and standard deviation were calculated.

5. The mean of all $\rho_0(\varepsilon_j)$ across all strain values (i.e. $\varepsilon_j = 5, 10, 15, 20, 35, 30\%$) was calculated as $\bar{\rho}_0$.

6. $\bar{\rho}_0$ was then substituted into Equation 4.1 as ρ_0, which was rearranged for stress to obtain the stress estimate as a function of mean change in conductance, $\hat{\sigma}_j(\Delta\bar{\rho}_j)$, of the sensed blob domain, Ω_s.

4.3 RESULTS

In the following Sections 4.3.1.1-4.3.3.2 the EIT image pre-processing, spatial, temporal, and localised force sensing performance metrics are displayed and quantified. First the steady state electrical noise, σ_n, and noise figure, NF, were determined, as given in Table 4.2. The NF value being a common metric showing noise amplification as a consequence of the EIT algorithm as used by Adler et al [168].

TABLE 4.2: DUT noise figure, NF, and noise, σ_n, at steady-state

CB wt%	**NF**	σ_n [mS]
8	1.20 ± 0.17	0.69
9	1.15 ± 0.11	0.48

4.3.1 1D Material Characterisation

To generate a 2D pressure map from the EIT reconstructions a 1D material electromechanical characterisation was required. The 1D electromechanical relationship can then be extended to form an electromechanical relationship in 2D.

4.3.1.1 Quasi-static Piezoresistivity

Given known strain input data, and measured stress and conductance change output data, a fit is shown in Figure 4.5. The gradient of the linear fit, i.e. the gauge factor, for the CBSR 8 wt% and 9 wt% was calculated as 0.6 and 0.2 respectively. Note that in the 9 wt% relative conductance data the standard deviation of the 5% strain data was similar to that of the mean, hence the linear range of 10 - 30% strain was considered when fitting the curve.

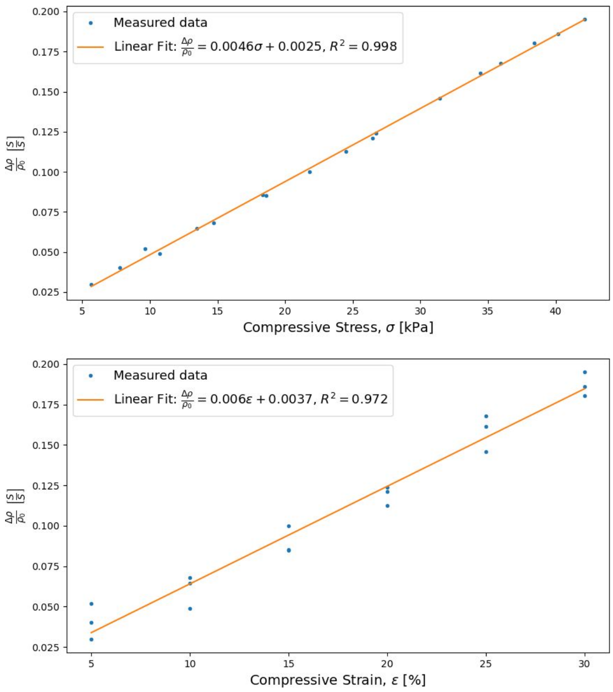

FIGURE 4.5: Conductance change vs. stress (top) and strain (bottom) data and fitted curves for 8 wt% CBSR.

4.3.1.2 Transient Piezoresistivity

The transient piezoresistive effects observed within a PNEC limit the frequency response of the sensor. An example of the transient response of the material to a repeated compressive strain pulse input is displayed in Figure 4.6, clearly showing the stress relaxation of the material due to its viscoelasticity. In Figure 4.7 a loading event is shown with the related stress and resistance relaxation curves. The unloading event similarly has a relaxation period for both stress and resistance in the loading case. Unlike the loading stress transient, the resistance transient has a spike during the unloading relaxation event seen in Figure 4.7. This rising edge and peak of this spike are ignored and the resistance relaxation edge is characterised. For each stress relaxation Equation 4.3 was fitted to the data. Analogously the same was done for the resistive relaxation events observed.

The fitted parameters were found for both 8 and 9 wt% CBSR samples, giving an indication of t

The settling times of the resistance relaxations give an indication of the frequency response of material. Thus, parameters were fitted to a series of relaxations using Equation 4.3, then a series of fit parameters could be used to determine a mean fit. The mean fit was then used to determine the mean settling time over each ten loading events and

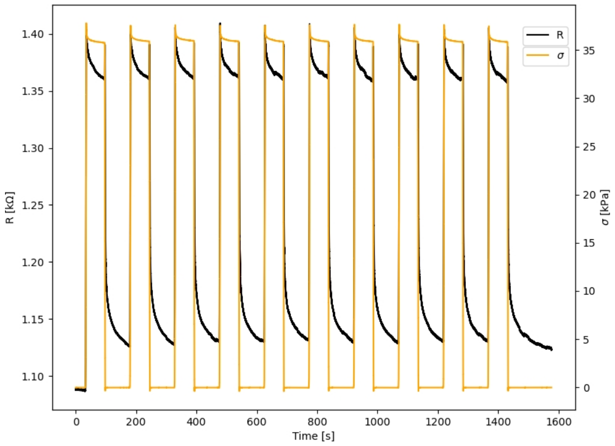

FIGURE 4.6: Compressive loading applied to the CBSR 8 wt% DUT for 10 loading events of 25% strain.

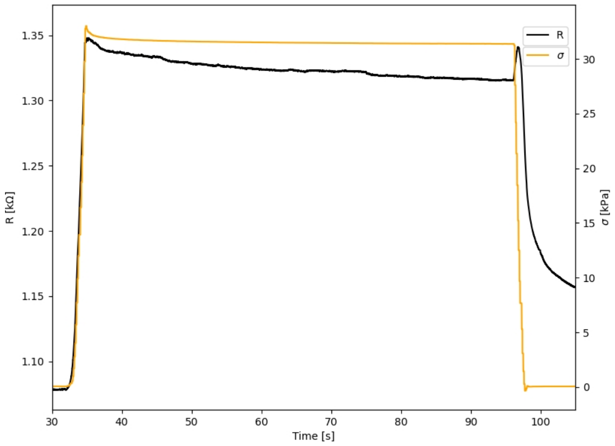

FIGURE 4.7: Compressive loading and unloading transients for CBSR 8 wt% material undergoing a 20% strain pulse from the first pulse given in Figure 4.6.

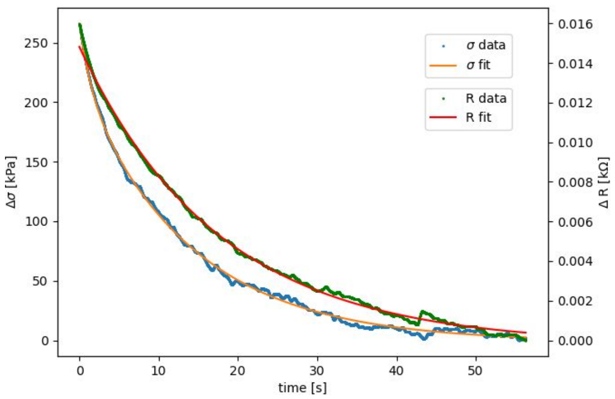

FIGURE 4.8: The fourth 1D load event, L_3 on the CBSR 8 wt% sample using 5% strain showing a stress, σ and resistance, R, relaxation event and their corresponding fitted curves.

each of the six strain values. The mean relaxation settling times were compared for each CB weight percentage as shown in Appendices **??** and **??**.

4.3.2 Sensor Performance Metrics

To validate this 2D pressure sensing platform for specific applications the limits of the sensor must known. Metrics to analyse and quantify the limits, sensor noise and spatial, temporal, and stress performance metrics are given in this section.

4.3.2.1 Pre-processing

The noise floor limits the detection of small forces. First the noise floor was found from the no load steady-state of material. The maximum noise from the first eight frames was found and this maximum was subtracted from all contiguous images in the time series experiment.

After a noise mask has eliminated the steady state noise floor, different percentage thresholds can be used to compensate for different regularisation and different material push area edge softness as shown in Figure 4.9.

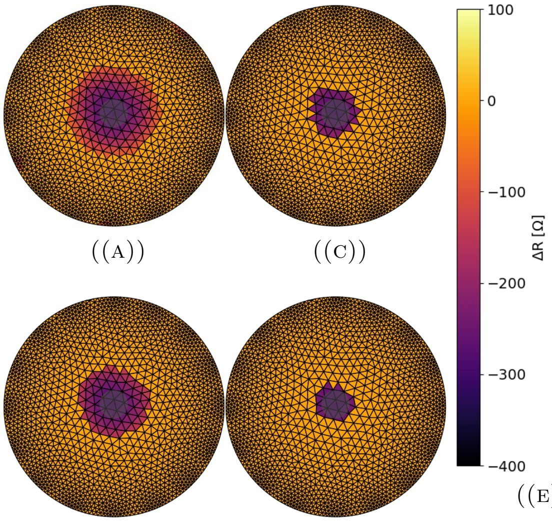

((A)) ((C)) ((B)) ((D)) ((E))

FIGURE 4.9: A series of threshold percentage masks (a) 25%, (b) 50%, (c) 75, and (d) 85% for the same reconstruction given in Figure **??**. (e) is the resistance change scale bar.

The threshold masked image blobs and the force applicator shapes in Figures 4.9(a) - 4.9(d) are compared and quantified in the following section.

4.3.2.2 Spatial Performance

To properly determine where the perimeter of a load is multiple threshold mask filters were applied. To validate the threshold mask percentages the three main performance characteristics were displayed as separate time series for each material, each applied strain, and each threshold percentage mask. These time series show how each metric changed over the course of a loading test sequence and how the metrics vary across the surface of the DUT. An example comparing this time series data for two instances where a 20% strain pulse train was applied to a the nine loading locations with multiple threshold mask percentages is shown in Figures 4.10 and Appendix **??** for for 8 and 9 wt% CBSR samples respectively.

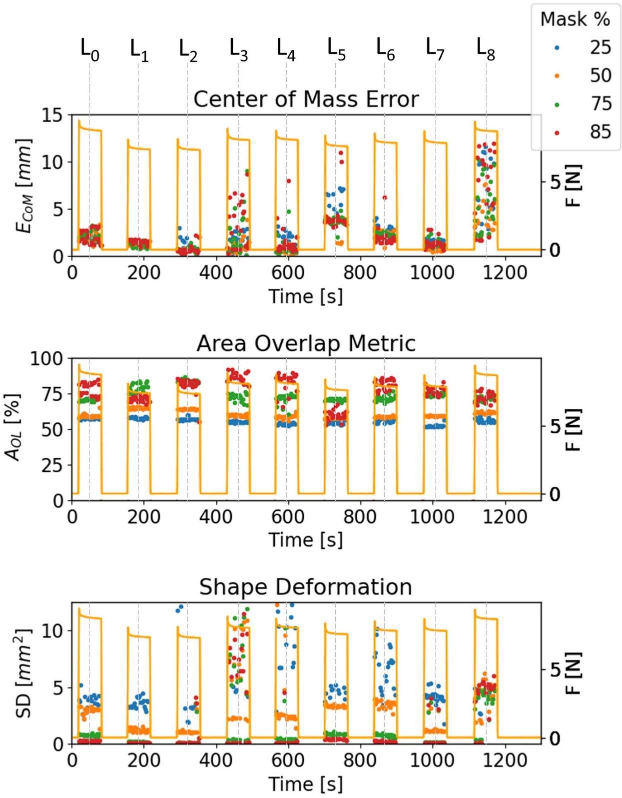

FIGURE 4.10: Spatial performance metrics comparing threshold percentages of 25, 50, 75, and 85% for a 8 wt% CBSR sample being loaded with 20% compressive strain in nine areas, L_{0-8}, shown in Figure 5.8. The force time series plot data is light orange.

The percentage threshold masks from 25 - 85% were compared by finding the mean of all of the spatial performance metrics for each strain from 5 - 30%. The mean and standard deviation for each of these metrics from the data shown in Figure 4.10 is given in Tables 4.3 and 4.4.

TABLE 4.3: CBSR 8 wt% mean and standard deviation for spatial performance metrics across of a nine loads, L_0-L_8 and strain value 20%.

% thresh	E_{CoM} [mm]	A_{OL} [%]	SD [mm^2]
0.25	4.1 ± 6.3	53.3 ± 15.3	10.4 ± 9.3
0.5	3.3 ± 6.3	57.5 ± 16.3	3.6 ± 4.4
0.75	3.8 ± 6.3	69.6 ± 19.8	2.4 ± 5.8
0.85	4.1 ± 6.4	72.5 ± 21.7	2.4 ± 6.5

TABLE 4.4: CBSR 8 wt% mean and standard deviation for spatial performance metrics of nine loads, L_0-L_8, a 85% percentage threshold mask, and strain value 20%.

Load	E_{CoM} [mm]	A_{OL} [%]	SD [mm^2]
L_0	2.05 ± 0.70	80.39 ± 4.19	0.28 ± 0.01
L_1	1.53 ± 0.23	72.32 ± 1.74	0.12 ± 0.01
L_2	0.67 ± 0.41	83.00 ± 2.38	0.48 ± 1.16
L_3	3.29 ± 2.17	87.93 ± 2.68	5.25 ± 3.78
L_4	1.44 ± 1.61	84.81 ± 5.78	2.76 ± 5.65
L_5	4.43 ± 2.09	61.08 ± 3.29	7.39 ± 16.31
L_6	2.03 ± 1.05	82.19 ± 3.55	3.14 ± 8.57
L_7	1.49 ± 0.56	77.68 ± 2.46	0.66 ± 1.25
L_8	6.95 ± 3.67	73.69 ± 3.60	3.78 ± 2.01

4.3.3 Randomised Location and Strain Testing

In a real world application the sensor platform in this work will likely experience a large range of unknown loads in various locations. To ensure that the device operates in a similar fashion to that seen in the structured experimental data, a randomised experiment was completed. The randomised experiment loads were at ten randomised radii, r_{rand}, angles, θ_{rand}, and strain values, within the ranges, 0 - 40% of the domain radius, 0 - 360°, and 5 - 30% respectively.

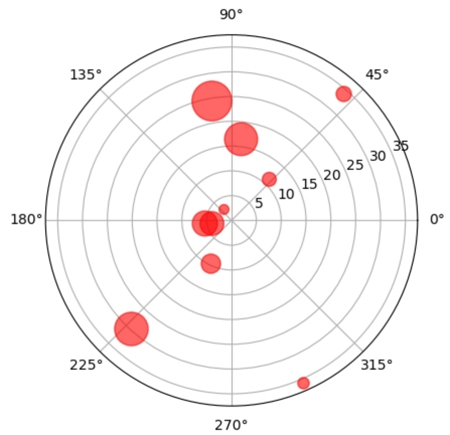

FIGURE 4.11: The ten random load point locations, L_{rand} and random strain values proportional to rec circle size as shown on a polar plot.

Spatial performance metrics for these tests are given in Tables 4.5 and **??** with the load points and their magnitudes shown diagrammatically in Figure 4.11. A pseudo-random number generator with a uniform distribution was used for all randomly generated data.

TABLE 4.5: CBSR 8 and 9 wt% mean and standard deviation for E_{CoM} spatial performance metrics of ten random locations, L_{rand} and random strains ε

L_{rand} (r, θ) [mm, °]	ε [%]	8wt% E_{CoM} [mm]	9wt% E_{CoM} [mm]
(5.4, 10)	17.9	3.1 ± 0.7	3.1 ± 0.5
(29.8, 337)	24.0	1.9 ± 0.4	5.0 ± 0.6
(4.2, 317)	17.0	7.9 ± 2.2	9.0 ± 1.0
(34.0, 70)	10.9	6.0 ± 3.5	2.9 ± 0.5
(35.8, 137)	8.1	13.9 ± 0.6	7.7 ± 4.6
(9.6, 55)	13.8	6.0 ± 1.0	10.3 ± 4.4
(2.8, 260)	7.0	12.0 ± 8.1	28.7 ± 10.9
(11.2, 114)	10.0	5.1 ± 1.2	12.0 ± 1.9
(24.6, 241)	28.5	2.3 ± 0.2	2.4 ± 0.2
(16.6, 253)	23.6	3.1 ± 0.4	7.1 ± 0.5

4.3.3.1 Temporal Performance

Temporal performance is crucial for time sensitive applications and the settling time of the sensing material domain must be known to apply a quasi-static force model. The fitted stress and resistance relaxation parameters were found for both 8 and 9 wt% CBSR samples, giving an indication of the frequency response of material across all experiments. To ensure a good fit all fits with an R^2 value less than 0.85 were eliminated.

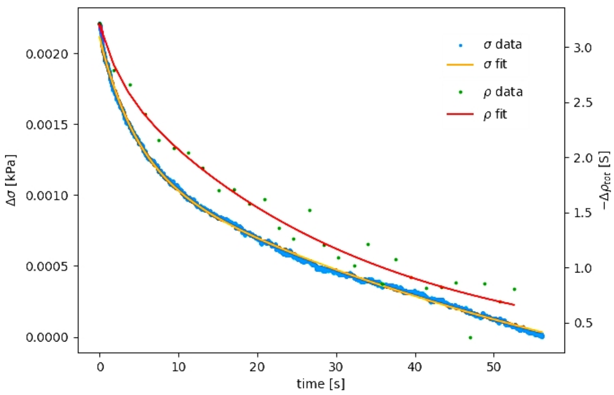

FIGURE 4.12: EIT load event L_0 on the CBSR 9 wt% sample using 30% strain showing a stress, σ and conductance, ρ, relaxation event and their corresponding fitted curves.

The mean settling time for each strain was calculated across relaxations for all strains, all 9 locations, and all 3 trials. The settling times were compared for each CB weight percentage as shown in Appendices **??** and **??**.

4.3.3.2 Localise Force Sensing Performance

To determine the localised force sensing performance the linear quasi-static Equation 4.1 was applied to the percentage threshold masked image blobs developed in section 4.2.3.2.

To determine the force sensing limits of the material, the force estimated erroneously due to the EIT reconstruction noise floor must be determined. The noise floor is the noise observed over a time series of EIT images when the DUT has zero load applied and there are no resistive transient effects present. The noise floor, $\Delta\rho_n$, of unloaded relaxed 8 and 9 wt% CBSR DUT conductance images were calculated as ± 0.33 and ± 0.34 μS respectively. An average DUT inter-electrode conductance, ρ_{int}, of 55.3 and 222.2 μS was derived from Table 4.1 for CBSR 8 and 9 wt% respectively. A relative change of conductance value, $\frac{\Delta\rho_n}{\rho_{int}}$, was then calculated as 5.97×10^{-3} and 1.53×10^{-3} μS for CBSR 8 and 9 wt% respectively. From the quasi-static piezoresistivity Equation 4.1 and the fitted quasi-static piezoresistivity parameters found in Section 4.3.1.1, we calculated the mean force approximation error as 0.17 N for both CBSR 8 and 9 wt%.

The force estimation from the inverse quasi-static Equation 4.1 was compared to the actual force loaded onto the DUT as measured by the force applicator loadcell. Figures 4.13 and 4.14 show data from load applications in the centre (L_0) of the respective 8 and 9wt% CBSR DUTs with a force estimation standard deviation of ± 0.78 and ± 0.81 N respectively.

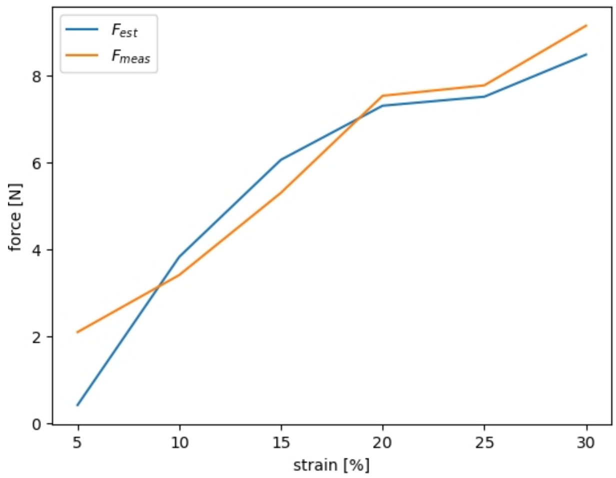

FIGURE 4.13: Comparing force estimates, F_{est}, and actual force measurements, F_{meas}, for 5 - 30% strain centre loading events at L_0 for the EIT sensor system for 8 wt% CBSR

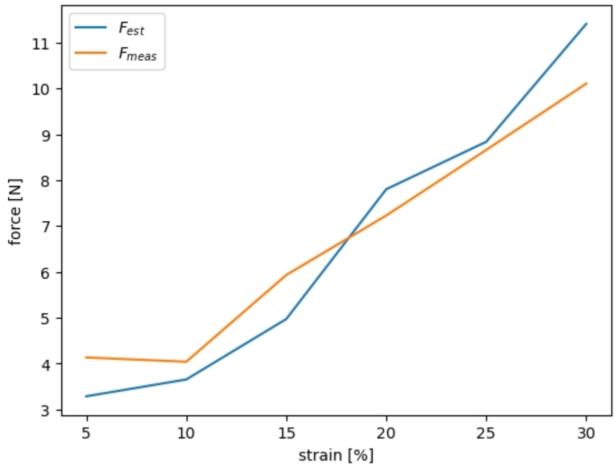

FIGURE 4.14: Comparing force estimates, F_{est}, and actual force measurements, F_{meas}, for 5 - 30% strain centre loading events at L_0 for the EIT sensor system for 9 wt% CBSR

4.4 DISCUSSION

Potential applications that emulate human-like skin pressure sensing characteristics require a forms of quantification to compare the technology to the specific requirements. This work quantitatively characterises performance metrics to help facilitate that comparison and optimisation process. The sensor developed could be likened to slow acting mechanoreceptors within human skin, such as Meissner's corpuscles and Merkel's discs, which combined can detect static pressure, and high resolution touch. For other EIT-based pressure mapping applications to be realised, the metrics developed in this work are some of the core metrics required to determine which soft sensing domains are suitable and are their limits.

4.4.1 Quasi-static Piezoresistivity

To make a low-frequency response load sensor, a quasi-static piezoresistive linear model was created as shown in Section 4.3.1. However, this model is only valid for sufficiently slow pressure applications or after a sufficiently long time period. This time period is determined by the largest expected steady-state relaxation time for the material shown in 4.3.1.1

4.4.2 Pre-processing

The two steps of a noise threshold mask and a percentage threshold mask successfully filtered noise and EIT reconstruction related noise artefacts. The favoured percentage threshold mask chosen for further metrics testing was 85% as this gave the lowest average E_{CoM} and *SD* values from the across all strains applied across all nine loading points.

In the experiments often a blob detection from a previous load will be present in a subsequent load, as expected due to the resistive relaxation. Feature detection could be added in future to ensure that only transients similar to those seen in the initial formation of a blob would signify that the blob is to be analysed. Concurrently, each blob could be tracked individually to determine whether it is a noise artefact or an actual sensed region depending on it's behaviour.

4.4.3 Performance Metrics

To develop sensing domains for future applications, the sensing domains may need take into account certain prior information about the limits of the system.

For example, human hands and feet have some of the highest density of mechanoreceptors in the body. Lower density regions of mechanoreceptors in humans include the back and chest [155]. Higher spatial resolution is require for emulating the pressure mapping of a human hands and feet, compared to the human back and chest. However, the pressure sensing range required by the human hands may be lower than that required by the human feet.

Using this prior information, we can validate the appropriate sensing domain characteristics that give a suitable performance for each different application.

Depending on the application of the sensor the importance of each temporal, spatial, and force sensing performance metrics could all vary.

4.4.3.1 Spatial Performance

All spatial performance metrics, E_{CoM}, A_{OL}, and *SD* are key indicators of whether a loading event has been localised correctly.

The A_{OL} gives a value out of 100 for a certain detected blob. This value is penalised for false positive and true negative elements that overlap (or not) with the force applicator area.

It is important to note, when a force is applied in an small area of a domain, however a blob has been detected over the majority area of the domain, a A_{OL} value of $\leq 50\%$ will be given although the blob detection could be completely false. Although the detected blob and force applicator are 100% overlapping the amount of false positive (i.e. blob elements not overlapping with force applicator area) could cover the rest of the DUT, potentially giving a value nearer to 50% than 0%. From this it must be recognised that this metric does not represent a linear relationship between A_{OL} and the quality of the reconstruction. So the scale of the A_{OL} value to quality relationship was determined empirically as:

$$0 \leq A_{OL} \leq 50\% = \text{Likely Poor}$$

$$50 \leq A_{OL} \leq 70\% = \text{Ok}$$

$$70 \leq A_{OL} \leq 100\% = \text{Good}$$

The *SD* is the mean square error between the force applicator perimeter and sensed region perimeter taken radially from the force applicator centroid, so will likely be lower with a low E_{CoM} and a higher A_{OL}. The closer the *SD* value is to zero the more accurately the shape of the load area applied has been sensed. The *SD* metric is also affected significantly by the quantisation error depending on the mesh coarseness.

Comparing the different percentage threshold masks for the experiment shown in Figure 4.10, it was determined that each percentage mask of 50%, 75%, and 85% gave showed the spatial performance for the E_{CoM}, *SD*, and A_{OL}. However, the standard deviation of these values is comparable to the mean itself therefore looking at the mean performance metric value in each location was shown in Table 4.4. The lowest E_{CoM} was found to be 0.67 ± 0.41 mm, at L_2. The highest A_{OL} value was found to be $87.93 \pm 2.68\%$. The lowest *SD* value was found to be 0.12 ± 0.01 mm^2 at L_1.

The CBSR 8 wt% samples gave better performance metric results than the 9 wt% samples due to the residual transient effects of previous load events as exemplified in Figure **??**. This will be mitigated in future by using a blob separation algorithm whereby each sensed-region/blob is given a weighting based on its appearance time, size, decay characteristic, and performance metric values.

The spatial performance metrics are useful for quantifying future testing with irregular load application area shapes and multiple loading events in future testing to validate a variety of irregular and multi-load test cases. Performance metric inconsistencies in the different load locations show that the electro-mechanical characteristics of the material is varies throughout the material. These metrics would all contribute toward a calibration step to compensate for material inhomogeneity, allowing for a range of materials to be used for the sensing domain.

4.4.3.2 Temporal Performance

Many applications require a minimum frequency response hence a temporal study was completed to characterise the transient effects limiting the speed of the sensor. The study focused on the settling time of transient piezoresistive events in the material for varying strain step inputs. With known PNEC material settling times, a filter could be applied to the output of this sensor to get an estimate of the load applied to the material.

To aid future inverse modelling and use of PNECs as pressure sensor it is important to understand each transient states of a load, including the loading phase, steady state, or unloading phase. It was found that on average that unloading events had a higher settling time than loading transients for both CBSR 8 and 9 wt% composites across all strains tested from 5 to 30%. No clear correlation was found between the settling time of the transient strain events and the strain percentage applied to the material. Mean settling times ranging 29 - 36 s and 29 - 41 s have been observed for the CBSR 8 and 9 wt% composites respectively.

A different sensing region material could provide a higher frequency response, such as a carbon nanotube silicone composite which has shown a lower settling time in previous works [191, 192]. Due to the viscoelasticity and elastic rebound in the material the resistance relaxation from predecessing load applications was often be present in subsequent load events, altering the observed resistance relaxation response. Future algorithms developed would aim to eliminate these predecessing residual relaxations.

Often soft materials are inherently viscoelastic like much soft tissue within the human body [40], so if soft sensor domains are required with a high frequency response this viscoelasticity will need to be compensated for using this work's performance metrics as a foundation.

It is important to note that if the homogeneity in the material is highly irregular, regions of the material will have different degrees of piezoresistivity the frequency response of the material is likely to vary considerably. Further research is required into how the different CB wt % values effect the temporal response of the material.

4.4.3.3 Localised Force Sensing Performance

The sensor platform gave stress estimates that correlated well with the real stress applied to the material, as seen in Figures 4.13 and 4.14. These stress estimates were gathered from the steady-state data gathered from the EIT measurements at approximately 1.5x the settling times found in Section 4.3.3.1 using the algorithm given in Section 4.3.3.2 to ensure the data was at steady state.

Stress relaxation of the composite CBSR material as a whole gives a good indication of macro-mechanical behaviour of the CBSR. It was postulated that the resistance relaxation gives an enhanced insight into the micro(and nano)-structural behaviour of the CBSR composite, because of the different observed behaviours of the CBSR stress and resistive relaxation and also how these relate to different CB weight percentages and their dispersion.

4.4.4 Real World Applications, Manufacturability, and Scalability

Using EIT-based pressure mapping on a larger scale is feasibly as shown by the use of ERT in geophysics [193]. Potential larger-scale applications include adding a pressure mapping layer under a tennis court to map force exerted by athletes onto a court or a method of measuring foot traffic in buildings and urban areas. The use of the performance metrics discussed in this work would be applicable for both scenarios.

For the tennis court application, the importance of player location and speed may be more important than detecting the footprint shape and exact force applied to the court surface. This means that the E_{CoM} and decay time values would be more heavily weighted than the *SD* and force values, and hence could be tuned for these characteristics. For the urban floor mat application, the importance of footprint shape and force estimation may give useful insight into the physical demographic of people or animals walking across the mat [194]. This may mean that the *SD* and force resolution values are more highly weighted in the design and process.

Larger-scale applications of an EIT-based sensor come with challenges such as, scaling the electronics driving the EIT measurement, fabricating such a large homogeneously piezoresistive domain, and ensuring the reliability in a range of outdoor environmental conditions. Smaller-scale applications are limited by the conductive particle size in the

PNEC. A sensing domain thickness sufficiently larger than the average agglomerate size would be required for reliable EIT mapping and force estimates.

Various forms of tribological wear on the device sensing region would alter the piezoresisitive characteristic of the device. Encapsulation of the device could be implemented to minimise wear and increase hermeticity.

The most obvious limitation of this sensor is the frequency response of the material as shown in Figures **??** - **??**, which could be algorithmically filtered or inverse-modeled to be corrected. Else, other more responsive, less viscoelastic materials could be used, and/or a capacitive EIT-based pressure mapping device used to improve the frequency response of this device. Otherwise the use of a time series dependent neural network, such as an LTSM, RNN, could be used to inversely model such events.

Mass production of an EIT-based sensor would use the performance metrics given in this work to calibrate and quality-check the sensing domain and boundary electrode connections. This work also found that using pin boundary electrodes adds to the durability and stability of electrical connection in this device.

4.5 CONCLUSIONS

An EIT-based piezoresistive sensor using a custom made carbon black silicone rubber composite material has been developed for sensing compressive pressure events and applying performance metrics to obtain the validity of the output EIT images. To be able to apply this EIT-based PNEC pressure sensor to a variety of scenarios, replacing human-like touch, performance metrics has been formed to quantify the sensor's suitability for each application. Sensing domains of 8 and 9 wt% carbon black silicone rubber have been tested using: 6 strain values, 9 load locations, and 3 trials. From this raw data we have calculated data for: spatial resolution, transient settling time, and force sensor resolution.

It was shown that the CBSR 8 wt% sample out performed the CBSR 8wt% sample in terms of spatial and temporal metrics across a range of experiments. The best performance metrics observed in the CBSR 8 wt% sample for E_{CoM}, A_{OL}, and SD, were 0.67 $\pm$ 0.41 mm, 87.93 $\pm$ 2.68%, and 0.12 $\pm$ 0.01 mm^2 respectively for three different load locations. For the sensor domains tested, average settling times of between 19.0 - 44.5 s and 22.5 - 36.0 s were determined for 8 and 9 wt% CBSR samples. A quasi-static conductance-force model of the material was developed with an accuracy of $\pm$ 0.78 and $\pm$ 0.81 N for a range of strains from a centre load test for 8 and 9 wt% CBSR respectively.

Using these performance metric data in future work a piezoresistively inhomogeneous sensor domain could be, calibrated to homogenise the apparent domain piezoresistivity, compensated for transient phenomena, and sense loads with a known degree of accuracy. All of these factors contribute to optimising the EIT-based 2D pressure mapping sensor for different applications. Future work also includes the development of a low-cost, small circuit to capture the the data discretely to open up a larger range of applications. The work shows promise for future use of an EIT-based sensor in a variety of applications requiring a soft sensing domain and non-invasive rigid electrodes.

Chapter 5

Giving Artificial Muscles the Sense of Touch

The content from this chapter is contains content from the manuscript published in the proceedings of Electroactive Polymers Actuators and Devices XXVI.

ABSTRACT

Dielectric elastomer actuators (DEAs) commonly use flexible conductive electrodes to apply an electric potential to actuate. Depending on the material used, these electrodes often possess predictable piezo-resistive properties. Combining electrical impedance tomography (EIT) with a dielectric elastomer actuator (DEA) is investigated in this work to map compressive forces occurring throughout the electrode surfaces. This technology could allow for enhanced closed-loop control of electro-active actuators, broadening their already extensive set of applications. This deformation mapping system also has potential to be used with other piezoresistive materials opening up applications requiring a range of hardnesses and pressure sensitivity. With the material used in this work, the DEA-EIT device has an inherent trade-off between actuation and pressure mapping accuracy driven by the compliant electrode thickness of the DEA. It has been shown experimentally that the simultaneous actuation and EIT mapping can be achieved on the designed hybrid DEA-EIT device. The DEA-EIT device exhibited actuation strains of 2.5 % with a mean center-of-mass detection error of 1.66 ± 0.17 mm for 2 mm thick DEA electrodes. Future designs will ensure that applications requiring human-like manipulation can be designed, ranging between biomedical implant devices, agricultural processing equipment, soft optics, and bio-mimicked robotic aquatic life.

5.1 INTRODUCTION

Fine motor manipulation, pressure sensitivity, and pressure mapping are some core attributes of skin and muscle tissues when innervated to the brain. These functions can be emulated and combined with two core technologies; Dielectric Elastomer Actuators (DEAs), and Electrical Impedance Tomography (EIT) based pressure mapping.

DEAs have been used to mimic biological muscles in many applications, because of the technology's likeness to biological muscle in terms of elasticity, energy density, and various potential shapes/topologies [195–197] . In previous research, it was determined that pressure mapping similar to that of human mechanoreceptors could be emulated using EIT with a piezoresistive nanoparticle elastomer composite (PNEC) in a planar sheet format[20] . The key qualities of the EIT-based sensing platform were that; pressure estimates could be obtained, and the pressure could be mapped and the spatial performance quantified[21] . Like DEAs, this sensing technology has a likeness to human tissue in terms of mechanical characteristics such as elasticity, and the potential of various topologies.

Alongside the visual and other sensory feedback, animals receive when actuating muscle tissue, pressure-sensitive mechanoreceptors are present within the muscle tissue and soft skin tissue to aid control the extent of a muscle contraction. This forms a multi-sensor closed-loop control system with a complex biological control regime. This work is looking towards creating a closed-loop control system which utilises a DEA-based artificial muscle and an EIT-based artificial skin all contained within monolithic bodies. Applications such as the ones conceptualised in Figure 5.1 can be designed with the use of DEA-EIT integrated technology.

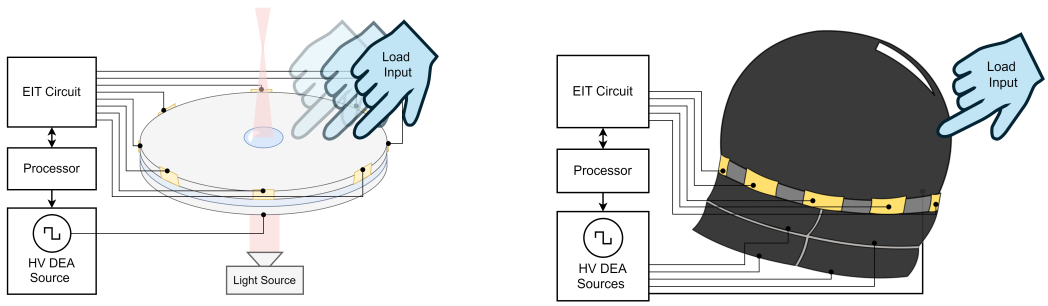

FIGURE 5.1: Potential future application of the DEA-EIT device topology. Left: EIT sensor input DEA controlled optical lens. Right: Pressure mapping sensitive skin for a DEA propelled jellyfish soft robot.

5.1.1 Background

The fundamental principles and a brief explanation of the state-of-the-art of each DEA and EIT-based sensor technologies are given in this section. A review of pressure mapping devices with actuation capabilities was then completed. At the time of completing this work, no literature had been found regarding the combination of these two technologies using PNEC electrodes on a DEA for simultaneous execution of sensing and actuation events.

5.1.1.1 Dielectric Elastomer Actuators

DEAs are often referred to as artificial muscles because they share similar characteristics to biological muscle. Although commonly used as an actuator, this technology offers versatile applications as an energy generator[198–200] or sensor and provides attractive features such as high energy density, large displacements, and fast response times. DEAs have been proven to produce strains larger than 1600 %[82] which is significantly larger than that of regular biological muscle. However, large DEA strains can often be at the cost of actuator instability and a low effective force. DEAs have a high work and power density comparable to that of biological muscle and have been found experimentally to have energy densities of around 3.4 $J.g^{-1}$ and theoretically an order of magnitude more[136, 200] . A dielectric elastomer actuator (DEA) is a form of soft robotic actuator that induces deformation with an applied electric field. A simple common configuration of DEA is a circular parallel plate capacitor, which consists of a thin elastomer sheet between two compliant conductive electrodes, as shown in Figure 5.2.

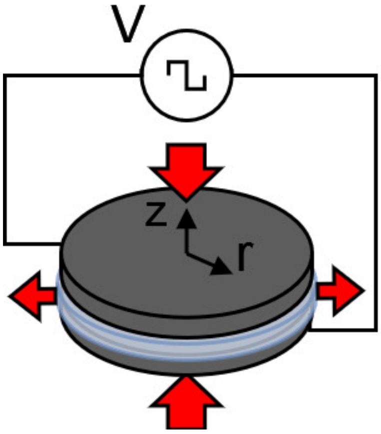

FIGURE 5.2: A circular DEA exemplifying its actuation principle.

When a voltage is applied to the compliant electrodes, an electrostatic force arises between the electrodes causing the dielectric elastomer (DE) membrane to contract by a decrease in thickness and an increase in area. The resulting actuation is controlled by changing the applied voltage. The region encompassing the two compliant electrodes and the DE portion sandwiched between them is called the 'active region', i.e. where the electric field is largest. For a simple DEA such as the one shown in Figure 5.2, a simplified formula for the electrostatic force on the compliant capacitor electrodes is given in Equation 5.1.

$$\sigma_{es} = \varepsilon_0 \varepsilon_r \frac{V^2}{z_{de}^2} \tag{5.1}$$

Where σ_{es} is the electrostatic stress, V is the applied voltage, z_{de} is the DE thickness, ε_0 is the permittivity of free space, and ε_r is the relative permittivity constant of the DE, which is a function of strain[201–203] and applied voltage[36] . This can be expanded to estimate the DE strain, $S_{z_{de}}$, using the bulk modulus, K, of the DE as shown in Equation 5.2.

$$S_{z_{de}} = \frac{\sigma_{es}}{K} \tag{5.2}$$

Designing a DEA for practical applications is often highly constrained by three key modes of failure as well as the parameters of the constituent components. A common mode of failure is the electromechanical instability of the elastomer. With increasing voltage, the DE compresses until the voltage exceeds the critical point at which dielectric breakdown occurs. At the point of failure, the DE membrane experiences a surge of electrical current, permanently changing the DE insulative properties. The second mode is a loss of tension in the elastomer when an applied voltage is large and the axial force provides an excessively large compression. The stress in the DE may cause the plane to lose tension such that the elastomer no longer actuates as expected, if at all. Often resulting in visible wrinkles in the DE. The third mode is a physical rupture of the elastomer due to stretching beyond the DE's yield strength [204] . A key benefit of DEA technology is its potential to be fabricated into various topologies depending of the desired application including, parallel plate[82], roll[205], tube[206], helical[134], and conical geometries[207] .

5.1.1.2 Soft EIT-based Pressure Mapping

A soft EIT-based pressure mapping sensor has the ability to estimate the magnitude and location of deformation events in a planar PNEC material. The hardware required usually consists of a piezoresistive sensor domain with attached boundary electrodes, EIT driver electronics, and a reconstruction processor. Boundary electrodes allow a non-invasive method of pressure mapping without compromising a monolithic piezoresistive material. Several researchers have created an EIT-based pressure mapping sensor using a range of piezoresistive domains and custom or lab-based hardware [21, 105, 160, 180–182] .

Electrical impedance tomography or EIT is most commonly used in medical pulmonary research to give a cross-section of a human thorax in real-time at a frame rate of 50 Hz, as shown in the two commercially available medical EIT machines the Pulmovista500 (Draeger, Lübeck, Germany) and the LuMon System (Sentec, Lincoln, USA). However, using EIT to map and quantify pressure events has the potential to give a faster frame rate due to the use of DC instead of AC. However, the viscoelastic and resistive nature of the sensor can lower the frequency response of the sensor depending on the piezoresistive sensing domain used. The stages required to generate a pressure image using EIT can be simplified into three core stages,

1. Data acquisition
2. Image reconstruction
3. Inverse force model

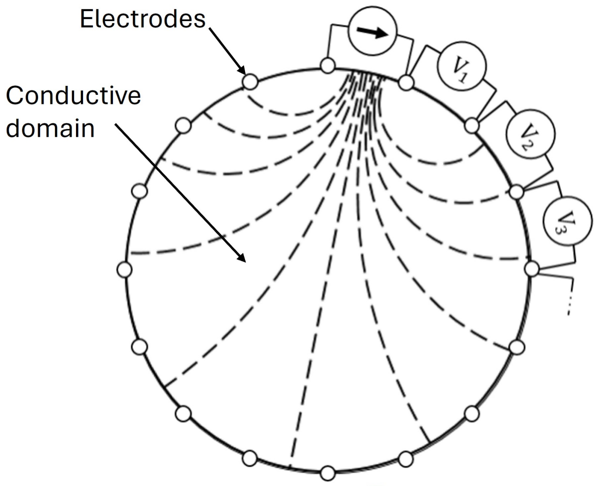

FIGURE 5.3: A 16 electrode circular EIT domain setup exemplifying its electrical function. Where the dashed lines are representative of an applied electric field[20] .

Data acquisition involves an excitation drive pattern to be applied to the piezoresistive sensing domain, which consists of the injection of a known current or voltage through two boundary electrodes connected to the material domain as shown in Figure 5.3. Typically an adjacent electrode drive pattern is used in literature and is also used in this work[181] . Concurrently all voltages at the other boundary electrodes of the material domain are read. Then a known current (or voltage) source is applied to the next set of adjacent electrodes, and all of the other adjacent electrode voltages are read once more. This process is repeated until it has been deemed there have been sufficient readings to solve the inverse problem and generate a conductance, ρ, distribution estimate of the material domain. Finally, an inverse model converting the conductance estimate of the material domain can be converted into a pressure map using an inverse model.

5.1.2 Simultaneous Pressure Mapping and Actuation

Various researchers have demonstrated and proposed the use of self-sensing DEAs for closed-loop control looking at the one-dimensional deformation of a DEA using their change in capacitance[35, 37, 38, 208] . Multi-degree-of-freedom (multi-DOF) DEA topologies have been created by several researchers [209–212] , allowing for a broader range of applications. The complex actuation mechanisms discussed in these papers give rise to the question of having more resolute sensor data for such topologies to aid with the control of such multi-DOF devices.

To sense deformation in multiple dimensions, the current methods used for DEA self-sensing must be altered. To ensure the DEA maintains minimal change to the parallel plate topology, the compliant piezoresistive electrodes can be used and/or altered to be able to determine the deformation of the DEA in more than one dimension. Options for sensing in two dimensions include determining the stretch across the compliant electrode material by measuring the change in resistance of the electrodes diametrically opposed at various angles around the DEA, or adding an extra pressure mapping sensor layer to the DEA stack, or using EIT to map change in resistance of the compliant electrodes. Using diametrically opposed resistance measurements across the compliant electrodes will have limited resolution and is limited in compliant electrode shapes that can be used effectively. Adding another sensing layer to the DEA requires a sensing technology that has a very low elastic modulus, to not hinder the actuation force of the DEA. The limitations given above are why EIT was chosen to sense 2D deformation of a DEA, as it has a relatively high spatial resolution that can be quantified and requires no extra hardware on the DEA body apart from non-invasive electrodes on the boundary of the DEA's compliant electrode(s).

5.2 METHODOLOGY

The DEA-EIT actuator-sensor-hybrid system required the two technologies to be verified and fabricated individually before being integrated to observe the effects of combining the two technologies relative to their independent forms. The following sections discuss the fabrication process for the DEA and EIT systems and then the integration of them both into a DEA-EIT device.

To optimise the actuation and sensing capabilities of the DEA-EIT system different parameters of the design were altered, such as the compliant electrode composite used, DE material used, circumferential electrodes, and magnitude of DE pre-stretch and sizing. The methodology explores the reasoning to certain design choices for the fabrication of the DEA design seen in Figure 5.4.

5.2.1 Dielectric Elastomer Preparation

The fabrication of the DEA used a rigid acrylic frame to attach the pre-stretched elastomer. For simplicity, a circular frame was chosen with the DE at a radial pre-stretch of +10%, i.e. $\lambda_r = 1.1$, as this is well within the DE's more predictable linear elastic region. The circular acrylic frame of 178 mm inner diameter was fabricated from laser cut acrylic of 4 mm thickness to ensure rigidity.

To achieve uniform stretch of the elastomer sheet, a toroidal shower hose mechanism was placed on the relaxed sheet of 4910 VHB tape (3M, Saint Paul, USA), which would act as a pre-stretcher annulus. The toroidal mechanism has an axis of rotation along its circumference as shown in, giving the ability to roll and stretch the elastomer equiaxially to the desired pre-stretch.

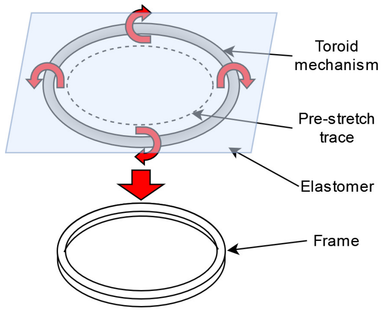

((A)) Elastomer pre-stretch method

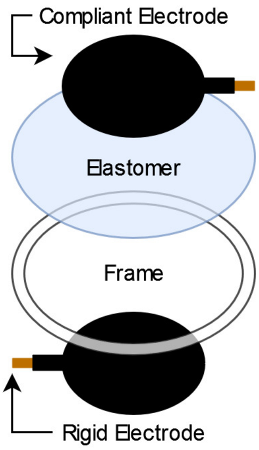

((B)) Circular DEA construction

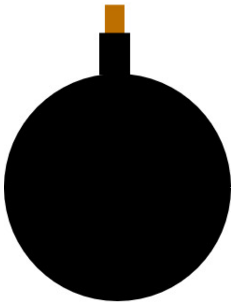

((C)) Single circumferential electrode

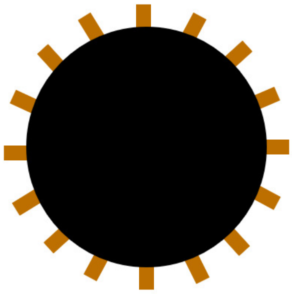

((D)) Multiple circumferential electrodes

FIGURE 5.4: Mechanical fabrication of the circular DEA-EIT platforms

5.2.2 Compliant Electrode Fabrication

Compliant electrodes (or active area) were fabricated using acrylic moulds of varying dimensions. Three thicknesses, z_{ce}, of the compliant electrode were fabricated, 0.5 mm, 1 mm and 2 mm, with two circular compliant electrodes of 100 mm diameter. Different thicknesses were explored as this would vary the actuation and sensing performance of the electrodes.

Two compliant electrode mediums were used in this work, carbon black (CB) powder and a carbon black silicone rubber (CBSR) composite. Compliant electrodes solely made of CB powder have been used for DEAs in previous literature[213–215] , hence this work uses the same compliant electrode type to generate reference data. The CB powder was used to make a single circumferential electrode configuration DEA as a reference to compare to the following DEA-EIT experiments. The CBSR composite was used to make both single (Figure 5.4(b)) and multiple (Figure 5.4(d)) circumferential electrode configurations of DEAs. The CB powder used in all of the compliant electrode samples was Vulcan XC-72 powder (Fuel Cell Store, Bryan, USA). The CBSR composite had 8% CB by weight mixed with DragonSkin 10NV silicone rubber (Smooth-On, Macungie, USA). This composite is a piezoresistive medium that has proven useful for EIT pressure mapping and sensing in previous work[21] , and DEA actuation[213, 214] .

Using the liquid silicone rubber, the CBSR composite mixture was formed by combining part A of the silicone solution and 8 wt% CB and mixing by hand for 10 s. The mixture was then placed in the ARV-310PCE planetary vacuum mixer (Thinky Inc., Tokyo, Japan) to complete a mixing cycle with 500 RPM for 45 s followed by a cycle with 800 RPM for 45 s. In the same mixing container, part B of the silicone solution was added to the mixture and stirred by hand for 10 s and immediately the same mixing cycle in the planetary mixer was completed again. After the cycle was completed, the composite was poured into the mould with attached circumferential copper tape electrodes. The CBSR mixture was then placed in an oven at 80 °C for 4.5 h to ensure the composite was sufficiently cross-linked.

Two types of compliant electrode configuration have been fabricated in this work, single circumferential electrode and multiple circumferential electrodes. The single circumferential electrode configuration was purely for testing DEA actuation. The multiple circumferential electrode configuration consisted of 16 evenly spaced circumferential electrodes. The multiple circumferential electrode configuration was for testing both EIT-based pressure mapping and actuation functionality of the DEA. Prior to curing the compliant electrode in a circular mold, the conductive copper tape circumferential electrodes were placed into the mold. The width of the circumferential electrodes were 8 mm. The circumferential electrodes were placed with a 3 x 8 mm area embedded in the compliant electrode circumference edge with the rest of the circumferential electrode protruding for easy access to external electrical connections.

5.2.3 DEA Hardware

The excitation voltage for the DEA was provided by a Trek 610E high voltage supply (Advanced Energy Industries, Fort Collins, USA) providing a maximum voltage output of 10 kV DC. The DEA was placed in a clear insulated box with the high voltage supply leads attached to the rigid copper electrodes of the DEA. An iPhone 11 camera (Apple Inc., Cupertino, USA) was used to obtain images of the radial compliant electrode strain as shown in Figure 5.5. The current limit of the high voltage supply was set to its maximum of 2 mA to ensure the DEA actuation response was not limited by the charging of the compliant electrodes.

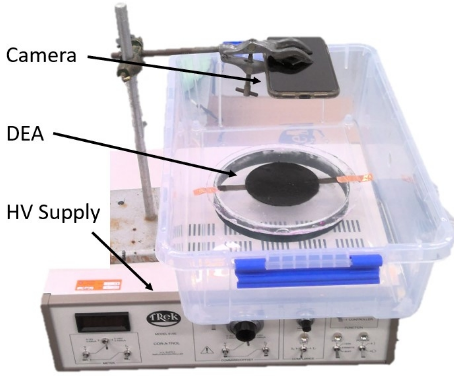

FIGURE 5.5: DEA excitation and measurement setup

5.2.4 EIT Hardware

The EIT hardware allows for data collection to reconstruct a conductance map of the of piezoresistive composite used as compliant electrodes in the DEA samples. The hardware required for this function, shown diagrammatically in Figure 5.6, includes a 2634b source measure unit (SMU) (Keithley, Solon, USA), a custom 4:16 multiplexer (MUX) PCB, an ESP32 development board, a Cartesian force applicator, and a reconstruction and control computer.

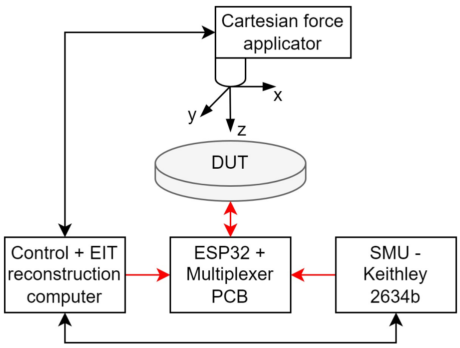

FIGURE 5.6: Architecture of the force applicator and EIT measurement system [21]

The SMU provides a constant current value of 1 mA and reads a series of voltages through the MUX PCB required for the EIT drive pattern. An adjacent electrode EIT drive pattern was used for EIT through the circumferential electrodes of the compliant electrode. The MUX PCB and SMU and controlled by the control computer. Once the data for each image reconstruction has been gathered the control computer was also used for the reconstruction of the conductivity maps of the compliant electrodes. The Cartesian force applicator is made up of a MK3s 3D printer (Prusa, Prague, Czechia) integrated with a loadcell and fabricated applicator tip to apply loads and hence generate data for pressure magnitude and localisation quantification.

5.2.5 Experimental Method

Before attempting to have simultaneous DEA actuation and EIT sensing occur in the same device, each system had to be tested independently. First DEA strain voltage relationships were explored followed by EIT-based pressure mapping of the DEA electrodes. Finally the same samples used for EIT testing were subsequently integrated into a DEA device for simultaneous functional testing.

5.2.5.1 DEA Validation

DEA actuation strain measurements were taken from voltages 5 kV to 10 kV in 1 kV increments. The SNR of strain measurements of the DEA excited with voltages < 5 kV were deemed to be too low to generate meaningful data. The excitation voltage was toggled between on and off states waiting for the strain deflection to reach a steady state for the strain measurements. Five radial strain images were captured and measured. The measurements were then averaged to minimise error and determine the radial strain uniformity. The radial strain was found by measuring the radial change of the circular compliant electrodes between relaxed and electrically contracted states. From the radial compliant electrode strain the planar and thickness deformation of the DE was estimated. The DE is assumed to be incompressible and have a Poisson's ratio, ν, of 0.5. The adhesion between the compliant electrode and the DE is assumed to be perfect to simplify the model used here. The thickness strain, $S_{z_{de}}$, is calculated using Equation 5.3[213] and 5.1.

$$S_{z_{de}} = \frac{1}{(S_{r_{ce}} + 1)^2} - 1 \tag{5.3}$$

Where S_r is the radial strain measured from the equi-biaxial actuation. The elastic modulus of a hyperelastic material such as VHB is often defined as a non-linear function of strain and strain rate[216] . In this work a linear bulk modulus value, K, of 142 kPA was used. The bulk modulus was determined by doing a meta-analysis and averaging of the elastic modulii determined at steady state 10% strain for VHB 4905 material in previous literature[38, 216, 217] . The relative permittivity, ε_r, used in Equation 5.1 was approximated to be 4.5±0.2 due to pre-strain effects seen in literature[201–203, 218] .

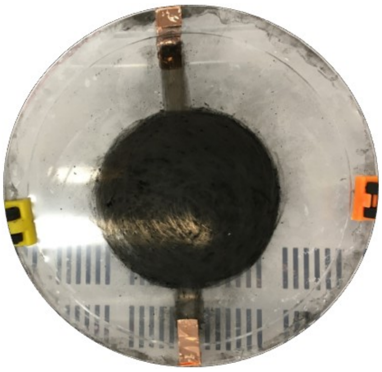

val

((A)) The reference DEA made with CB powder compliant electrodes

((B)) A DEA with 0.5 mm thick compliant electrodes at steady state contraction and excited at 10 kV

FIGURE 5.7: The two DEA compliant electrode material types used in this work.

5.2.5.2 EIT-based Pressure Mapping on DEA

A load sequence was devised to ensure that forces in various locations of the compliant DEA electrode could be localised using EIT. A similar test procedure used in previous works[21**?**] was applied to the three individual compliant electrodes thicknesses, z_{ce}, of 0.5, 1, and 2 mm. Nine load application points were determined on the material at three distinct radii as shown in Figure 5.8.

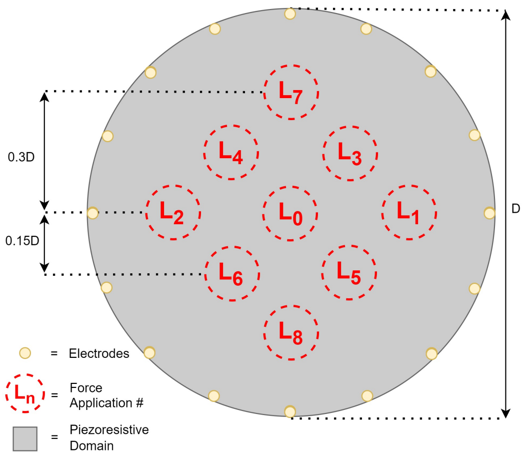

FIGURE 5.8: Load application areas used for compressive stress testing in order of application[21] .

A Cartesian force applicator applied the loads with varying strains in the nine locations. Once the compliant electrodes had undergone the first load application tests, they were applied to each side of a DEA and tested again using the same sequence of nine loads. Compressive strains from 0 to 30% of the electrode thickness in 5% increments were applied when to each of the load points using a flat circular 13 mm diameter force applicator. When applying the compressive strain to the compliant electrodes, a slow strain rate of of 16.67%.s^{-1} was used to minimise piezoresistive transient phenomena. After completing the load tests on individual compliant electrodes the compliant electrodes were attached to the DE surface. Next the load test was completed again to the DEA placed on a flat surface.

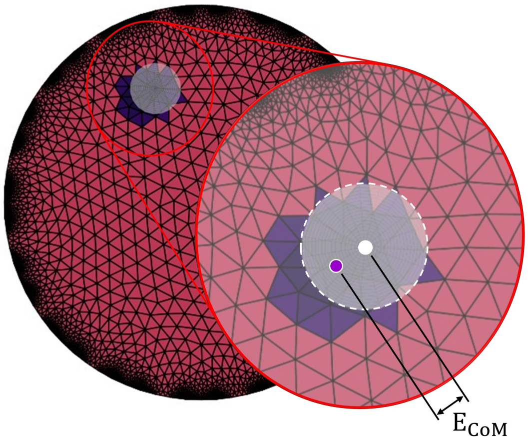

((A)) E_{CoM}

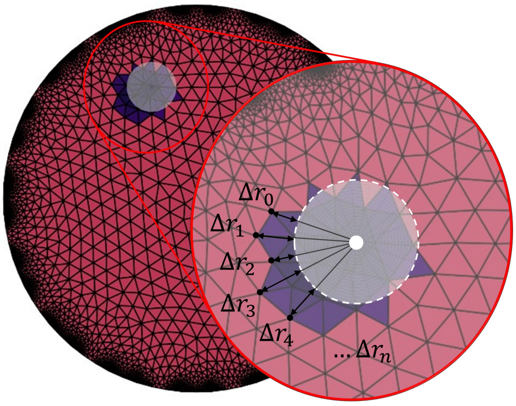

((B)) *SF*

FIGURE 5.9: The two spatial performance metrics used for determining accuracy of blob as a load area estimate, where the transparent white circle is the actual load area and the dark purple elements are the load estimate area.

$$SF = \left(\sum_{n}^{i} \Delta r_i^2 \right) / n \tag{5.4}$$

After gathering all of the experimental data from applied loads, the data was used to generate EIT conductance images. To form blobs as estimates of the applied loads, post-processing was completed by applying an 85 % threshold mask to the EIT image. These blob images were subsequently analysed using two spatial performance metrics, the center-of-mass error, E_{CoM}, and the shape fit, *SF*, as exemplified in Figure 5.9. The E_{CoM} values were determined by calculating the difference between the CoM of the actual load and the blob representing the load estimate. The *SF* was determined by calculating the radial mean square error between all of the, n, perimetral nodes of the blob load estimate and the actual load circumference, as taken from the CoM of the actual load area.

5.2.6 Simultaneous Actuation and Pressure Mapping

The DEA-EIT device was tested for simultaneous actuation and pressure mapping to highlight the functional limitations that arise with such a device. Simultaneous actuation and pressure mapping involves an excitation voltage is applied to the DEA whilst completing EIT to the grounded DEA electrode.

To ensure that the EIT electronics are able to operate during transients or dielectric breakdown events, an intermediary 20 V Zener diode array and a current limiting resistor, R_{lim}, were added to the system as shown in Figure 5.10.

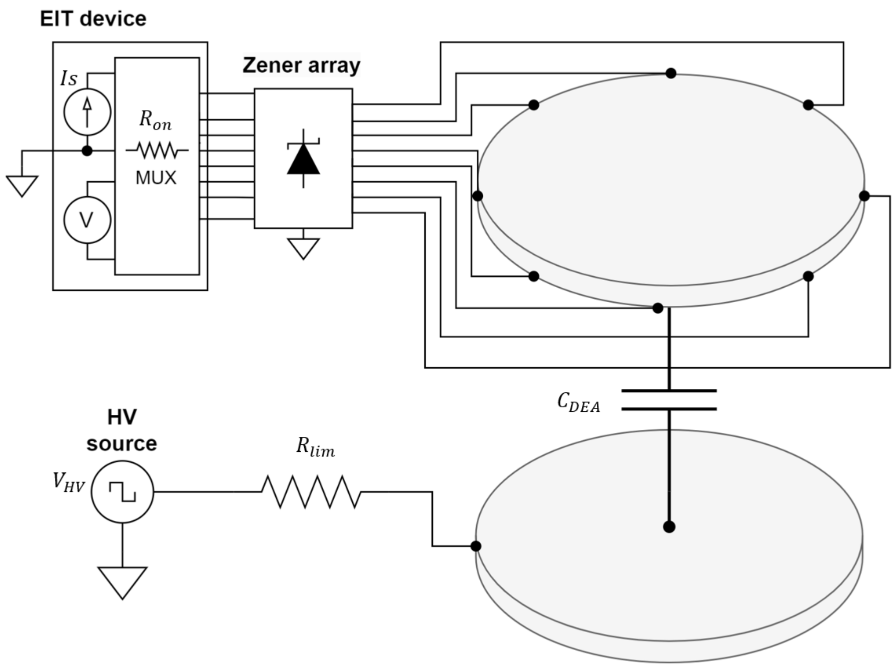

FIGURE 5.10: System architecture for simultaneous DEA actuation and EIT mapping.

When the DEA is switched on, the compliant electrodes charge. During this charging period a voltage will be developed on the HV and low-voltage EIT electrode characterised by the charging capacitance, C_{DEA}, the HV source resistance, R_{lim}, and the multiplexer on resistance, R_{on}. The resistance of the DEA is lumped in with R_{lim} for the Equations 5.5 and 5.6 below. The charging of the DEA capacitance is governed by Equation 5.5.

$$V_{DEA_{HV}}(t) = V_{HV}(1 - e^{-t/(R_{on}+R_{lim})C_{DEA}}) \tag{5.5}$$

In the configuration shown in Figure 5.10, a voltage divider is created between the R_{lim} resistor and the multiplexer, R_{on}, on-resistance to ensure the voltage seen at the multiplexer input pin is sufficiently low. The voltage seen on the multiplexer pin is given by Equation 5.6.

$$V_{\mathrm{MUX}}(t) = V_{HV}\frac{R_{on}}{R_{on}+R_{lim}}e^{-t/(R_{on}+R_{lim})C_{DEA}} \tag{5.6}$$

To mitigate the effects of the DEA switching transients during loading experiments, the loads were applied when the DEA voltages were at steady state, as exemplified in Figure 5.11, to observe the effects of the high voltage electrode on the EIT electrode mapping.

To investigate the effects the DEA voltage switching transient has on EIT data capture, EIT frames were captured during switching events as shown in Figure 5.11.

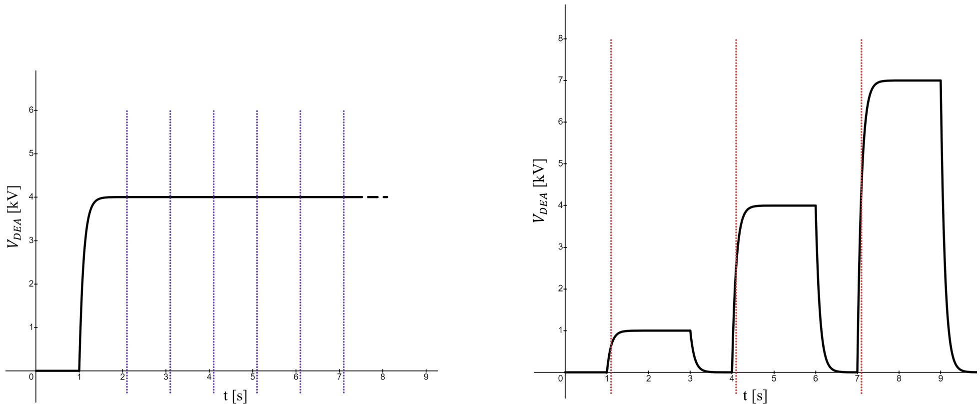

FIGURE 5.11: Illustrative experiment timing diagrams. Left: Steady state V_{DEA} where the purple dotted lines represent the time a load event begins. Right: Transient EIT measurements where the red dotted line represents the time an EIT frame capture begins.

5.3 RESULTS

First the measurements taken during fabrication are explored, followed by the results from the independent DEA actuation validation and EIT pressure mapping validation. Finally, results are presented on the phenomena of concern when integrating HV DEAs with EIT-based pressure mapping.

5.3.1 Fabrication

Prior to constructing the DEA, the compliant CBSR inter-electrode resistances, R_{int}, were measured in a similar fashion to voltage shown in Figure 5.3 to ensure the sufficient conductivity and hence CB particle dispersion for DEA actuation and EIT-based sensing. R_{int} between the adjacent circumferential electrodes for all samples was consistently < 20 kΩ, as shown in Table 5.2. Therefore, the R_{int} values indicated a sufficiently low resistance for the EIT circuitry and indicates sufficiently homogeneous CB particle dispersion.

5.3.2 DEA Validation

Before testing the piezoresistive compliant electrodes for both actuation and pressure mapping capability, the reference DEA was tested for its voltage actuation strain relationship. The theoretical actuation strain versus voltage was compared to the measured strain for the reference DEA shown in Figure 5.7(a). The actuation strain data gathered is shown in Figure 5.12. The range given was derived from substituting the range of K and ε_r parameter values found in previous similar works[38, 216, 217] into Equations 5.1 - 5.3.

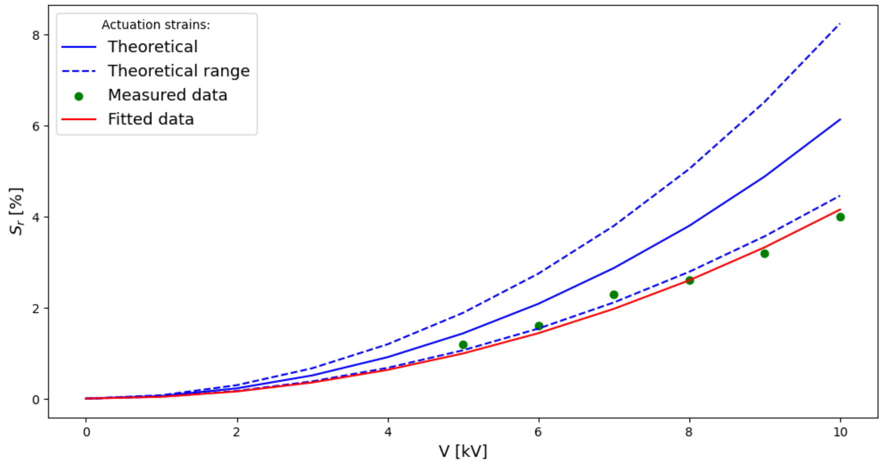

FIGURE 5.12: Comparing the measured CB reference DEA strain, the theoretical strain average and range, and the data fitted to Equation 5.3 by fitting either parameter K or ε_r.

The curve fit shown in Figure 5.12 was found to have a linear set of solutions for K and ε_r with values similar to those limits of the material given characterisation determined in previous literature [219] .

The CBSR compliant electrode experiments showed significantly smaller strains relative to the DEA with the CB powder compliant electrode as displayed in Figure 5.13. The effective mechanical impedance for the DEA with the CBSR compliant electrodes was significantly increased due to the relative thickness of the CBSR electrode and similar bulk modulus relative to the DE VHB material. Hence an effective bulk modulus, K_{eff}, was calculated from fitting to the measured data, as a sum of the existing DE bulk modulus, K, and the effect of the compliant electrode's bulk modulus. K_{eff} is the a key characteristic of using thick compliant electrodes on a DEA that limits the actuation performance. When calculating K_{eff}, ε_r is assumed constant, as the effects of this different compliant electrode thickness on ε_r is assumed relatively negligible.

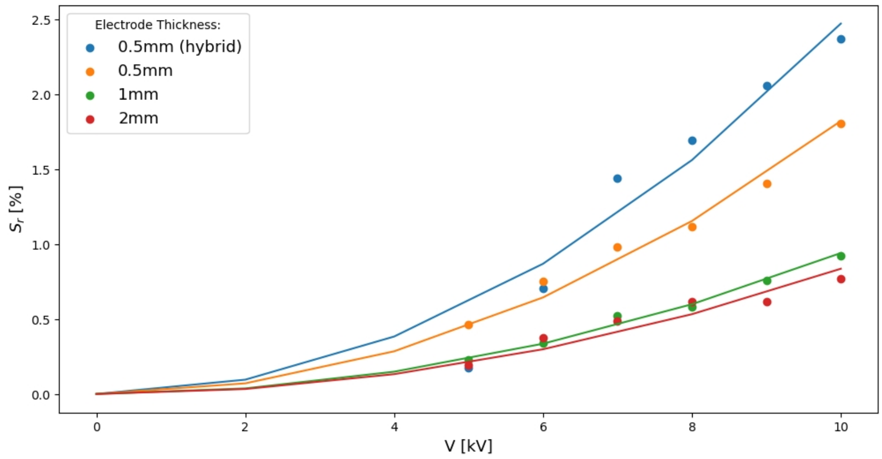

FIGURE 5.13: Comparison of the voltage strain relationships between the 100 mm diameter compliant electrodes of various thicknesses, z_{ce}, used for the DEA.

The effective bulk modulus impeding the actuation of the DE was calculated for each CBSR compliant electrode thickness by fitting to Equation 5.3 with the results displayed in Table 5.1. To further enhance the actuation strain, $S_{z_{de}}$ of the DEA-EIT device, the compliant electrodes were hybridised such that one of the compliant electrodes was made from CB powder and the other from the CBSR composite. The hybridised results for the K_{eff} value are also given in Table 5.1.

TABLE 5.1: Effective bulk modulus, K_{eff}, and coefficient of determination, R^2, for each fit of voltage-strain data for the CBSR compliant electrodes.

z_{ce} [mm]	K_{eff} [kPa]	R^2
2	966	0.86
1	860	0.99
0.5	450	0.98
0.5 (hybrid)	334	0.91

5.3.3 EIT Validation

Validation of the EIT sensing method on the compliant electrodes was carried out for the three different electrode thickness, z_{ce}, values to see the differences the thickness may have on the pressure mapping characteristics' spatial performance. Figure 5.14 exemplifies the difference in the conductance reconstructions for a load.

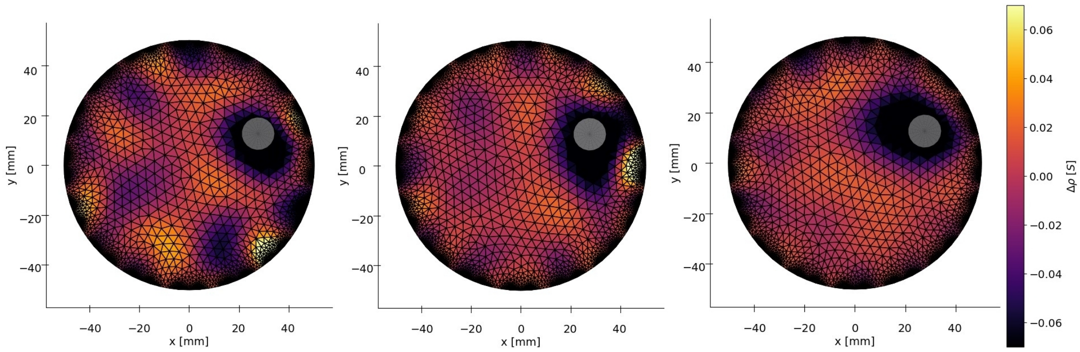

((A)) $z_{ce} = 0.5$ mm ((B)) $z_{ce} = 1$ mm ((C)) $z_{ce} = 2$ mm ((D)) Scale

FIGURE 5.14: A 15% strain compression at point L_1 applied to 100mm diameter compliant DEA electrodes of 3 compliant electrode thicknesses.

A significant factor for determining the minimum pressure able to be detected is governed by the noise floor experienced when the domain is in a steady relaxed state. A metric used to quantify the noise floor is the noise figure, *NF*, which is commonly used in other applications of EIT[21, 168] . To quantify the domain homogeneity the inter-electrode resistance (i.e. between adjacent electrodes) and respective standard deviation data for each sample was gathered alongside the NF, as shown in Table 5.2.

TABLE 5.2: Noise factor and mean inter-electrode resistance, $\bar{R}_{int}$, for each thickness of compliant DEA electrode used for EIT

z_{ce} [mm]	*NF*	$\bar{R}_{int}$ [kΩ]
2	0.99	4.40 ± 0.69
1	0.98	7.72 ± 1.14
0.5	0.96	9.91 ± 2.16

To quantify the localisation performance of the loads applied to the DEA compliant electrode the center-of-mass error, E_{CoM}, and shape fit, *SF*, of the sensing system were calculated. A polar histogram plot of the E_{CoM} values from each frame from an experiment are displayed in Figures 5.15(a) - 5.15(b). From this same experiment a mean E_{CoM} is given in Table 5.3.

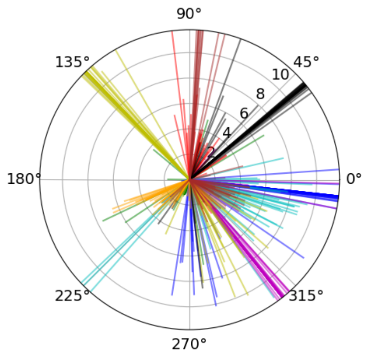

((A)) $z_{ce} = 0.5$ mm

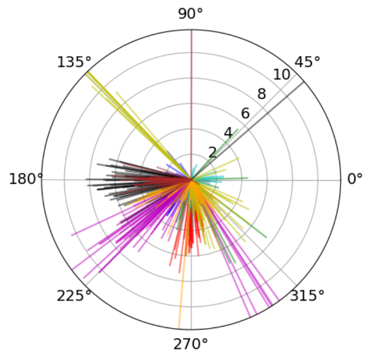

((B)) $z_{ce} = 1$ mm

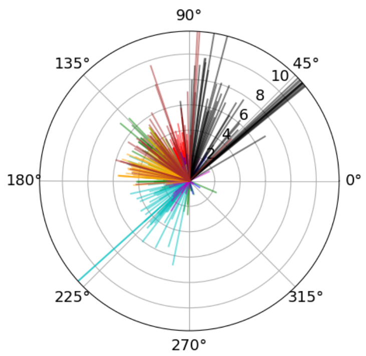

((C)) $z_{ce} = 2$ mm

((D)) Load locs

FIGURE 5.15: Vectorised E_{CoM} for the nine load experiment at 20% compressive strain for each z_{ce} value tested on individual DEA-EIT compliant electrode samples.

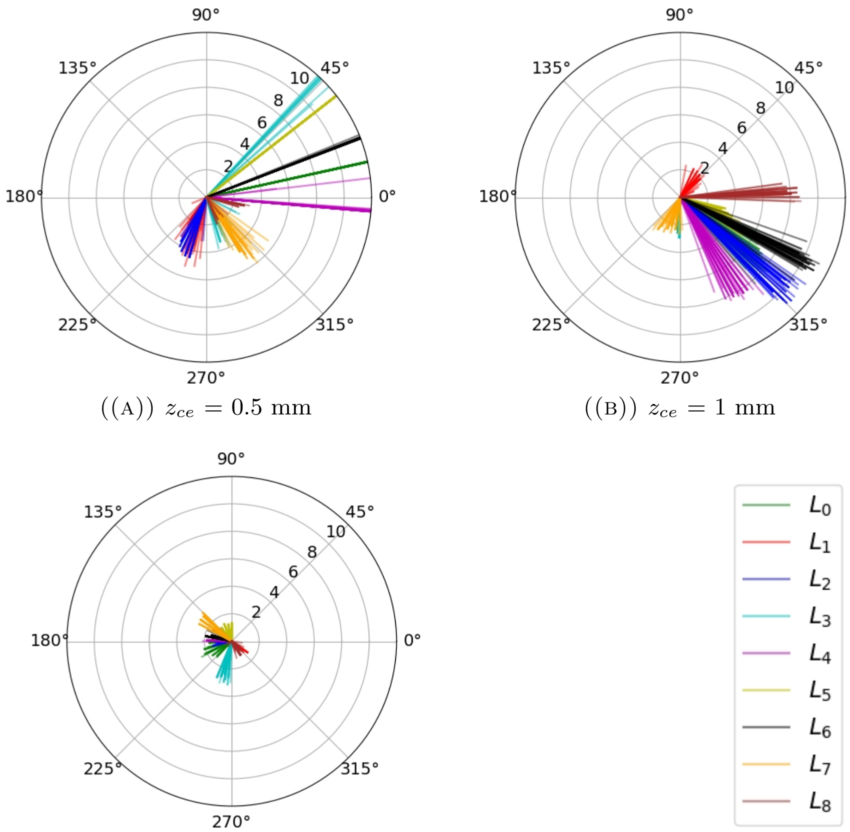

((A)) $z_{ce} = 0.5$ mm

((B)) $z_{ce} = 1$ mm

((C)) $z_{ce} = 2$ mm

((D)) Load locs

FIGURE 5.16: Vectorised E_{CoM} for the nine load experiment using the same indentation depth as Figure 5.15 for each z_{ce} value tested on the DEA-EIT integrated samples.

Mean values for the spatial performance metrics, E_{CoM} and SF, were gathered for each strain, each thickness, and at each load point. Spatial performance metric means from two nine load experiment are given in Tables 5.3 and 5.4. The SF values are found using Equation 5.4.

TABLE 5.3: Mean E_{CoM} and SF values ($\pm$ std) obtained for each DEA compliant electrode thickness at 20% strains loads

z_{ce} [mm]	$\bar{E}_{CoM}$ [mm]	$\bar{SF}$ [mm^2]
2	4.10 ± 1.93	46.03 ± 0.51
1	4.25 ± 2.42	36.93 ± 0.92
0.5	10.43 ± 6.06	81.92 ± 8.43

Table 5.4: Mean E_{CoM} and SF values ($\pm$ std) obtained for each DEA stack at the same indent depth as 20% strain in Table 5.3 loads. *Where the compliant electrode is part of a DE compliant electrode DEA stack.

z_{ce}* [mm]	$\bar{E}_{CoM}$ [mm]	$\bar{SF}$ [mm^2]
2	1.66 $\pm$ 0.17	46.03 $\pm$ 0.56
1	6.01 $\pm$ 0.44	37.03 $\pm$ 1.06
0.5	8.83 $\pm$ 1.49	81.64 $\pm$ 7.99

5.3.4 Simultaneous Actuation and Pressure Mapping

Simultaneous actuation and pressure mapping has been performed when at a range of actuation strains using excitation voltages ranging from 1 kV to 10 kV. Each DEA voltage excitation yielded similar noise in their reconstruction results as shown in Figure 5.17.

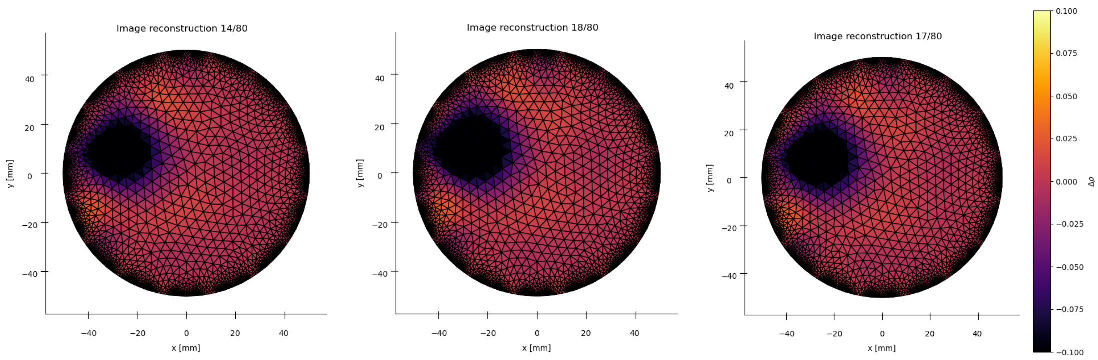

((A)) $V_{\mathrm{DEA}} = 1kV$ ((B)) $V_{\mathrm{DEA}} = 4kV$ ((C)) $V_{\mathrm{DEA}} = 7kV$

Figure 5.17: Loads applied to the compliant ground electrode of a DEA during different steady state voltage excitations, V_{DEA}.

The next set of experiments observed the transient effects of a high voltage step input the DEA during an EIT cycle. Artifacts such as the ones given in Figure 5.18 occur due the inrush/outrush currents across the DEA's capacitance.

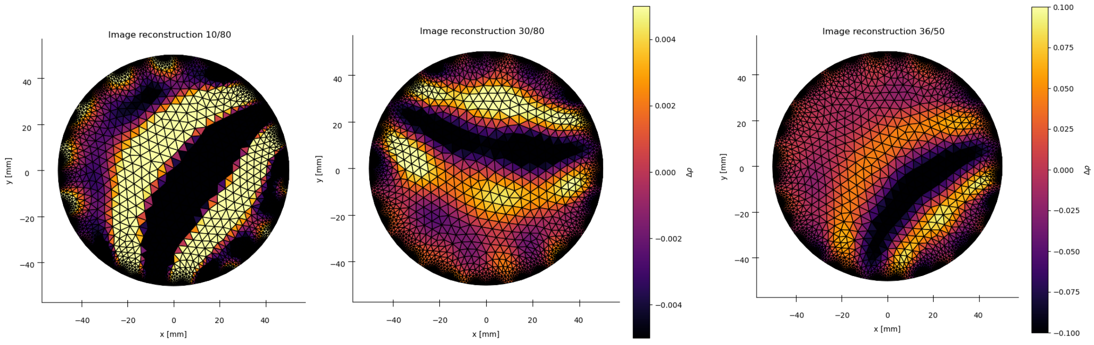

((A)) $V_{DEA} = 1$ kV ((B)) $V_{DEA} = 4$ kV ((C)) $V_{DEA} = 10$ kV

FIGURE 5.18: An unloaded DEA with a captured during various voltage, V_{DEA}, step input artifacts.

Note that the scale on Figure 5.18 contains two scales and one is an order of magnitude smaller than that seen in Figure 5.17 to highlight and investigate the transient artifact pattern observed.

5.4 DISCUSSION

A system was created that could both generate strain and map strain events using common DEA componentry with a circular DEA topology. The major limitations of integrating the two technologies were explored and quantified as a starting point for the further optimisation of such a device.

5.4.1 Fabrication

Fabrication methods were successfully developed to create a range compliant electrode composites for successful DEA actuation and EIT-based pressure mapping. The fabrication process had limited quantification of the dispersion of CB particles within the CBSR composite material used for the DEA compliant electrodes. A basic check for homogeneity was done using the device hardware measuring the inter-electrode resistance between adjacent electrodes as shown in Table 5.2. Further validation to check the homogeneity of the whole domain could be done using other invasive or non-invasive methods such as a nail-bed resistance test and/or spectroscopic imaging. Inhomogeneity quantification on a resolution similar to that of the thickness of the material sample is important to obtain a higher SNR and hence *NF* value. Dispersion of the CB particles and minimisation of air voids was ensured by using a vacuum planetary mixer, however a change to a less viscous liquid silicone rubber in future could ensure improved mixing, less air voids, and increased homogeneity.

A key limitation to decreasing the thickness of the compliant electrode occurs at a point where the tear strength of the material is significantly lower than the elastic modulus of the circumferential electrodes, hence increasing the likelihood of mechanical failure through tearing resulting in unstable conductivity or an open-circuit of the electrical connection.

Moulds were used successfully to generate a series of samples, in future work other techniques for film fabrication could be used to improve sample quality such as, screen printing, spin coating, and conductive coating deposition and spray methods [213, 220, 221] .

Stress-strain characterisation of DEs in literature clearly shows a hyperelastic softening effect between 50 to 400 % strain for VHB film material whereby the elastic modulus decreases to 40 - 70 kPa[216] . This is significantly less than the assumed $\sim$ 142 kPa elastic modulus resulting from a 10 % pre-stretch in this work. This hyperelastic region should be determined using both the DE and compliant electrode materials' hyperelastic regions to ensure the K_{eff} is minimised for maximal actuation strain, $S_{z_{de}}$.

5.4.2 DEA Validation

Through actuation testing of different compliant electrodes applied to a DEA, models were fitted to the voltage-strain data gathered with R^2 values between 0.86 and 0.99. The model fitting resulted in the formation of effective bulk modulus, K_{eff}, values of the DEA active region ranging from 334 to 966 kPa for increasing $z_c e$ values. The use of an effective bulk modulus constant only holds for a small linear range of strains. The CBSR compliant electrodes should be modelled to produce expected behaviours for a much larger range of strains to optimise for a better DEA-EIT system over a large range of potential pre-stretches and actuation strains.

Mullins effect was expected to be observed in our experiments with CBSR compliant due to the nature of testing conductive particle filled elastomer composites[222]. Mullins effect is the change in the stress-strain relationship when stress testing a sample at a stress value at a stress value higher than the sample has experienced in previous testing. Therefore, often before characterising conductive particle elastomer composites, the composite sample should be subjected to a stress larger than that of the intended future experimentation stresses.

It is well known in literature and is intuitive that mechanical characteristics of a DEA's compliant electrodes have a significant effect on the actuation performance [219, 223] . However, there has been a lack of empirical evidence and subsequent modelling on quantifying how much the thickness of a piezoresistive composite electrode effects actuation performance. This work provides empirical data to begin creating and validating models for thick electrode DEAs, as a step towards creating an objective function to optimise for a DEA for both actuation and sensing performance.

5.4.3 EIT Validation

A metric used to determine the minimum resistance change measured and hence pressure sensed is the noise factor, *NF*. *NF* is analogous to SNR, but instead using EIT reconstruction noise vs EIT voltage data noise. It was found that for increasing values of z_{ce} the *NF* values also increased. This noise correlation is exemplified in Figure 5.14.

EIT was used to map nine compressive loads applied throughout the material successfully. To compare the performance of each thickness of the compliant electrode the spatial resolution was quantified using two main performance metrics, E_{CoM} and SF. For increasing thickness of compliant electrode the E_{CoM} and its standard deviation decreased by almost an order of magnitude. However, the SF values were all within the same order of magnitude and had decreasing standard deviations for increasing z_{ce}.

The vectorised format of the E_{CoM} gave a good indication of consistent biases that were present in the sample domains when compared across several repetitions of the same experiment. The vectorised E_{CoM} values do not appear random and may instead be due to inhomogeneity. This data could be used in future in a calibration stage to determine how pressure sensed in particular regions may be spatially biased and preemptively corrected.

To ensure the EIT domain reconstruction was geometrically accurate the circumferential electrodes were modelled in the meshing software to the same width as the real circumferential electrodes. However, the embedded depth of the circumferential electrode was not modelled. Due to the manual nature of the fabrication, significant error of up to 3 mm in the circumferential spacing of the rigid EIT electrodes was present, a factor which would be improved in future iterations especially if automated fabrication were to be implemented.

5.4.4 Simultaneous Actuation and Mapping

The DEA-EIT device constructed in this work has been shown to complete simultaneous actuation and pressure mapping using the method shown in Figure 5.11.

There was no significant noise generated due to an active DEA electrode at a steady state voltage, however this may vary with rapid large loads which change the DEA capacitance and cause a large transient on the grounded EIT compliant electrode. The pressure mapping for 1 - 7 kV scenarios is shown in Figure 5.17.

The transients induced by the large sudden voltage changes are shown as crescent shaped artifact in Figure 5.18. The artifact seen in the image is due to an increase in the grounded DEA electrode voltage at a certain point during the data collection sequence of the EIT voltages.

Not all transient events were captured, which was due to aliasing. A lower EIT sample frequency and higher resolution 'DEA transient'-'EIT data capture' synchronisation would aid in capturing these events more accurately.

This technology show promise and can be further optimised for improved actuation and pressure mapping capability. A system architecture integrating both DEA and EIT-based pressure mapping functionality into a single device is done using the components in Figure 5.10.

5.4.5 Altered Actuation Performance

During a compressive load event to an actuated DEA-EIT device, the DE thickness is decreased which increases the electrostatic stress, Equation 5.2, induced by the same voltage. Therefore during a compressive loading event the stress applied to the material is a combination of the external compressive load and the increased electrostatic load.

Often a DEA is pre-stretched to take advantage of the hyper-elastic region of DE material so for a smaller change in electrostatic stress, $\Delta\sigma_{es}$, a larger strain, $\Delta S_{z_{de}}$, can be achieved. An externally applied load may mean that the stress-strain region the material may be in is changed (i.e. from a linear to a hyper/hypo-elastic region) and the same $\Delta\sigma_{es}$ would have a different $\Delta S_{z_{de}}$.

5.4.6 Dielectric Breakdown

During a compressive load event to an actuated DEA-EIT device, the DE thickness is decreased which increases the concentration of charge in the strain area. Both factors increasing the likelihood of dielectric breakdown within the material.

Feedback from the EIT pressure sensor could be used to decrease the actuation voltage if the device receives a strain that is likely to cause a dielectric breakdown.

An un-explored research avenue is the structural health monitoring of DEAs using EIT. It may also be possible to alter the system given in this work to map the location and size of any dielectric breakdown using EIT concurrently on each compliant electrode. This would allow for more technology to be developed around the self-healing of DEAs.

5.5 CONCLUSION

This work demonstrates the effective integration of Electrical Impedance Tomography (EIT) with Dielectric Elastomer Actuators (DEAs) for simultaneous pressure mapping and actuation. The findings indicate that the use of piezoresistive nanoparticle elastomer composites (PNEC) allows for the emulation of pressure sensing akin to human mechanoreceptors, enhancing the sensitivity and responsiveness of DEAs in various applications. Effective bulk moduli values were found to quantify the mechanical actuation impedance of each compliant electrode thickness used, ranging from 334 to 966 kPa. Force mapping was successful with decreasing degrees of mapping error with increasing compliant DEA electrode thickness. The best mean centre-of-mass error of 1.66 $\pm$ 0.17 mm was found for the thickest, 2 mm, compliant DEA electrode used.

The work highlights the importance of electrode thickness on the performance of pressure mapping, revealing that thicker electrodes may improve the detection of pressure changes due to their lower noise factors. The results suggest that the EIT method can provide valuable feedback for controlling actuation, potentially preventing issues such as dielectric breakdown by adjusting voltage levels in response to detected strain.

Moreover, the research opens avenues for structural health monitoring of DEAs, enabling the mapping of dielectric breakdown locations and sizes, which could lead to advancements in self-healing technologies. Overall, the integration of EIT with DEAs not only enhances their functionality but also broadens their applicability in fields such as robotics, soft actuators, and wearable technology, paving the way for future innovations in smart materials and systems.

Chapter 6

Unintentional Power Generation in a DEA-EIT Sensor-Actuator Device

ABSTRACT

This study investigates the phenomenon of unintentional power generation in Dielectric Elastomer Actuator (DEA) devices integrated with Electrical Impedance Tomography (EIT) for pressure mapping applications. While DEAs are primarily designed for actuation, they can inadvertently function as Dielectric Elastomer Generators (DEGs) due to localized mechanical strain during operation. The research explores the mechanisms behind this unintended energy generation, focusing on the changes in capacitance that occur when the DEA is subjected to varying loads. Through experimental simulations, the study quantifies the energy produced, revealing that energy generation can range from 0.2 μJ to 4 mJ depending on the load conditions. The findings highlight the dual functionality of DEAs, emphasizing the need for careful management of energy generation to prevent potential damage to connected circuitry. This work contributes to the understanding of DEA-EIT devices and their applications in soft robotics and energy harvesting, suggesting that while unintentional, the energy generated could be harnessed for practical use in various scenarios, including vehicular and foot traffic loads. With further research and development the DEG energy from this work could be used to power the EIT sensing circuit extending the range of possible applications.

6.1 INTRODUCTION

Dielectric Elastomer Actuators (DEAs) and Dielectric Elastomer Generators (DEGs) share a similar form whereby they both have compliant conductive electrodes either side of a dielectric elastomer (DE) membrane. However, DEGs represent a class of electromechanical devices that harness mechanical strain to generate electrical energy. DEAs and DEGs can often utilise the same soft electroactive area for actuation and power generation, but differ in the connected electronics. These devices exploit the properties of dielectric elastomers, which are soft, flexible materials capable of undergoing significant deformation. This deformation can be utilised to generate electrical power, making DEGs a promising technology for energy harvesting applications. However, DEGs can also arise as an unintended consequence of loading a DEA device.

In typical DEG configurations, the focus has been on uniform, global strain changes within the dielectric elastomer domain. Previous research has concentrated on scenarios where the entire thickness of the DE is reduced as a result of applied strain, leading to energy generation due to global DE deformations [200, 213, 224].

In contrast, this work explores unintentional DEG scenarios that have arisen from the invention of a hybrid actuation and pressure mapping DEA-EIT device. By investigating the effects of localised thickness reduction within the DE caused during a load event during DEA switching, we observe unintended power generation due to the change in the device capacitance.

This localised approach introduces a new dimension to DEG functionality, where strain is not uniformly applied but concentrated in specific areas. This DEA-EIT integration, as discussed in Chapter 7, allows for precise monitoring and analysis of localised deformations, thereby enhancing understanding potential scenarios where DEG behaviour may occur. In the existing literature, neither the intentional nor unintentional use of a DEA-EIT-like device as a DEG, when subjected to localised loads, has been investigated at the time of writing this work.

6.1.1 BACKGROUND

Before describing how a dielectric generator arises in DEA-EIT device, it is important to understand the function of a DEA-EIT device first as described in detail in the previous chapter. A DEA-EIT device can use the same compliant electrodes and dielectric elastomer to function both as an electro-active actuator and pressure mapping sensor. The DEA function consists of applying a high voltage to a bottom electrode leaving the top electrode as the low voltage electrode which performs as the pressure mapping surface. The pressure mapping surface is piezoresistive and uses electrical impedance tomography to map any changes in resistance and hence any loads throughout the electrode surface.

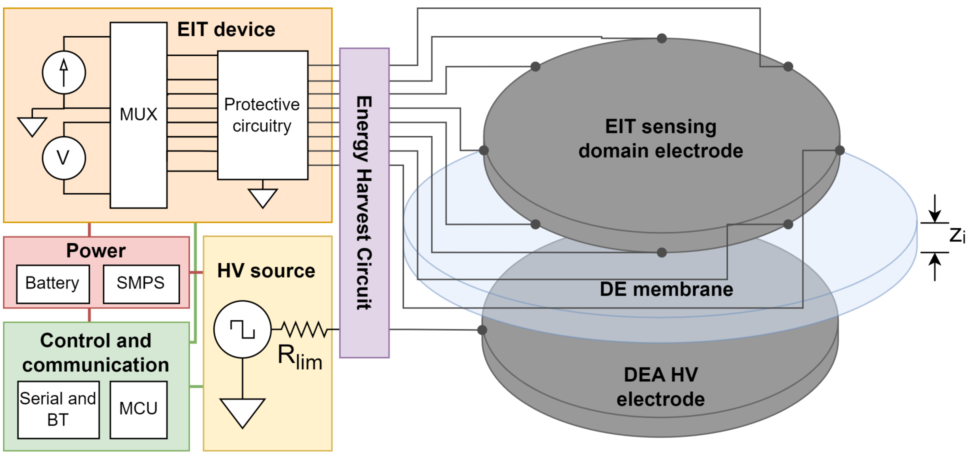

FIGURE 6.1: Architecture of a DEA-EIT pressure mapping and actuator device with an exploded view of the DEA stack.

A DEG may be incidentally be created during simultaneous DEA-EIT operation. This effect will take place when the DEA experiences sufficiently large external strains and DEA voltage switching at specific times. This DEG sequence is shown in Figure 6.2 and is explained as five distinct stages.

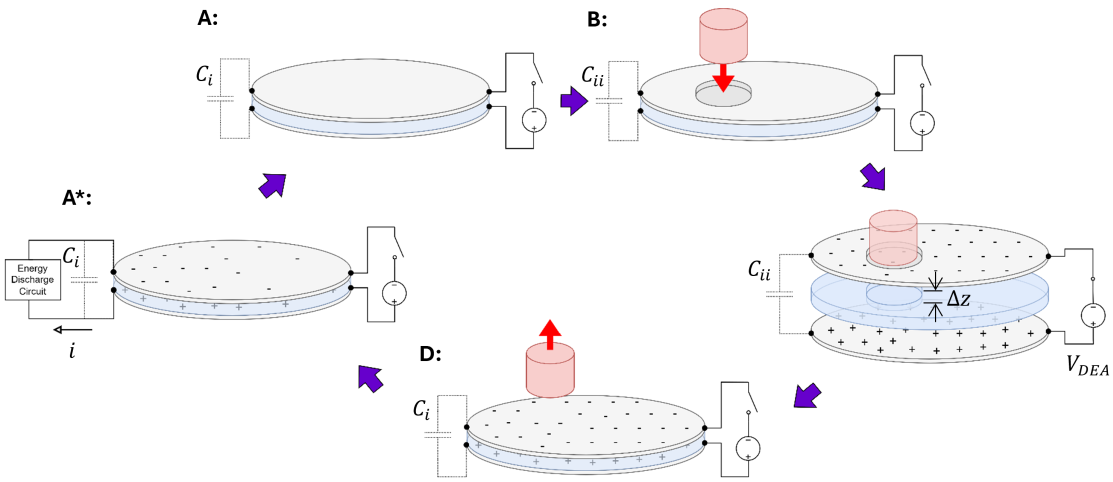

FIGURE 6.2: Dielectric elastomer generator scenario sequence with a localised compressive load.

Where C_i is the initial capacitance of the DEA, C_{ii} is the 'primed' capacitance of the DEA, the positive and negative signs, $+$ and $-$, on the compliant electrode represent electrical charge, and the red cylinder represents the load applicator. The typical operation of a DEG consists of the five main stages described below and exemplified in Figure 6.2. Note that the changes in electrostatic force due to loads are ignored.

State A: the DEA has an initial capacitance of C_i, is deformation free, and has zero voltage applied across the compliant electrodes.

State B: the DEA is compressed and deformed with a localised change(s) in thickness of the DE, Δz, increasing the DEA capacitance to C_{ii}. Work is done on the DEA by the compressive load storing elastic potential energy in the strained DE. As derived from Hooke's law the elastic potential energy, U_ε for a material of Young's modulus, Y, cross-sectional area, A_i, original thickness, z_i, and change in thickness, Δz is given in Equation 6.1. This equation is for a singular body with an even change in thickness across the area, A_{DE}, showing the core parameters governing the elastic potential energy.

$$U_\varepsilon = \frac{Y A_0 \Delta z^2}{2 z_i} \tag{6.1}$$

State C: An applied voltage, V_i, across the compliant electrodes generates electrical charge. The total charge developed, Q, is given by Equation 6.2.

$$Q = C_{ii} V_i \tag{6.2}$$

Charging the electrodes gives electrical potential energy to the DEA as it is now a charged capacitor. The electrical potential energy of the DEA is given by Equation 6.3.

$$U_{E(C)} = \frac{1}{2} C_{ii} V_i^2 \tag{6.3}$$

State D: The DEA is unloaded and returns to its original state with capacitance, C_i, while maintaining the same charge Q causing the voltage to increase to V_{ii} as shown by Equation 6.4.

$$V_{ii} = \frac{Q}{C_i} \tag{6.4}$$

When the load is released the elastic potential energy, U_ε, is used as the DEA returns to a relaxed state. In parallel, the increase in voltage on the DEA increases the electrical potential energy, $U_{E(D)}$ as shown by Equation 6.5.

$$U_{E(D)} = \frac{1}{2} C_i V_i i^2 \tag{6.5}$$

Resulting in a gain of electrical potential energy ΔU_E comprising the difference of U_{EC} and U_{ED}.

State A*: The DEA is discharged into the energy harvesting circuit returning the charge and voltage values across the DEA to zero, returning to State A.

The unintended power generation discussed may cause issues with the pressure measurement system if switching significantly high DEA voltage source is done during a significant DEA-EIT surface loading event. A significant loading event is one which changes the capacitance of the DEA such that a voltage is generated by the unintended DEG which is high enough to cause potential harm to the EIT driving circuitry.

6.2 METHODOLOGY

To confirm the existence of this DEG phenomena in the DEA-EIT device design has undergone a sequence of FEM studies. To determine which compressive loads may give significant capacitance changes that could lead to significant voltage amplification and potentially significant energy generation across DEA electrodes, FEA of a DEA undergoing compressive pressure loading events have been completed. Experimental cases using two different loading areas, as shown in Figure 6.4, with a range of forces were completed. All FEA studies were three dimensional to account for any potential non-symmetric results and variations in fringe effects.

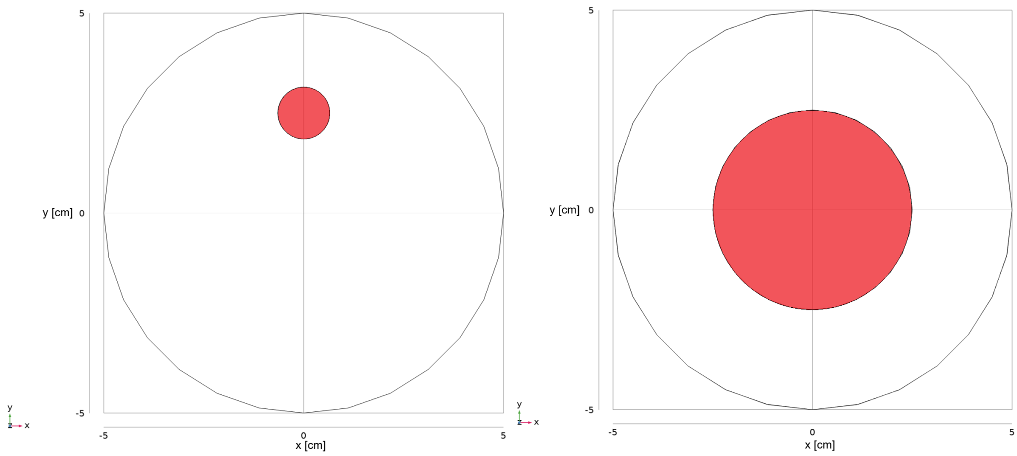

FIGURE 6.3: Loading cases for analysis of capacitance change. Left: 13 mm diameter load. Right: 50 mm diameter load.

6.2.1 DEA Load Study

To obtain a representation of how the DEA structure will deform during a different loading events, a static load FEA study was performed to determine the expected deformation of the DEA and create mesh models. The deformed mesh models were then used for further electrostatic FEM studies to determine the change in capacitance of the DEA structure.

The materials used for the FEA load study were closely matched to the characteristics of the material used in previous work [21] . For the compliant electrode a Young's modulus of 100 kPa was used with a Possion's ratio, ν_{ce} of 0.4, an electrode thickness, z_{CE}, of 0.5 mm, and the diameter of 100 mm. The DE material Young's modulus was set to 90kPa with a Poisson's ratio, ν_{DE}, of 0.49, a membrane thickness, z_{DE}, of 0.5 mm, and the diameter of 100 mm.

A static load analysis of the circular areas shown in Figure 6.3, for a range of force values. The loads ranged from 2.5 to 240 N, to obtain comparable strain values to those seen within our previous research [21, 157] . The bottom electrode surface was assumed fixed in place and rigid to simulate a typical application case where the compliant DEA-EIT material is adhered to a rigid body.

A mesh of the deformed DEA models from each of different load case was saved for use in the next study.

6.2.2 Deformed DEA Electrostatics Study

The deformed meshes from the previous load study were used to generate new meshes for an electrostatics study. To determine the change in capacitance from the undeformed DEA model and the deformed DEA cases, an electrostatic study was performed. The same dimensions as the load study were used the compliant electrode was assumed to have an ideal conductivity and the DE membrane relative dielectric permittivity was set to 4.2 as seen in the other studies done on similar DE material [218]. The a positive voltage was set on the upper electrode and the lower electrode was grounded. After the electric field model was generated using COMSOL Multiphysics [225] for each case the compliant electrode capacitance was calculated using Maxwell's capacitance matrices [226] .

6.2.3 Voltage and Energy Generation

The voltage increase and energy generated for each DEA load case was calculated from the capacitance values determined in the electrostatics studies using Equations 6.2 - 6.5. Analysis of which types of loads can be handled by the DEA-EIT device when undergoing high voltage switching is a critical step for determining the limitations of future applications of the DEA-EIT device. The capacitance results generated from the FEA studies are then validated using Equation 6.6.

$$C = \varepsilon_0 \varepsilon_r \frac{A}{z} \tag{6.6}$$

Where ε_0 is vacuum permittivity, ε_r is the relative permittivity of the dielectric, A is the area of the 'infinitely' large parallel plate electrode, and z is the dielectric thickness.

6.3 RESULTS

The a series of models were generated from a sequence of FEM studies to obtain the voltage and energy generated from a DEA acting as a DEG. First results from a static mechanical load analysis are shown followed by an electrostatic analysis and finally capacitance and energy results were derived from the electrostatic FEA results.

6.3.1 DEA Load Study

To determine how various localised loads deform the DEA-EIT device structure FEM was performed. Examples of the deformations caused are given in Figure 6.4.

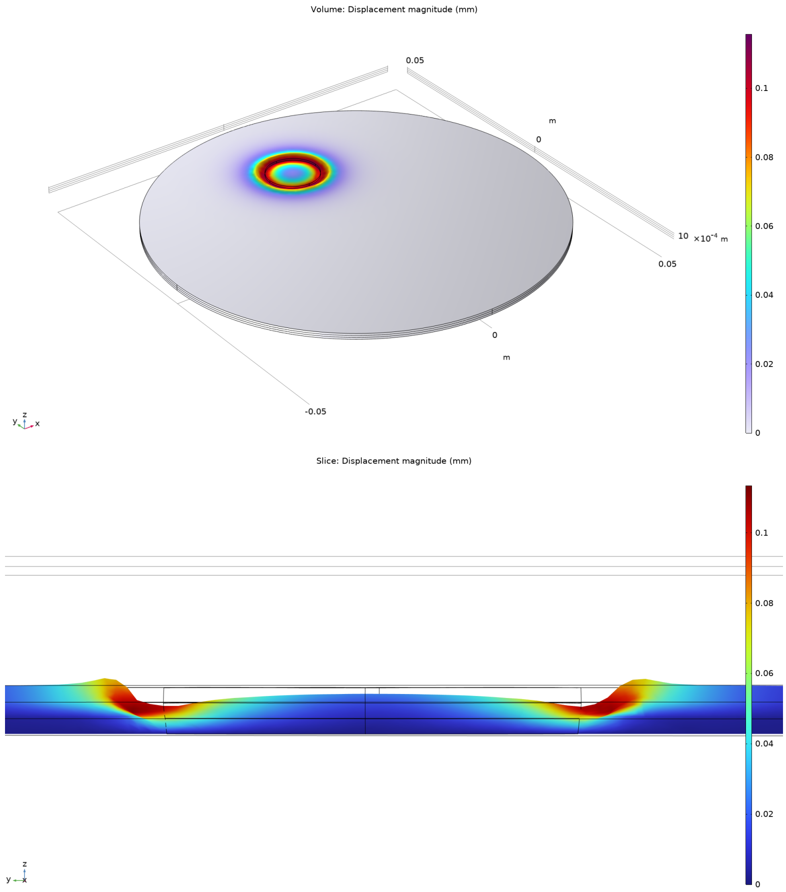

FIGURE 6.4: Deformed mesh plot of 13 mm diameter 20 N load case FEM model (x10 scale displacement). Top: 3D view. Bottom: Cross-section zoomed view.

6.3.2 Deformed DEA Electrostatics Study

The deformed DEA-EIT structure causes the overall capacitance across the device electrodes to increase. The first step was running an electrostatic FEM study to generate an electric field, as shown in Figure 6.5.

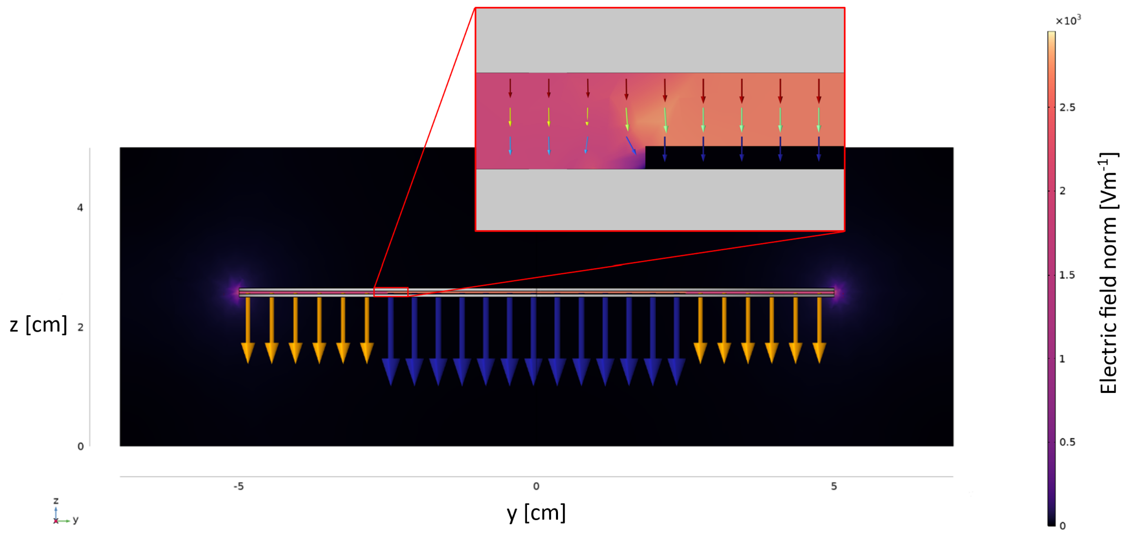

FIGURE 6.5: Electric field simulation of 50 mm diameter 240 N load case. With a zoomed section to show the electric field around the shoulder of the load cross-section. Volumetric arrows proportional to electric field.

6.3.3 Voltage and Energy Generation

The parallel plate assumption for calculating capacitance of the DEA-EIT becomes invalid for the deformed DEA-EIT device. An approximation using the electric field FEM result on the deformed DEA-EIT FEM result is used using Maxwell's capacitance matrix.

To show the scale at which energy is generated an example scenario for the extra voltage generated is given. Given that the values from Figure 6.2 are, $C_i = 10pF$, $C_{ii} = 15pF$, and $V_i = 5kV$. We get a charge $Q = 75nC$, and then at stage D, $V_{ii} = \frac{Q}{C_i} = 7.5kV$. This gives a voltage change, $\Delta V = +2.5kV$.

TABLE 6.1: Voltage and energy generation results calculated from FEM values for the 13 mm diameter load cases.

Load [N]	**ESTRN**	**C [pF]**	**dC [pF]**	**dV_DE [V]**	**dU [uJ]**
0.00	0.00	588.86	0.00	0.00	0.00
2.50	0.08	589.69	0.83	7.04	31.14
5.00	0.15	590.73	1.87	15.83	70.20
10.00	0.30	593.40	4.54	38.25	170.68
20.00	0.60	605.53	16.67	137.65	630.86
30.00	0.91	688.18	99.32	721.61	3903.68

Table 6.2: Voltage and energy generation results calculated from FEM values for the 50 mm diameter load cases.

Load [N]	ESTRN	C [pF]	dC [pF]	dV_DE [V]	dU [uJ]
0.00	0.00	588.86	0.00	0.00	0.00
10.00	0.02	591.90	3.04	25.68	0.20
20.00	0.04	595.00	6.14	51.60	0.79
30.00	0.06	598.33	9.47	79.14	1.87
60.00	0.12	609.24	20.38	167.26	8.52
120.00	0.24	635.86	47.00	369.58	43.43
240.00	0.48	727.10	138.24	950.63	328.54

To validate the capacitance results form Tables 6.1 and 6.2 the the capacitance was solved analytically using the parallel-plate capacitance approximation given in Equation 6.6. Matching the parameters of the FEA simulation the capacitance of the 100 mm DEA device with no load applied, the capacitance was approximated to be 584.13 pF.

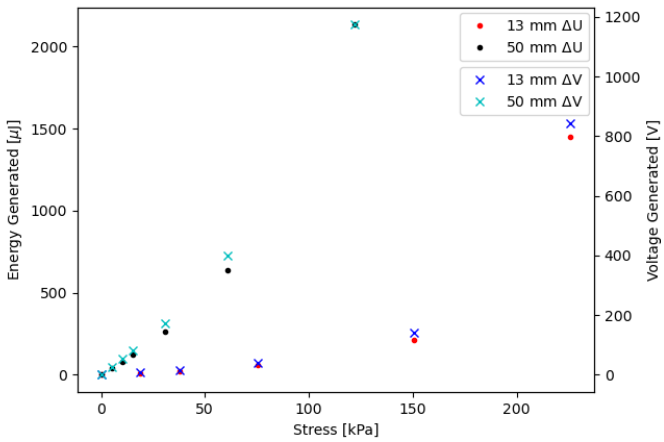

Figure 6.6: Observing the trends from the energy and voltage generation results for the range of loads applied.

6.4 DISCUSSION

The results from this work show promise towards understanding the energy generated from an EIT-DEA device when used in a particular fashion. The FEA simulations completed were validated analytically with a small discrepancy of 4.73 pF, i.e. 0.8% error, due to the electric field fringe effects the parallel plate capacitor assumption does not account for. The plot shown in Figure 6.6 shows the trends for a 13 mm and 50 mm load applicator, from this the prominence of the decreasing dielectric thickness can be seen to give a large increase in voltage and energy generated. At these high strains the likelihood of dielectric break through is significantly increased, especially so in a real world scenario when the load surface may contain sharp features.

The energy generated by the sequence shown in Figure 6.2, can be harnessed if there is a sensing mechanism put in place to determine when the capacitance of the DEA will change and apply the voltage appropriately. Conversely, this energy generation can be undesirable for certain applications as it may cause damage to the attached circuitry.

Such energy generation case may be avoided in a system by detecting that a pressure event has occurred and preventing the excitation of the DEA or limiting the charge accumulation on each plate of the capacitor.

An example scenario of voltage and energy generation was given in Section 6.3.3. This voltage change transient is connected to the EIT multiplexer through the capacitance of the DEA, as shown by Equation **??**. The multiplexer pins used in this case are limited to between the power rails, i.e. ±22 V [152]. In the case described above the minute change in capacitance of the DEA is calculated to generate 93.75 μJ of energy.

To determine the device's tolerance against transient voltage spikes, the EIT multiplexer limits would need to be characterised. Otherwise, in the case of an input pin overvoltage CMOS latch-up may occur [227] . Typical ESD standards [**?**] state that electronic devices must be tolerant to 200 pF capacitance charged to ±15 kV, giving an energy dissipation of 22.5 mJ. This is several orders of magnitude larger than the energy generated in the simulation results shown in Tables 6.1 and 6.2. However, for different configurations of DEA device this energy generation may become significant.

The Poisson's ratio of the DE and the compliant CBSR electrodes differs due to viscoelasticity and micro-porosity seen in this material as shown by the SEM images in Figure **??**, Chapter **??**. To determine the Poisson's ratio more accurately for the composite material, empirical data should be gathered as there is limited data for similar composite material with microporosity.

6.5 CONCLUSION

This work has investigated the prominence of energy generation of a 100 mm diameter DEA device with a 500 μm dielectric elastomer. The sequence by which this energy generation occurs has been explained, and several scenarios have been tested for energy generation from localised 13 mm and 50 mm diameter loads. Depending on the load force 0.2 μJ to 4 mJ of energy generation has been estimated. Although these are small values, often DEAs require large voltages to actuate so any amplification of these voltages needs to be handled on a case by case basis for each application and DEA device. Using methods to estimate the occurrence of a change in DEA capacitance is recommended in all applications to either avoid or harness this energy generation. Potential future applications of a device that utilises this energy generation ranges from vehicular traffic loads to foot traffic loads. Application examples where energy generation is undesirable are given Chapter **??**. In future work we strive to make a system whereby the energy generated from the DEG can be harvested and used to power the EIT-based pressure sensing circuit.

Chapter 7

A Portable Electrical Impedance Tomography Based Pressure Mapping Sensor and Validation System

The content from this chapter is contains content from the manuscript to be published in the Journal HardwareX.

7.1 Abstract

This work presents portable, low-cost hardware for pressure mapping using EIT-based soft sensors. An important part of developing these EIT-based pressure sensors is the sensor characterisation. Therefore, this work also provides the design of a system for characterising and validating the spatial, pressure, and temporal performance of different soft sensor material domains. The system is capable of driving soft EIT-based sensors using a range of sensing materials, shapes, and configurations. The hardware allows for the wireless transmission of EIT data to a remote device. A data capture frame rate of 12.7 Hz allows for the analysis of dynamic events. The maximum current drive voltage is ± 22 V and a voltage read resolution of $\pm 0.3\ \mu V$ allowing for a range of sensing domain sizes, thicknesses, and materials. A Cartesian force applicator device has been developed for the automatic characterisation of rates of 0 - 800 mm/min for can sense loads from 0 to 100 N with a resolution of ± 50 mN. Loads can be applied with an error of ± 0.01 mm. A standardised method has been provided for researchers to experiment with a range of different sensing domain materials and shapes. The system described in this work is suitable for both research and practical applications, making it a valuable tool for advancing the field of EIT-based soft sensor technology.

Table 7.1: Specifications table

=1ex to —X—X[3,l]—

Hardware name	EIT Pressure Mapping Device and Calibration System
Subject area	Engineering and material science
Hardware type	[noitemsep, topsep=0pt]Imaging tools Measuring physical properties and in-lab sensors Mechanical engineering and materials science
Closest commercial analogue	No commercial analogue is available.
Open source license	General Public License (GPL)
Cost of hardware	ERT sensor device : USD$148 Cartesian force applicator device : USD$1046 (incl. Prusa MK3s 3D printer - USD$899)
Source file repository	http://doi.org/10.5281/zenodo.11520112

7.2 Hardware in context

Electrical impedance tomography (EIT) is an imaging technique used to map impedance/resistance throughout a material using multiple boundary electrodes. The boundary electrodes inject current through the homogeneous domain instead of a patterned or layered one, allowing the sensor measurements to be non-invasive.

EIT is most commonly used for thorax imaging for clinical respiratory analysis; however, this same method can be used for a multitude of applications with conductive bodies to map changes in impedance/resistance. Commercial devices that perform EIT, or the DC equivalent electrical resistivity tomography (ERT), exist in large-form factors such as Pulmovista 500 (Draeger, Luebeck, Germany), EIT16/32 (Sciospec Scientific Instruments GmbH, Leipzig, Germany), LuMon (Sentec, Lincoln, USA), Zeta (Zonge International, Tucson, USA), WGMD-4 (WTS Geophysical, Wanchai, Hong Kong). All of these options are application-specific for biomedical and geophysical applications. Several research papers [113, 228**? ? ?** –233] have described similar but smaller versions of the commercial products mentioned. In this work the same physics principles used in bio-medical and geophysical sensing are used to map localised compressive loads on a soft piezoresistive material. Pressure mapping is widely used for many applications including sports equipment grip analysis, foot pressure in gait analysis, in production line part alignment, hospital patient bed and chair pressure minimisation, headphone pressure analysis, amongst many others. These applications are useful for increasing quality of life, optimising sporting performance, object detection, and production efficiency optimisation.

A core limiting factor of current technology is the lack of customisability in sensor size, shape, sensing domain material softness, and sensing material composition [162, 175, 176, 178]. Most often, pressure sensors are given in a rectangular format because of the arrays of wiring and sensing elements required within the sensing domain. EIT-based pressure mapping sensors are not constrained by wires or complex patterning within the sensing domain area. EIT-based pressure sensors can have a homogeneous sensing domain configured in various shapes. To advance the research of this soft pressure mapping platform technology, we require a system that is lost cost, open source, easy to use, portable, and sufficiently flexible to test a range of different sensing domain materials. The system developed in this work is for the research and development of EIT-based pressure mapping sensors.

The hardware of our system has two key components, a circuit for gathering raw ERT data and a Cartesian force applicator (CFA) machine for characterising an ERT-based pressure mapping sensor. The system characterises the sensor and can be used for validating the spatial, pressure, and temporal performance for different piezoresistive sensor material domains. The CFA allows for repeatable experiments and quantifiable data for different sensor configurations.

7.3 Hardware description

Created an EIT-based pressure mapping sensor toolbox that reliably and repetitively allows for EIT-based pressure mapping and quantification of the sensor performance. The overall system is simple to construct and easy to operate and is split into two main parts: the ERT sensor and the CFA device.

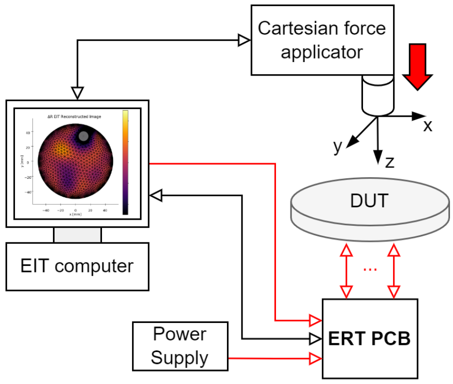

FIGURE 7.1: System architecture of ERT sensor and CFA setup. The large red arrow shows the direction of the force applicator compression onto the sensing domain (DUT) and analogue/power signals are shown with red arrows and digital signals with black arrows.

The ERT sensor consists of an ERT sensor circuit and the sensing domain under test (DUT). The ERT circuit drives the EIT measurements through the sensing domain soft elastomer composite material. The EIT circuit designed is small (79 x 94 x 12 mm) for potential use in space-constrained mobile applications. The system has a programmable current source which can drive up to 50 mA of constant current. The voltage measurement circuit has an ADC resolution of 0.3 μV, ensuring that the small signals generated by small localised loads can be detected. The sensing domain in this work is a soft piezoresistive composite made from carbon black (CB) powder and silicone rubber with 16 boundary electrodes made from gold pins and copper tape, as seen in Figure 7.6.

FIGURE 7.2: A soft sensor domain connected to the ERT sensor electronics.

To ensure that the sensor can accurately locate pressure points and their magnitude, the CFA device described in this work is used to apply compressive forces at various locations. The CFA test bed allows for loads within a 220 x 180 mm area.

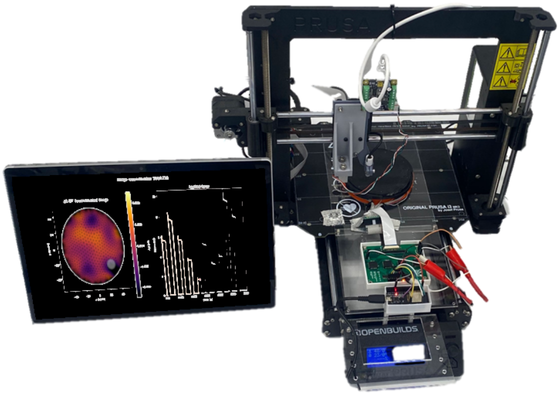

FIGURE 7.3: Cartesian force applicator setup with an ERT circuit and EIT reconstruction computer

Previous research groups have developed EIT hardware for pressure mapping sensors [105, 113, 169, 182, 234]; however, a complete open-source system including validation hardware has not yet been published.

To move the field of EIT-based soft pressure mapping forward, there is a need to optimise materials for qualities such as pressure sensitivity, homogeneity, electrode connectivity, and dynamic viscoelastic properties. This CFA automates the testing process with easily changeable spatio-temporal parameters, such as strain magnitude, strain rate, and strain profile. This system standardises the analysis of the pressure mapping by allowing for the EIT reconstructed resistance images to be compared with stress and strain data form the sensing domain material.

The hope for the hardware and software given in this paper is that it will provide a standardised platform for future researchers to use to further quantify the utility of other sensing materials, and their compare their performance metrics with standard loading test procedures, as done in our previous work [21].

The ERT sensor and force applicator hardware could be utilised in further research for:

- 2D piezoresistive material analysis
- Pressure mapping device characterisation and performance
  - Spatio-temporal performance
  - Dynamic stress sensing performance
  - Piezoresistivity
- Development for real-world applications
  - Robotic skin integration
  - Sports sensing
  - Prosthetic limbs

7.4 Design files summary

The ERT pressure mapping sensor contains a PCB assembly, housing, and wiring. The CFA design includes a selection of off-the-shelf parts as well as custom designed mechanical CAD parts. Table 7.2 contains all of the custom designed parts from the system as well as the software for both the ERT sensor and CFA devices. In this work the mechanical CAD files were generated using Solidworks and the electrcial ECAD files were generated using KiCAD. Programs designed for this system were mainly written in Python and C.

TABLE 7.2: Summary of all design files.

=1ex to —X—X[0.65,1]—X[0.35,1]—X[0.8,1]—

Designed parts	File types	Open source license	Location of the file
PCB design	elec CAD (.kicad_sch, .kicad_pcb, .kicad_pro)	GPL	10.5281/zenodo.11520112 /ERT_sensor/elec_CAD/
3D printed housing	mech CAD parts (.stl, .sldprt)	GPL	10.5281/zenodo.11520112 /ERT_sensor/mech_CAD/
PCB firmware	embedded firmware (.c)	GPL	10.5281/zenodo.11520112 /ERT_sensor/firmware/
ert_sensor_bom.csv	bill of materials	GPL	10.5281/zenodo.11520112 /ERT_sensor/
Fabricated parts	mech CAD parts (.stl, .sldprt)	GPL	10.5281/zenodo.11520112 /CFA/mech_CAD/
Testing software	data capture/ processing (.py)	GPL	10.5281/zenodo.11520112 /CFA/software/
cfa_bom.csv	bill of materials	GPL	10.5281/zenodo.11520112 /CFA/

7.4.1 ERT pressure mapping sensor file descriptions

PCB design - KiCAD project files including the electrical schematics and PCB layout for the ERT sensor circuit.

3D printed housing - CAD files for 3D printed sensor enclosure and a sensor domain holder example.

PCB firmware - Firmware for the ERT data capture driving the electrode drive pattern through multiplexer switching. The data captured is then streamed via serial to a seperate reconstruction processor.

ert_sensor_bom.csv - Bill of materials for all parts and components in the ERT PCBA.

7.4.2 Cartesian force applicator file descriptions

Fabricated parts - CAD for 3d printed and laser cut parts for the modification of the 3D printer platform into a CFA.

Testing software - Software for simultaneous force, position, and ERT data acquisition and processing.

cfa_bom.csv - Bill of materials for all parts in the CFA system apart from the ERT sensor electronics.

7.5 Bill of materials

Please refer to the two detailed bills of materials (BOMs) given in Table 7.2.

7.6 Build instructions

The build is separated into two parts. The first being the assembly of the ERT sensor electronics and housing. The second being the build of the Cartesian force applicator. Text within square brackets refer to the part reference designators (e.g. U1 for the ESP32 module) in the BOMs.

7.6.1 ERT Sensor

The manufacturing process of the PCB involves first sending the PCB gerber files to a PCB manufacturer. This work used JLC PCB with their default parameters for a 4 layer PCB.

Next populate the PCBs with the SMD parts given in the BOM and place in a reflow oven. First complete the rear side then the top side to ensure components stick. Once all SMD parts have been firmly soldered, solder all of the THT components. Finally attach the jumpers for the desired power mode, explained in Section 7.8.1.

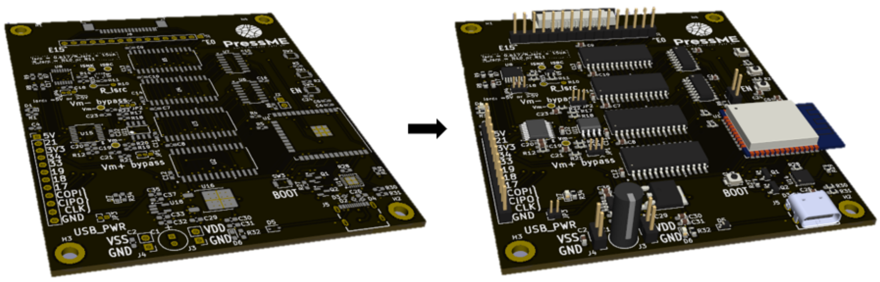

FIGURE 7.4: ERT PCB [PCB1] before and after electrical component population.

To ensure simple protection against electrical shorts and low-level ingress protection (equivalent to IP20) 3D print an enclosure in PLA using the STL files given in the

BOM, *ert_housing_top.stl* [PR1] and *ert_housing_base.stl* [PR2]. There are 4 threaded inserts [HW2] to mount the PCB securely in the 3D printed enclosure using four M3 14 mm bolts [HW1].

Attach the 16 way ribbon connector [W1] to the ERT electrodes. In this example there is a ribbon to IDC connector interface board [J8], which then connects to a custom built electrode pin to domain interface [DUT1, DUT2, PR3, PR4]. This electrode interface will vary based on the required sensing domain.

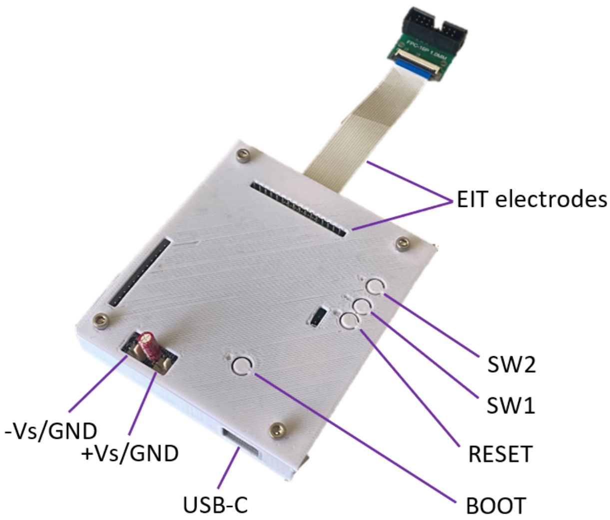

FIGURE 7.5: ERT sensor PCBA mounted in enclosure and attached electrode harness showing buttons and the main electrical connections.

The sensor device shown in Figure 7.5 shows all of the connections and buttons necessary for the programming and operation of the sensor, as well as two optional buttons SW1 and SW2 for any other desired functions.

7.6.2 Sensing Domain

As a reference the method for fabricating a specific sensing domain is given in this section. The sensing domain used was a carbon black (CB) nanoparticle silicone rubber composite.

With the material requirements of a low Shore hardness of 5A - 25A, similar to that of human skin and muscle tissue [160, 184], low viscoelasticity, high yield strength, low resistivity, high strain gauge factor, and non-toxic. Other sensor domain materials may be used for the sensor, such as soft conductive particle composites, conductive polymers, and hydrogels [113, 128, 146].

Researchers fabricating their own sensing domain for use with this system should follow three key requirements,

1. The size of the sensing domain must fit within a 220 x 180 x 160 mm volume (X×Y×Z) on the CFA test bed.

2. The bulk modulus of the domain material must be chosen such that the required loads applied to the domain must not exceed 100 N.

3. The inter-electrode resistance, R_{int}, must be low enough to not saturate the current source, I_{src}, given a power supply voltage, V_s, as shown in Equation 7.1,

$$R_{int} < \alpha \frac{V_s}{I_{src}} \tag{7.1}$$

Where R_{int} is the resistance values between every configuration of the current drive electrodes during an EIT capture cycle and α is the factor of safety for any electrode movement or incidental increase of R_{int} during experimentation.

The domain under test (DUT) used in this work was a composite comprised of XC 72R carbon black (CB) nanoparticles (Cabot, Alpharetta, USA) [DUT5] of 50 nm average diameter, dispersed in a two part Dragon Skin 10 NV silicone rubber (SR) matrix (SmoothOn, Macungie, USA) [DUT6]. The weight percentage (wt%) of CB to liquid silicone rubber which resulted in near optimal piezoresistive characteristics was found to be between 8 - 10%. To ensure homogeneous CB particle dispersion and mitigate air bubble formation an ARV-310 vacuum planetary mixer (Thinky, Tokyo, Japan) was used to mix the CB particles through the liquid silicone matrix. Upon completion of mixing, the uncured composite was poured into the circular sheet domain mould. The curing of the composite was controlled by heating the newly-mixed material in the mould at 80°C for 90 min. The domain samples used in this work and previous work [20, 21] had a diameter of 100 mm as shown in Figure 7.6.

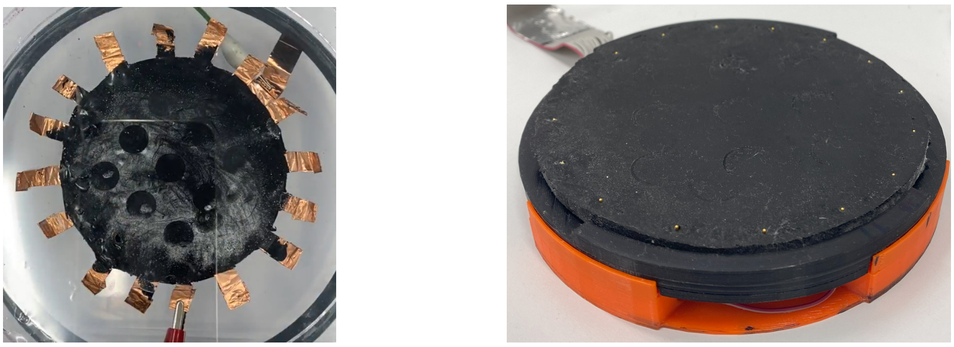

Figure 7.6: Left: An example of a CBSR sample with copper tape electrodes integrated with a dielectric elastomer actuator setup [?]. Right: Example of a CBSR sensing domain with gold pin electrodes penetrating material surface around the sensing region boundary.

7.6.3 Cartesian force applicator

To test the spatial and force resolution of the ERT pressure mapping device, the CFA was designed using a Prusa MK3s 3D printer to provide a stable platform. First a functional Prusa MK3s 3D printer was acquired with its printing capabilities tested on several standard demo PLA prints to ensure the print head can move with the expected resolution in the X, Y, and Z directions. Standard benchmark tests and tuning for the printing platform can be found here and here [? ?].

FIGURE 7.7: MK3s print head. Left: Original print head assembly. Right: Dismantled print head assembly [**?**].

Next the print head of the MK3s was dismantled, as shown in Figure 7.7, leaving a flat surface to attach first the PINDA adapter [PR8] and the loadcell bracket [PR9], as shown in Figure 7.8. Use M3 bolts to attach the loadcell bracket and PINDA adapter to the dismantled print head surface. See read the printer assembly manual for more detail on the part assembly[**?**]. Bolt the TAL220 10 kg loadcell [E3] onto the loadcell bracket using M5 bolts [HW4]. Bolt the force applicator head [PR5-7, HW5] onto the other end of the loadcell using M4 bolts [HW3]. A range of force applicator heads shapes and sizes have been created to test the resolution of the sensor.

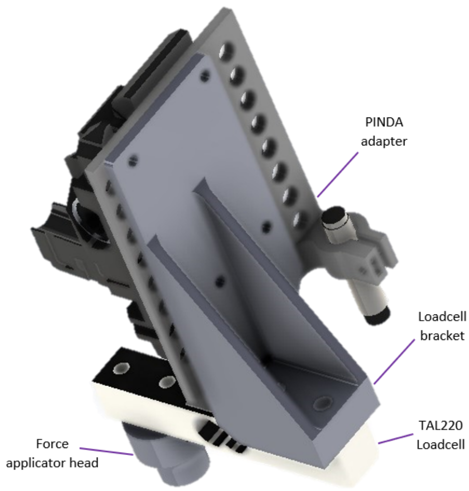

FIGURE 7.8: Force applicator head assembly.

With the thermistor from the original printhead no longer required, a trimpot [RV1] is attached to the thermistor port on the printer's control circuit PCBA[**?**]. While the 3D printer is turned on, the trimpot is manually adjusted until room temperature is reached on the 3D printer display to avoid any future under/over temperature errors.

The print bed of the MK3s 3D printer is removed and replaced with a mount tray [LC1] for the sensing domain. The ERT tray bearing part [PR10] mounted and bolted [HW6] onto the frame of the MK3s as shown in Figure 7.9. The ERT sensor tray [LC2] and the sensing domain mount tray are fixed together onto the print bed with two M3 bolts [HW6] clamping the trays to the edge of the print bed.

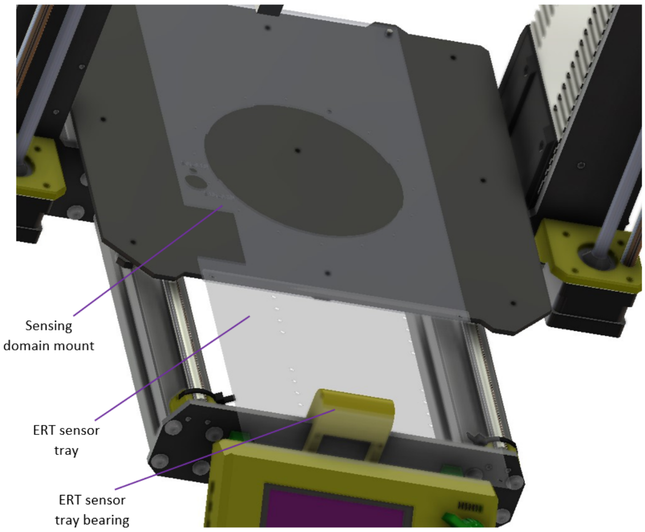

FIGURE 7.9: MK3s with original print bed tray removed and the ERT sensor trays added.

The firmware version used in this work was MK3s 3.9.0. Later versions may be compatible. Other 3D printer platforms with a similar gcode command set and a similar core firmware such as the Marlin firmware may also be used as a CFA. However, minor configuration changes in this work's software and hardware may be required.

7.7 Design Decisions

This section outlines and justifies some of the important design decisions made for both the ERT sensor and the CFA device.

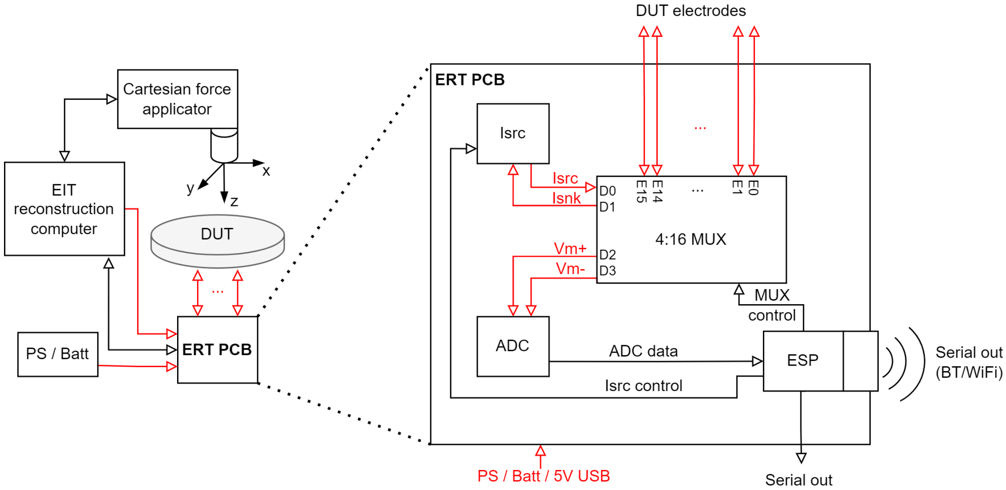

FIGURE 7.10: System architecture of ERT sensor and CFA setup (left) and the key internal electrical signals of the ERT circuit (right). With analogue/power signals shown with red arrows and digital signals with black arrows.

7.7.1 EIT cycle and load sequence

While a sequence of compressive loads are applied by the CFA to the sensing domain, concurrently the ERT sensor circuit gathers data for EIT reconstruction. This cyclic EIT data capture process follows a specific sequence,

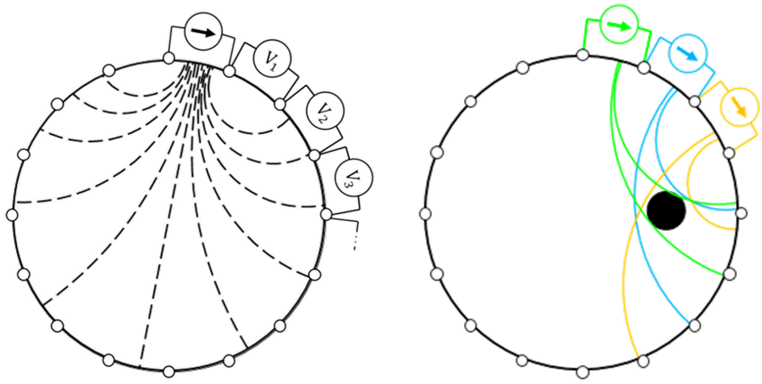

FIGURE 7.11: EIT adjacent drive pattern sequence.

1. A constant current is applied at adjacent electrode positions E_i and E_{i+1}, these electrode positions are selected with the 'MUX control' line.
2. Sequentially 16 adjacent electrode voltage measurements are completed next, again the electrode positions are selected with the 'MUX control' line.
3. Each raw voltage measurement is transmitted through 'serial out' to an 'EIT reconstruction computer'.
4. The next current injection electrode position is selected, i.e. i = i + 1. Once all 16 current injection positions are completed, 256 voltages are measured giving enough data for one reconstruction frame. This is repeated for the duration of the experiment.

Multiplexing of the voltage measurements was chosen instead of the alternative option of simultaneous voltage measurement, to maintain a low-cost circuit. The simultaneous voltage measurement solution involves 16 separate ADCs, one for each electrode. A DC current source was chosen instead of the AC alternative because the sensing domains do not show significant changes in reactance during loading events.

7.7.2 Small signal measurement

The range of voltages required for recreating minute changes in resistances of a sensing domain spans several orders of magnitudes. Therefore a high dynamic range, high resolution, low-noise voltage measurement system is required to capture this data.

To evaluate the performance of the system with a standardised testing domain a resistor mesh network was created. The mesh network was created to validate the expected resolution required for generating EIT reconstructions [20] for a variety of different resistances and resistance changes. The resistor mesh network provided a standardised platform with known resistor values and tolerances for the comparison a real and simulated resistor mesh network. The resistor mesh network was chosen to provide a range EIT voltage data comparable to that of the real CBSR composite material.

A script was created to form a square resistor mesh network of various dimensions and various background resistance values. PySpice circuit simulator [**?**] was used to run a zero noise simulation on the system to show the expected difference in raw ERT voltage data between a homogeneous resistor mesh and a resistor mesh with an anomalous blob as shown in Figure 7.12. The maximum and minimum ΔV_{read} values shown in Figure 7.12 and 94.994 mV and 53 μV respectively.

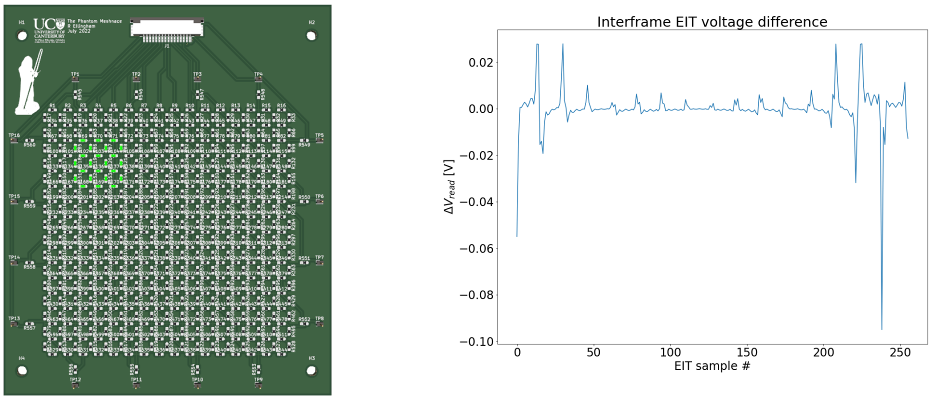

Figure 7.12: Left: A resistor mesh network for validating the ERT circuit, with the anomaly shown highlighted in green. Right: The difference between EIT raw voltage data from a homogeneous square 2.2 kΩ resistor mesh domain and the same domain with a 3.3 kΩ resistor mesh anomaly.

It is non-trivial to determine the exact resolution required for an EIT based pressure mapping sensor voltage measurements as it depends on the inherent noise of the domain, the force resolution required, the expected external noise, the drive current, the EIT reconstruction algorithm used, amongst other factors. This work uses a 24 bit ADC [U12] so that given an ideal noiseless representative domain the minimum voltage data shown in Figure 7.12 will be an order of magnitude larger than the resolution of the ADC.

7.7.3 Signal generation

The current source can drive a current, I_{src} between 15 μA and 50 mA and can be set as a programmable or fixed current source value. The I_{src} value can be altered by changing the R_{Isrc} [R7 or R8] value as shown in Equation 7.2.

$$I_{src} = \frac{0.617}{R_{Isrc}} + 15\mu A \tag{7.2}$$

If a fixed current source is desired for the ERT circuit R_{Isrc} sets the current source value based on Equation 7.2. If the circuit is configured as a programmable current source, the digital potentiometer [U9] controlling the R_{Isrc} value will a multiple of 39 Ω up to a maximum of 10 kΩ or a high impedance state. The possible programmable current source values are given in the `isrc_lookup.xlsx` file in the repository. If the resistivity of the domain is too high the current source supply will saturate to Vs. Ensure the domain resistivity is sufficiently low for this current source saturation not to occur within its expected range of use. A sufficiently high current value must pass through the domain to ensure low noise readings throughout the boundary electrodes on the domain. This noise predominantly occurs due to electrostatic effects in sensing domains. To ensure this current can be driven for the sensor domain configuration given in this work, a supply voltage, $\pm V_s$, of ± 20 V should be used.

7.7.4 Signal conditioning

When using the recommended supply voltage of ± 20 V, an attenuation stage is required for the input into the ADC. This is done with an operational amplifier (opamp) voltage buffer-divider-buffer circuit as shown in Figure 7.13. When using a single ended 5 V supply to drive the current source this opamp circuit can be bypassed using the jumpers shown in Figure 7.18 as the attenuation is not required and the offset and noise due to the opamp circuit can be avoided. However due to a lack of a negative Vss, the multiplexer channel resistance will be degraded as exemplified in Figure 7.15.

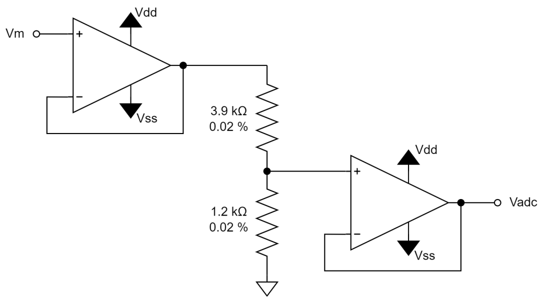

FIGURE 7.13: Measurement attenuation circuit

To allow larger current signals to be driven through the domain a maximum voltage driving the current source of 20 V is used with an attenuation circuit consisting of two voltage buffers and a voltage divider. The attenuation circuit steps down the voltage with a nominal gain of $0.24 \pm 3\%$. The attenuation circuit is duplicated for both differential ADC inputs. This circuit is highly sensitive to any noise, DC offset, or component variation. To combat the sensitivity of this circuit the opamps used [U10, U11] have a low input bias current, and low input DC offset voltage, the resistors used have a low tolerance of $\pm 0.02\%$.

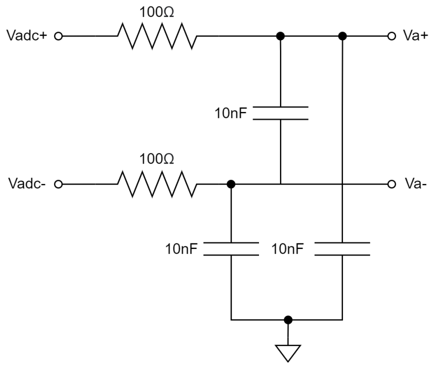

FIGURE 7.14: Passive low-pass filter circuit

A passive low-pass filter has been placed between the opamp circuit and the ADC input to attenuate ADC input noise. The cutoff frequency for this filter has been set to a value of, 1 MHz allowing for sufficient settling time for the maximum potential ADC sample rate of 512 kSPS.

7.7.5 Switching circuit

A 4:16 multiplexing circuit allows for a range of EIT switching drive patterns for ERT data acquisition. Previous research has shown the trade-offs with different EIT drive patterns [181, 235, 236]. A multiplexer with a low drain-source on-resistance characteristic for smaller drain voltages has been chosen as the majority of the voltage readings being read through the multiplexer will be nearer to zero than ±Vs.

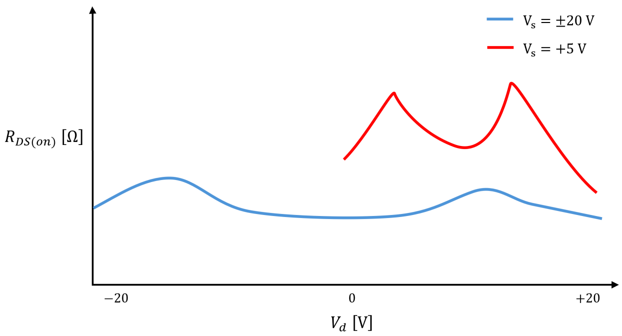

FIGURE 7.15: $R_{DS(on)}$ characteristic diagram for a typical multiplexer analogue channel for a dual and single-ended power supply.
[**?**].

Any variation in the $R_{DS(on)}$ value as a function of V_D or from channel-to-channel will add to the offset noise read by the ADC lowering the resolution of the ERT pressure sensor. This low $R_{DS(on)}$ variation can be seen in Figure 7.15. The multiplexer used can switch analogue voltage up to ±22 V with a switching time of 200 ns [**?**].

7.7.6 Force measurement

The CFA system is designed to be used with soft piezoresistive sensing domains due to loading limitations of the 3D printer frame and the force applicator head design. The force applicator head must be significantly more rigid than the sensing domain being tested to ensure low strain error.

A static load FEA simulation was completed on the loadcell bracket [PR9] with the maximum load expected used as 100N. The material of the bracket was PLA with orthotropic material properties. The static simulation used the orthotropic 3D printed PLA properties given by Sosa-Vivas et al. [**?**] with Caculix FEM solver [**?**]. As shown in Figure 7.16 the maximum predicted displacement of an FEM element within the loadcell part was 0.13 mm. If using a sufficiently soft domain and small force applicator this maximum displacement has little effect on the data processed, however this may cause significant error within harder domains and/or larger force applicators. Although the device can operate at 100 N, device operation is recommended below 50 N to decrease the strain error due to force applicator deformation.

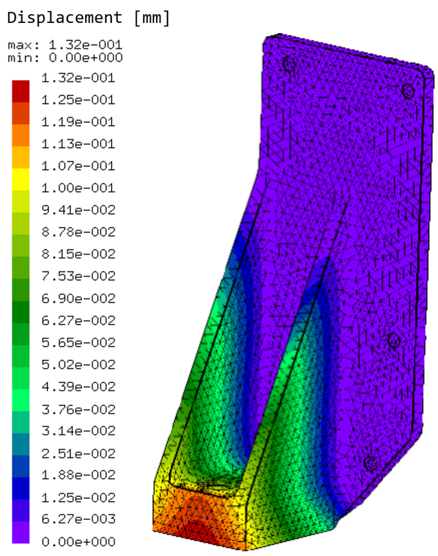

FIGURE 7.16: Static load analysis of the loadcell bracket part [PR9] of maximum allowable load of 100 N showing the magnitude of displacement.

The TAL220 loadcell used was chosen for the sensing domain material. The CBSR material had an elastic modulus of 100 kPa[21] so that range of strain measurements from 0 - 50% could be accurately recorded with the given loadcell. The minimum force is on the limit of what can be detected as the TAL220 is rated for ±50 mN resolution [**?**] across its operating load and temperature range. However the noise of the loadcell was measured to be ± 2.5 mN during several 15 minute experiments in a 22±0.7°C regulated room. Examples of experiment loading limits are given in Table 7.3, giving the extreme cases for testing minimum and maximum theoretical strain for 5 and 20 mm diameter force applicator heads on a lower and higher elastic modulus material respectively.

Table 7.3: An example of the extreme parameters of two loading experiments showing the minimum and maximum strains limits for 5 mm and 20 mm diameter force applicators and their required forces respectively.

Force [N]	**Force applicator diameter [mm]**	**Force applicator area [mm^2]**	**domain elastic modulus [kPa]**	**Theoretical strain [%]**	**Theo stres**
0.06	5	19.6	60	5.1	3.1
50.00	20	314.2	200	79.6	159.2

7.7.7 Position control and measurement

The Prusa MK3s 3D printer was used because of it's proven reliability as a 3D printer to move in x, y, and z axes with high resolution. The resolution of the force applicator location under without applying a load is 0.01 mm in each axis. Due to the open-loop nature of control of the stepper motors the resolution at high loads may not be reliable.

7.7.8 Sensing domain

The weight percentage of CB powder in an elastomer matrix, such as silicone rubber, to maintain desired mechanical and electrical properties can be tuned as shown in the characterisations completed by D'Asaro et al and Shang et al [186, 187]. The most desirable piezoresistive characteristics found in these works are near the inflection point of the conductivity versus CB weight percentage plot.

Because of the difference in fabrication processes and degree of dispersion generating variability in the percolation, an iterative trial and error approach using the starting point found in literature was used to get 8 wt % and 9 wt % values for CB in SR [186, 187]. Within this range the material was sufficiently conductive while maintaining mechanical strength through sufficient elastomeric cross-linking. Previous research indicates that there is a weight percentage at which the gauge-factor/piezoresistivity is at a maximum within a similar range used in this work [188, 189]. The CB particle dispersion can vary throughout a domain depending on various factors in the fabrication process including mixing technique, solvents used, silicone viscosity, particle size, particle agglomerations, amongst other factors [153, 237**?** , 238]. Dispersion of carbon black particles was ensured by using a relatively low viscosity silicone of 6,000 mPa.s and a centrifugal planetary mixer a method proven to give better dispersion than other traditional mixing techniques [**?**].

7.8 Operation instructions

To validate and characterise the ERT pressure mapping sensor the CFA is used to apply a sequence of loads to the material. The below sequence of required operations to complete this experiment includes:

1. ERT sensor power modes
2. ERT sensor programming

3. ERT sensing domain preparation
4. Load application point and strain configuration
5. Touch based mesh bed leveling
6. Load experiment execution
7. Data capture
8. Data processing

This sequence of events is repeated for different sensing domains and different loading conditions.

7.8.1 ERT sensor power modes

Before running any experiments, the ERT sensor power mode must be configured. The jumper configuration for the bipolar supply (blue) and +5 V USB single-ended supply (red) mode is shown in Figure 7.18.

The bipolar supply first mode is recommended for driving the ERT signal through a wider range of sensing domains at a higher voltage. A bipolar supply of ±20 V is connected to $\pm V_s$ for the best performance of the circuit.

The second power mode uses a +5 V USB 3.X power supply to run the ERT circuit. The second mode is limited to lower resistance sensing domains that can be tested as it can only drive constant currents using +5 V. When using the +5 V supply mode the $-V_s$ and GND pins on the power input must be shorted for the multiplexers to operate.

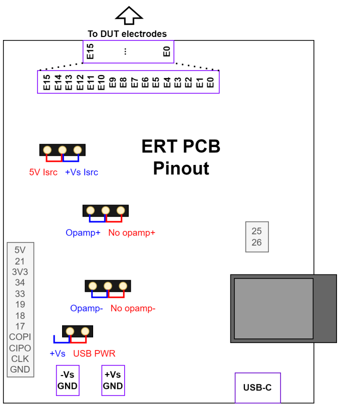

FIGURE 7.17: ERT PCB pin-out and power mode options. Blue jumpers are for the bipolar supply mode (i.e. $\pm V_s$ attached). Red jumpers are for the +5 V USB supply mode.

For each power mode there will be a distortion of the signal dependent on the power supply voltages and input signal as exemplified in Figure 7.15.

7.8.2 ERT sensor programming

The ERT sensor contains an ESP-WROOM32 module [U1] which requires the `main_ert.c` program to be built and flashed. This can be achieved using the default project template from the ESP-IDF environment[?]. The default ERT circuit firmware `main_ert` completes the well proven adjacent electrode drive pattern [236, 239? ?]. Upon successful programming of the ERT circuit it will output a constant serial stream of the adjacent electrode pattern ERT data separating each frame of 256 measurements with an '`A`'. The ERT sensor circuit has the capability to send the real-time serial ERT data via a USB serial, Bluetooth, or WiFi connection to a EIT reconstruction capable computer.

7.8.3 ERT sensing domain preparation

For sensing domain fabrication instructions refer to Section 7.6.2. The ERT sensing domain needs to have sufficiently low adjacent inter-electrode resistance to function, so that the current source will not saturate due the power supply voltage. The ET electrodes can be attached to the domain in many ways as shown in Figure 7.6, ensure these connections provide a reliable electrical contact to the sensing domain. Connect sensing domain electrodes to the ERT circuit FPC connector[W1] via an adapter[J8]. The ERT sensing domain must be flat and centered on the sensing domain holder [PR3, PR4] as shown in Figure 7.6 (middle).

7.8.4 Load application point and strain configuration

Load application points and strains applied to the sensing domain can be configured by altering variables in `ertpcb_cfa_reader.py` code. A loading sequence consists of a series of load applications, in the form of a strain pulse train, applied to a set of X and Y coordinates on the sensing domain. The main parameters to change for running a loading sequence are given in Table 7.4.

TABLE 7.4: Experimental parameters.

to X[0.5,1] X[0.1,1] X

Variable:	**Unit:**	**Description:**
Strain speed (`v_z_push`)	mm/min	The rising/falling edge gradient for each pulse.
Strain limit (`strain_limit`)	%	The maximum compressive strain allowed.
Load locations (`push_points`)	[mm, mm]	An array of XY locations of each load pulse.
Reference offset (`ref_loc_mm`)	[mm, mm]	The XY offset of the zero point of the sensing domain relative to the CFA home reference.

These can all be found as variables in the software file `ertpcb_cfa_reader.py` within the `main` function. Before running this program the serial COM ports may need to be changed in the `ertpcb_cfa_reader.py` program to match the comports of the CFA and ERT sensor hardware.

7.8.5 Load experiment execution

Once all hard-coded parameters have been set the command parameters are set and the load experiment begins. To begin the load experiment use the following terminal command:

```
>> python ertpcb_cfa_reader.py <dir/filename> <Isrc_A> <Vmax> <sample_name> <date_fab
<load_time_s> <strain>
```

Where `<dir/filename>` is includes the file directory and file name, `<Isrc_A>` is the constant current source value set in the ERT circuit in amps, `<Vmax>` is the maximum allowed voltage to be read by the ADC in volts (e.g. 20 V), `<sample_name>` is a descriptive sensing domain name, `<date_fabricated>` is the sample fabrication date ('NA' or leave blank if irrelevant), `<load_time_s>` is the strain pulse on and off time in seconds, and `<strain>` is the desired strain applied to the domain as a percentage. If a random test sequence is desired with randomised strain and locations this can be achieved by simply setting the `<strain>` value to -1.

7.8.6 Touch-based mesh bed leveling

An undulating sensing domain surface can often be present during testing due to an intentionally curved sensor or manufacturing defects. To compensate for an uneven surface a touch-based mesh bed leveling process has been created to improve the quality of the stress/strain data gathered. The process involves the force applicator head travelling towards the sample until a change in force has been detected above 0.1 N. This mitigates the risk of any misalignment with the force applicator surface plane and the sensing domain surface plane and ensures more accurate strain data capture for low strain magnitudes. This touch-based mesh bed leveling is completed before the load sequence experiment begins. The sensing domain and holding trays should not be physically contacted in any form after beginning the `ertpcb_cfa_reader.py` program.

7.8.7 Data capture

Once the `ertpcb_cfa_reader.py` program has completed capturing data, a time-series plot of the 16 inter-electrode resistances, R_{int}, will appear. A stable R_{int} is for stable EIT reconstructions of the sensing domain.

Any significant change in the inter-electrode resistance may cause a poor EIT reconstruction result. A significant change in the inter-electrode resistance could be a result of, applying force too close to the electrodes themselves, an inherently unstable electrode connection, or an external force applied near the electrode. If the R_{int} values are not stable it will be evident in the plot and there will be a warning message in the console.

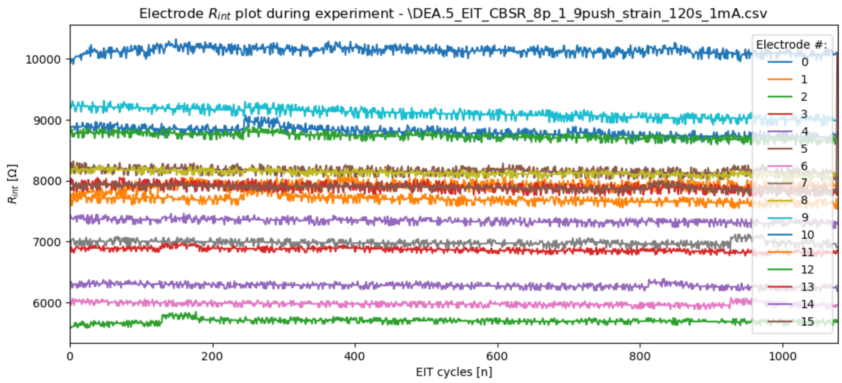

FIGURE 7.18: An example plot of the R_{int} values generated on completion of an experiment for a stable experiment. Where the Electrode # 'i' represents the resistance between electrode 'i' and 'i+1'.

Once the inter-electrode resistance plot is closed the program will continue to save all of the data in three separate files for the given `filename`,

1. *filename*.csv - Time series data for ERT voltages, compression forces, and force applicator XYZ locations. The UTC start date and time of the experiment is given in the top row.
2. *filename*.pkl - Logs the same data as the .csv file **and** all of the important experiment parameters into a serialised python 'pickle' file.
3. *filename*.gcode - The gcode file of the commands sent to the 3D printer platform for the experiment run.

7.8.8 Data processing

Once all of the data has been collected in the above steps, the data can be processed. Data processing includes the following,

1. Pre-processing of the raw voltage, force, and position data. Filtering and data cleaning could be included in this step.
2. Image reconstruction using a chosen EIT algorithm with the pre-processing or raw data. EIT reconstruction could include algorithms such as regularised Newton's methods [**?**], neural network based methods [183, 240], and back projection methods [**?**].
3. Any post-processing of the EIT image reconstruction data and integration with the force applicator stress and/or strain data. Post-processing could include resistance to force inverse modelling, pressure mapping performance metric quantification, an application specific software interface.

In this work EIDORS [241] has been used to complete the EIT reconstructions of the domain and any post processing is then completed with a python program as shown in Section 7.10.

7.9 Construction and Operational Safety

Various safety concerns must be stated for the construction and operation precautions of this system. This is not a comprehensive safety guide, but will give an overview of some potential safety concerns. Other precautions may be necessary depending on the development location and sensing domain materials used. The construction and operation of the system can each be separated into three parts, the ERT sensor circuit, the CFA, and the sensing domain.

7.9.1 Construction

During the assembly of the ERT sensor circuit the regular health and safety procedures for assembling and soldering a PCB must be followed.

During testing of the CFA as a 3D printer there will be moving parts which could get caught on long hair or collide with a person too close. Steps must be taken to avoid any undesired collisions or any people touching the CFA during operation.

When fabricating the sensing domain often this involves micro/nano sized conductive particles dangerous for inhalation and sometimes dangerous to touch. The material safety datasheet must be consulted for any material used in the sensing domain. Any safety procedures with mixing machines and curing devices must be followed.

7.9.2 Operation

The PCBA can operate on up to ± 20 VDC which is within the safe level the SELV as defined by IEC [**?**]. However, should the contacts of the power supply to the ERT circuit be electrically shorted, a burn or fire hazard may arise. The current on the sensing domain electrodes is limited to prevent a dangerous short circuit current.

During the operation of the CFA there will be moving parts which could collide tangle long hair or collide with the person operating. Steps must be taken to avoid any undesired collisions or any people touching the CFA during operation.

The sensing domain may not be bio-compatible so the material safety datasheet(s) for each domain must be followed for each real world sensor application.

7.10 Validation and characterisation

To show that the system is functional, the plots produced from an EIT reconstruction of the voltage data and the force measurements can be compared for a correlation. Examples are given below in Figure 7.19 and 7.20, showing localised blobs at the known locations of the force applicator.

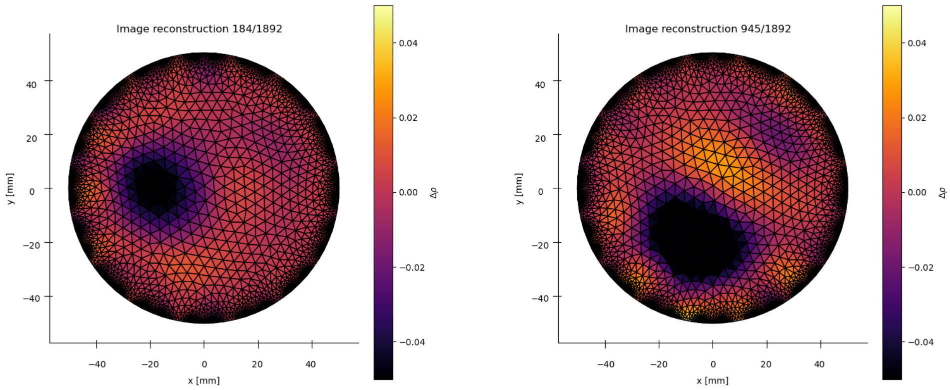

FIGURE 7.19: Reconstruction frames from a random push test sequence on a 1mm thick 100mm diameter sample. Strain and applied locations (x, y) [mm] - Left: 24% (-14.8, -3.4). Right: 36% (-1.9, -21.3)

A raw video of this experiment can be seen in the `/examples` folder. It can be useful to plot the force profile being applied alongside the EIT reconstruction to verify the data is ready for further processing and modelling.

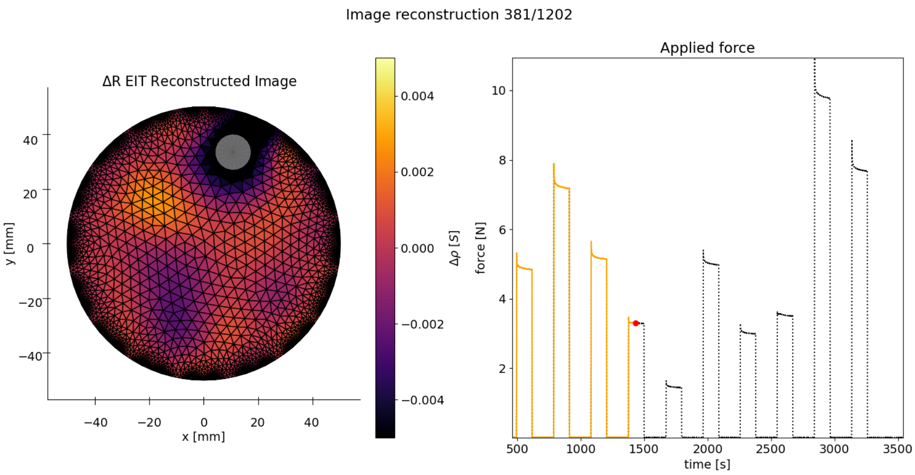

FIGURE 7.20: Reconstruction frames from a random push test sequence on a CBSR 100mm diameter sample. The white circle representing the force applicator location and the red dot on the force plot showing the captured frame in time.

7.10.1 Sensor capabilities

Simultaneous application of multiple loads can be achieved with this system using a multi-head force applicator. It has been shown that multiple touch points can be detected as shown in Figure 7.21 the supplementary material and in our previous work [20].

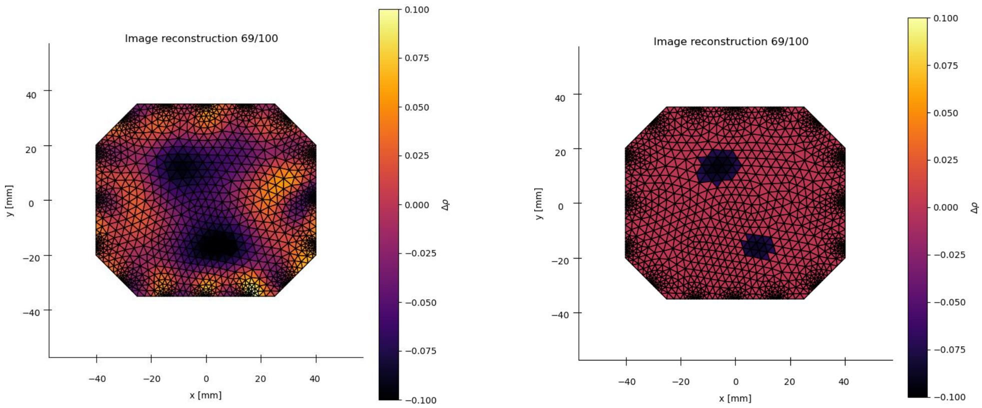

FIGURE 7.21: An EIT reconstruction image of a sensing domain with two loads applied simultaneously. Left: Without threshold filtering. Right: With a 75% threshold amplitude filter applied.

A major factor constraining the application of EIT-based sensors is the poor frequency response of the material, which limits the detection of rapid successive loads. The system given in this work allows further research into characterising the transient response of a range of sensing domains in 2D. Examples of how transients have been characterised are shown in Figure 7.22

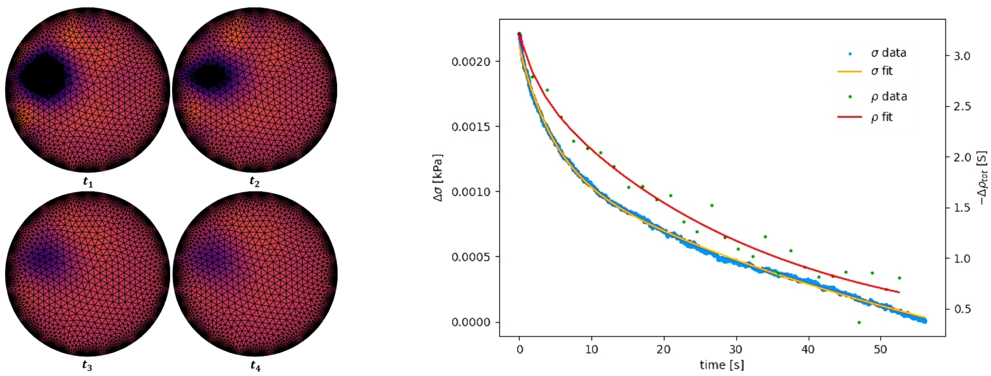

FIGURE 7.22: Left: Example sequence a resistive relaxation after a loading event at times t_1 to t_4. Right: Example stress, σ, and resistive, ρ, relaxation plot generated from an ERT CFA experiment given a 30% strain step input [21].

The piezoresistivity of a sensing domain can often vary throughout its volume giving unpredictable results if a homogeneous domain is assumed for the pressure mapping sensor. This system can be used to generate map of the piezoresistivity function of a material surface in 2D dimensions.

7.11 Conclusions

This work has provided the methods and tools to enable further research and development for soft EIT-based pressure sensing systems. The system is low cost, simple to construct, and easy to use. The automation of compression load experiments ensures that experiments are repeatable with quantifiable results and mitigating human error.

The automated nature of the CFA device significantly reduces the time to complete a set of experiments and can provide experiment sequences similar to those expected during the real-world application of the sensor. Upon load experiment completion, the system provides clearly formatted raw data files ready for analysis.

Uses of this system vary from 2D piezoresistive material analysis and pressure mapping sensor characterisation. Extensive research has been conducted into one-dimensional (1D) characterisation of piezoresistive materials. However, the characterisation of these materials in two dimensions (2D) has often been overlooked in past literature [187, 191, 242, 243], often due to the complex and invasive methods required. The device can be used to characterise the electromechanical/piezoresistive properties of a soft thick film material in 2D, quantify EIT reconstruction performance, and generate models predicting localised loads from localised resistance changes.

To push the field of EIT-based pressure mapping forward tools are required to standardise testing and reliably acquire quantifiable data for pressure modelling in different sensing domain materials. A toolbox of hardware and software have been described in this work to make EIT-based pressure mapping realisable for more real-world applications.

Proposed future enhancements of the system include minimising noise and offsets in the signal conditioning ERT circuit, adding an auto-calibration procedure to ensure the ADC and I_{src} circuits operate at the expected resolution, and reducing the PCB size. The ERT sensor and Cartesian force applicator system described in this work will help transition this technology into real-world applications.

7.12 Future Work

The integration of DEA and EIT in a portable package would open a range of applications. To integrate this portable EIT system into the DEA-EIT device mentioned in Chapters 6 and 7, a DEA driver expansion board would be required. This would give an DEA-EIT device could have the capability of contracting and acquiring EIT voltage data for pressure mapping while maintaining a small form factor. A draft design of the DEA PCBA mounted on the portable EIT PCBA can be seen in Figure 7.23.

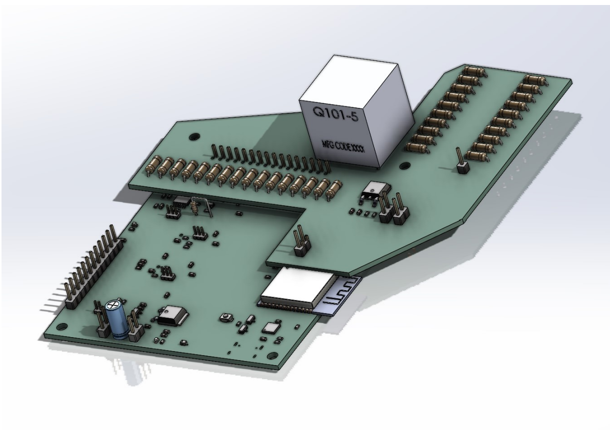

FIGURE 7.23: Render of a DEA daughter board mounted on this work's portable ERT board.

Chapter 8

?? Modelling of DEA-EIT Capacitively driven Hybird Sensing and Actuation Device

ABSTRACT

8.1 INTRODUCTION

Development of Electrical Impedance Tomography (EIT)-based pressure sensors have hit a brick wall in the past due to the time-dependent phenomena experienced by piezoresisitive materials making them difficult to model and limiting the resistivity of such a pressure mapping sensor. This work investigates adding capacitive functionality to EIT-based pressure mapping by using a dielectric elastomer (DE) to aid capacitively shunt current so that not just the resistance of the device changes but also the capacitance. The hypothesis is that the non-linear time dependent effects of resistive sensing will be mitigated using this capacitive shunting.

As described in previous works [21] there have been various attempts at created EIT-based pressure sensing devices. However, all of the state-of-the-art sensors rely on the change of resistance for pressure mapping []. Zhang et. al [244] utilised capacitive shunting for EIT touch mapping on a variety of surfaces with conductive coatings. Their work used a human touch input to shunt electrical current through the person's contact point, essentially mapping localised changes in capacitance. Work from Reynolds Smith [**? ?**] pioneered the bifurcation of EIT and Electric Field Tomography (EFT). In this work the benefits and limitations of such a technology is explored.

The lack of control over the object being shunted through makes pressure mapping estimates non-trivial.

To create a sensing domain that can map loads and estimate the corresponding pressure using this shunting phenomena three main components have been used. A conductive particle elastomer composite (CPEC) top layer, an insulating dielectric elastomer (DE) middle layer, and a grounded conductive bottom layer, as shown in Figure **??**. The top layer has 16 boundary electrodes connected for use with EIT drive circuitry. The bottom layer is connected to the EIT drive circuitry's ground via a singular electrode. This bottom surface will be used to shunt the current capacitively, with localised changes in capacitance due to loading causing localised changes in shunting of current.

This work investigates whether the EIT drive frequency can be optimised for an EIT-based pressure sensor with range of DE shapes and thicknesses.

8.2 METHOD

8.3 RESULTS

8.4 DISCUSSION

8.5 CONCLUSIONS

Chapter 9

The Biomimmetic Re-Evolution

9.1 Introduction

Bibliography

[1] Meejin Kim and Sukwon Lee. Fusion poser: 3d human pose estimation using sparse imus and head trackers in real time. *Sensors*, 22:4846, 6 2022. ISSN 1424-8220. doi: 10.3390/S22134846. URL https://www.mdpi.com/1424-8220/22/13/4846/htmhttps://www.mdpi.com/1424-8220/22/13/4846.

[2] Ryo Eguchi, Brendan Michael, Matthew Howard, and Masaki Takahashi. Shift-adaptive estimation of joint angle using instrumented brace with two stretch sensors based on gaussian mixture models. *IEEE Robotics and Automation Letters*, 5:5881–5888, 10 2020. ISSN 23773766. doi: 10.1109/LRA.2020.3010486.

[3] Ben O'Brien, Todd Gisby, and Iain A. Anderson. Stretch sensors for human body motion. volume 9056, pages 254–262. SPIE, 3 2014. ISBN 9780819499820. doi: 10.1117/12.2046143. URL https://www.spiedigitallibrary.org/conference-proceedings-of-spie/9056/905618/Stretch-sensors-for-human-body-motion/10.1117/12.2046143.full.

[4] Logan Thomas Chatfield. A hybrid assist-as-need elbow exoskeleton for stroke rehabilitation. 2021. doi: 10.26021/11321. URL https://hdl.handle.net/10092/102273.

[5] XSENSOR. Xsensor — wheelchair seating. URL https://www.xsensor.com/solutions-and-platform/csm/wheelchair-seating.

[6] PressureProfile. Tactile sensors for robotic applications — pps, 2023. URL https://pressureprofile.com/robotics.

[7] PowerOn. Poweron: Update of the "super sensitive" - robotik-insider.de. URL https://mrk-blog.de/en/PowerON-Update-of-the-super-sensitive/.

[8] Tekscan. Thin-film pressure sensors — tekscan. URL https://www.tekscan.com/thin-film-pressure-sensors?utm_source=google&utm_medium=cpc&utm_term=pressure+sensors&utm_content=eta7&utm_campaign=pressure&gad_source=1&gclid=CjwKCAiApuCrBhAuEiwA8VJ6Jt-4kVuEinAM6-jd72DwnWxvPCQus_Md7xr2i_bDOsIWg7SK7aw6nRoCuk0QAvD_BwE.

[9] SensorProducts. Tactilus — compression force sensing resistor (fsr) — force sensing resistors — force sensing resistors — tactilus — surface pressure indicator — mapping — force sensing and profiling. URL https://www.sensorprod.com/tactilus.php.

[10] David Richfield. Medical gallery of david richfield. *Wiki Journal of Medicine*, 1:9, 2014. doi: https://doi.org/10.15347/wjm/2014.

009. URL https://en.wikiversity.org/wiki/WikiJournal_of_Medicine/Medical_gallery_of_David_Richfield_2014.

[11] Dr. Andreo A Spina. Muscle — functional anatomy seminars, 2014. URL https://functionalanatomyblog.com/2014/06/12/muscle/.

[12] Joseph Teran, Silvia Blemker, Victor Ng-Thow-Hing, and R. Fedkiw. Finite volume methods for the simulation of skeletal muscle. pages 68–74, June 2003.

[13] Edith M. Arnold, Samuel R. Ward, Richard L. Lieber, and Scott L. Delp. A model of the lower limb for analysis of human movement. *Annals of biomedical engineering*, 38(19957039):269–279, February 2010. ISSN 0090-6964. URL https://www.ncbi.nlm.nih.gov/pmc/articles/PMC2903973/.

[14] Tadej Bajd and Marko Munih. Basic functional electrical stimulation (fes) of extremities: an engineer's view. *Technology and health care : official journal of the European Society for Engineering and Medicine*, 18:361–9, 2010.

[15] Wang Yanjie and Takushi Sugino. Ionic polymer actuators: Principle, fabrication and applications. July 2018.

[16] Nicholas Kellaris, Vidyacharan Gopaluni Venkata, Garrett M. Smith, Shane K. Mitchell, and Christoph Keplinger. Peano-hasel actuators: Muscle-mimetic, electrohydraulic transducers that linearly contract on activation. *Science Robotics*, 3(14):3276, 1 2018. ISSN 24709476. doi: 10.1126/scirobotics.aar3276. URL http://robotics.sciencemag.org/. ¡br/¿.

[17] Yu-Jin Park, Seong Hwan Kim, Tae-Hoon Lee, Ae-Ri Cha, Gi-Woo Kim, and Seung-Bok Choi. Design analysis of a magnetorheological elastomer based bush mechanism. volume 10595, March 2018. URL https://doi.org/10.1117/12.2318795.

[18] Ron Pelrine, Roy Kornbluh, Qibing Pei, and Jose Joseph. High-speed electrically actuated elastomers with strain greater than 100 *Science*, 287(5454):836–839, 2 2000. ISSN 00368075. doi: 10.1126/science.287.5454.836. URL http://science.sciencemag.org/content/287/5454/836.abstract.

[19] Y.C. Fung. *Biomechanics - Mechanical Properties of Living Tissues*. Springer Verlag, second edition, 1993. ISBN 0-387-97947-6. Pg 568.

[20] Richard Ellingham and Tim Giffney. Carbon black silicone piezoresistive electrical impedance tomography stress sensor device. volume 12042, pages 207–214. SPIE, 4 2022. doi: 10.1117/12.2610694. URL https://doi.org/10.1117/12.2610694.

[21] Richie Ellingham, Chris Pretty, Lui Holder-Pearson, Kean Aw, and Tim Giffney. An electrical impedance tomography based artificial soft skin pressure sensor: Characterisation and force modelling. *Sensors and Actuators A: Physical*, 373:115427, 2024. ISSN 0924-4247. doi: https://doi.org/10.1016/j.sna.2024.115427. URL https://www.sciencedirect.com/science/article/pii/S0924424724004217.

[22] Yann Roudaut, Aurélie Lonigro, Bertrand Coste, Jizhe Hao, Patrick Delmas, and Marcel Crest. Touch sense: functional organization and molecular determinants of mechanosensitive receptors. *Channels (Austin,*

Tex.), 6:234–245, 7 2012. ISSN 1933-6950. doi: 10.4161/CHAN.22213. URL https://www.ncbi.nlm.nih.gov/pmc/articles/pmid/23146937/?tool=EBIhttps://europepmc.org/article/pmc/3508902.

[23] Francesco Stella and Josie Hughes. The science of soft robot design: A review of motivations, methods and enabling technologies. *Frontiers in Robotics and AI*, 9: 1059026, 1 2023. ISSN 22969144. doi: 10.3389/FROBT.2022.1059026/BIBTEX.

[24] Yongchang Zhang, Pengchun Li, Jiale Quan, Longqiu Li, Guangyu Zhang, and Dekai Zhou. Progress, challenges, and prospects of soft robotics for space applications. *Advanced Intelligent Systems*, 5:2200071, 3 2023. ISSN 2640-4567. doi: 10.1002/AISY.202200071. URL https://onlinelibrary.wiley.com/doi/full/10.1002/aisy.202200071https://onlinelibrary.wiley.com/doi/abs/10.1002/aisy.202200071https://onlinelibrary.wiley.com/doi/10.1002/aisy.202200071.

[25] Florian Hartmann, Melanie Baumgartner, Martin Kaltenbrunner, F Hartmann, M Baumgartner, and M Kaltenbrunner. Becoming sustainable, the new frontier in soft robotics. *Advanced Materials*, 33:2004413, 5 2021. ISSN 1521-4095. doi: 10.1002/ADMA.202004413. URL https://onlinelibrary.wiley.com/doi/full/10.1002/adma.202004413https://onlinelibrary.wiley.com/doi/abs/10.1002/adma.202004413https://onlinelibrary.wiley.com/doi/10.1002/adma.202004413.

[26] Oncay Yasa, Yasunori Toshimitsu, Mike Y. Michelis, Lewis S. Jones, Miriam Filippi, Thomas Buchner, and Robert K. Katzschmann. An overview of soft robotics. *Annual Review of Control, Robotics, and Autonomous Systems*, 6:1–29, 5 2023. ISSN 25735144. doi: 10.1146/ANNUREV-CONTROL-062322-100607/CITE/REFWORKS. URL https://www.annualreviews.org/content/journals/10.1146/annurev-control-062322-100607.

[27] Mariangela Manti, Vito Cacucciolo, and Matteo Cianchetti. Stiffening in soft robotics: A review of the state of the art. *IEEE Robotics and Automation Magazine*, 23:93–106, 9 2016. ISSN 10709932. doi: 10.1109/MRA.2016.2582718.

[28] Chidanand Hegde, Jiangtao Su, Joel Ming Rui Tan, Ke He, Xiaodong Chen, and Shlomo Magdassi. Sensing in soft robotics. *ACS Nano*, 17:15277–15307, 8 2023. ISSN 1936086X. doi: 10.1021/ACSNANO.3C04089/ASSET/IMAGES/LARGE/NN3C04089_0013.JPEG. URL https://pubs.acs.org/doi/full/10.1021/acsnano.3c04089.

[29] Cosimo Della-Santina, Christian Duriez, and Daniela Rus. Model-based control of soft robots: A survey of the state of the art and open challenges. *IEEE Control Systems*, 43:30–65, 6 2023. ISSN 1941000X. doi: 10.1109/MCS.2023.3253419.

[30] Costanza Armanini, Frederic Boyer, Anup Teejo Mathew, Christian Duriez, and Federico Renda. Soft robots modeling: A structured overview. *IEEE Transactions on Robotics*, 6 2023. ISSN 19410468. doi: 10.1109/TRO.2022.3231360.

[31] S. Murugesan. An overview of electric motors for space applications. *IEEE Transactions on Industrial Electronics and Control Instrumentation*, IECI-28:260–265, 1981. ISSN 00189421. doi: 10.1109/TIECI.1981.351050.

[32] T. Ashuri, A. Armani, R. Jalilzadeh Hamidi, T. Reasnor, S. Ahmadi, and K. Iqbal. Biomedical soft robots: current status and perspective. *Biomedical engineering letters*, 10:369–385, 8 2020. ISSN 2093-985X. doi: 10.1007/S13534-020-00157-6. URL https://pubmed.ncbi.nlm.nih.gov/32864173/.

[33] F. Branz and A. Francesconi. Experimental evaluation of a dielectric elastomer robotic arm for space applications. *Acta Astronautica*, 133:324–333, 4 2017. ISSN 0094-5765. doi: 10.1016/J.ACTAASTRO.2016.11.007.

[34] Alessandro Bruschi, Davide Maria Donati, Peter Choong, Enrico Lucarelli, and Gordon Wallace. Dielectric elastomer actuators, neuromuscular interfaces, and foreign body response in artificial neuromuscular prostheses: A review of the literature for an in vivo application. *Advanced Healthcare Materials*, 10: 2100041, 7 2021. ISSN 2192-2659. doi: 10.1002/ADHM.202100041. URL https://onlinelibrary.wiley.com/doi/full/10.1002/adhm.202100041https://onlinelibrary.wiley.com/doi/abs/10.1002/adhm.202100041https://onlinelibrary.wiley.com/doi/10.1002/adhm.202100041.

[35] Todd A. Gisby, Benjamin M. Obrien, and Iain A. Anderson. Self sensing feedback for dielectric elastomer actuators. *Applied Physics Letters*, 102, 5 2013. ISSN 00036951. doi: 10.1063/1.4805352/26744. URL /aip/apl/article/102/19/193703/26744/Self-sensing-feedback-for-dielectric-elastomer.

[36] Samuel Rosset, Benjamin M. O'Brien, Todd Gisby, Daniel Xu, Herbert R. Shea, and Iain A. Anderson. Self-sensing dielectric elastomer actuators in closed-loop operation. *Smart Materials and Structures*, 22:104018, 9 2013. ISSN 0964-1726. doi: 10.1088/0964-1726/22/10/104018. URL https://iopscience.iop.org/article/10.1088/0964-1726/22/10/104018https://iopscience.iop.org/article/10.1088/0964-1726/22/10/104018/meta.

[37] Xiqiang Liu, Li Wang, Guidong Chen, al, Joseph W Lowdon, Kasper Eersels, Bart van Grinsven, G Rizzello, D Naso, A York, and S Seelecke. Closed loop control of dielectric elastomer actuators based on self-sensing displacement feedback. *Smart Materials and Structures*, 25:035034, 2 2016. ISSN 0964-1726. doi: 10.1088/0964-1726/25/3/035034. URL https://iopscience.iop.org/article/10.1088/0964-1726/25/3/035034https://iopscience.iop.org/article/10.1088/0964-1726/25/3/035034/meta.

[38] Weiyang Huang, Guozheng Kang, and Pengyu Ma. Uniaxial electro-mechanically coupled cyclic deformation of vhb 4905 dielectric elastomer: Experiment and constitutive model. *Journal of Materials Engineering and Performance*, pages 1–16, 4 2023. ISSN 15441024. doi: 10.1007/S11665-023-08179-8/FIGURES/17. URL https://link.springer.com/article/10.1007/s11665-023-08179-8.

[39] Wan Hasbullah MohdIsa, Andres Hunt, and S. Hassan HosseinNia. Sensing and self-sensing actuation methods for ionic polymer–metal composite (ipmc): A review. *Sensors 2019, Vol. 19, Page 3967*, 19:3967, 9 2019. ISSN 1424-8220. doi: 10.3390/S19183967. URL https://www.mdpi.com/1424-8220/19/18/3967/htmhttps://www.mdpi.com/1424-8220/19/18/3967.

[40] Guillaume Landry, Katia Parodi, Joachim E Wildberger, al, Mikaël Simard, Arthur Lalonde, Hugo Bouchard, Gurpreet Singh, and Arnab Chanda. Mechanical properties of whole-body soft human tissues: a review. *Biomedical Materials*,

16:062004, 10 2021. ISSN 1748-605X. doi: 10.1088/1748-605X/AC2B7A. URL https://iopscience.iop.org/article/10.1088/1748-605X/ac2b7ahttps://iopscience.iop.org/article/10.1088/1748-605X/ac2b7a/meta.

[41] Holger J. Klein, Richard M. Fakin, Pascal Ducommun, Thomas Giesen, Pietro Giovanoli, and Maurizio Calcagni. Evaluation of cutaneous spatial resolution and pressure threshold secondary to digital nerve repair. *Plastic and Reconstructive Surgery*, 137:1203–1212, 2016. ISSN 00321052. doi: 10.1097/PRS.0000000000002023. URL https://journals.lww.com/plasreconsurg/fulltext/2016/04000/evaluation_of_cutaneous_spatial_resolution_and.20.aspx.

[42] Judith Krotoski, Sidney Weinstein, and Curt Weinstein. Testing sensibility, including touch-pressure, two-point discrimination, point localization, and vibration. *Journal of Hand Therapy*, 6:114–123, 4 1993. ISSN 0894-1130. doi: 10.1016/S0894-1130(12)80292-4.

[43] Aisling Ní Annaidh, Karine Bruyère, Michel Destrade, Michael D. Gilchrist, and Mélanie Ottténio. Characterization of the anisotropic mechanical properties of excised human skin. *Journal of the Mechanical Behavior of Biomedical Materials*, 5:139–148, 1 2012. ISSN 1751-6161. doi: 10.1016/J.JMBBM.2011.08.016.

[44] Krisakorn Khaothong, J C H Goh, and C T Lim. In vivo measurements of the mechanical properties of human skin and muscle by inverse finite element method combined with the indentation test. *IFMBE Proceedings*, 31 IFMBE:1467–1470, 2010. ISSN 1433-9277. doi: 10.1007/978-3-642-14515-5_374. URL https://link.springer.com/chapter/10.1007/978-3-642-14515-5_374.

[45] Y. Zheng and A. F.T. Mak. Effective elastic properties for lower limb soft tissues from manual indentation experiment. *IEEE Transactions on Rehabilitation Engineering*, 7:257–267, 9 1999. ISSN 10636528. doi: 10.1109/86.788463.

[46] Brian Holt, Anubhav Tripathi, and Jeffrey Morgan. Viscoelastic response of human skin to low magnitude physiologically relevant shear. *Journal of biomechanics*, 41:2689, 8 2008. ISSN 00219290. doi: 10.1016/J.JBIOMECH.2008.06.008. URL /pmc/articles/PMC2584606//pmc/articles/PMC2584606/?report=abstracthttps://www.ncbi.nlm.nih.gov/pmc/articles/PMC2584606/.

[47] Cameron H. Parvini, Alexander X. Cartagena-Rivera, and Santiago D. Solares. Viscoelastic parameterization of human skin cells characterize material behavior at multiple timescales. *Communications Biology 2022 5:1*, 5:1–11, 1 2022. ISSN 2399-3642. doi: 10.1038/s42003-021-02959-5. URL https://www.nature.com/articles/s42003-021-02959-5.

[48] Marion Geerligs. Skin layer mechanics. 1 2010. doi: 10.6100/IR657803. URL https://research.tue.nl/en/publications/skin-layer-mechanics.

[49] Mélanie Ottenio, Doris Tran, Aisling Ní Annaidh, Michael D. Gilchrist, and Karine Bruyère. Strain rate and anisotropy effects on the tensile failure characteristics of human skin. *Journal of the Mechanical Behavior of Biomedical Materials*, 41: 241–250, 1 2015. ISSN 1751-6161. doi: 10.1016/J.JMBBM.2014.10.006.

[50] Karen A. Newell. *Wound Closure*, pages 313–341. W.B. Saunders, 2 edition, 1 2007. ISBN 9781416030010. doi: 10.1016/B978-1-4160-3001-0.50027-7.

[51] Sharad P. Paul. Biodynamic excisional skin tension lines for surgical excisions: untangling the science. *Annals of The Royal College of Surgeons of England*, 100:330, 4 2018. ISSN 00358843. doi: 10.1308/RCSANN.2018.0038. URL /pmc/articles/PMC5958865//pmc/articles/PMC5958865/?report=abstracthttps://www.ncbi.nlm.nih.gov/pmc/articles/PMC5958865/.

[52] Davide Deflorio, Massimiliano Di Luca, and Alan M. Wing. Skin and mechanoreceptor contribution to tactile input for perception: A review of simulation models. *Frontiers in Human Neuroscience*, 16:862344, 6 2022. ISSN 16625161. doi: 10.3389/FNHUM.2022.862344/BIBTEX.

[53] Hirotake Yokota, Naofumi Otsuru, Rie Kikuchi, Rinako Suzuki, Sho Kojima, Kei Saito, Shota Miyaguchi, Yasuto Inukai, and Hideaki Onishi. Establishment of optimal two-point discrimination test method and consideration of reproducibility. *Neuroscience Letters*, 714:134525, 1 2020. ISSN 0304-3940. doi: 10.1016/J.NEULET.2019.134525.

[54] Rochelle Ackerley, Ida Carlsson, Henric Wester, Håkan Olausson, and Helena Backlund Wasling. Touch perceptions across skin sites: differences between sensitivity, direction discrimination and pleasantness. *Frontiers in Behavioral Neuroscience*, 8, 2 2014. ISSN 16625153. doi: 10.3389/FNBEH.2014.00054. URL /pmc/articles/PMC3928539//pmc/articles/PMC3928539/?report=abstracthttps://www.ncbi.nlm.nih.gov/pmc/articles/PMC3928539/.

[55] Nicholas D.J. Strzalkowski, Robyn L. Mildren, and Leah R. Bent. Neurophysiology of tactile perception: A tribute to steven hsiao: Thresholds of cutaneous afferents related to perceptual threshold across the human foot sole. *Journal of Neurophysiology*, 114:2144, 8 2015. ISSN 15221598. doi: 10.1152/JN.00524.2015. URL https://www.ncbi.nlm.nih.gov/pmc/articles/PMC4595609/.

[56] Muhammad M. Hussain and Nazek El-Atab, editors. *Handbook of Flexible and Stretchable Electronics*. CRC Press, 2019. ISBN 1138081582.

[57] Robert A Cross. Myosin mechanical ratchet. *Proc Natl Acad Sci USA*, 103(24): 8911, 6 2006. URL http://www.pnas.org/content/103/24/8911.abstract.

[58] R Mcn. Alexander and H C Bennet-Clark. Storage of elastic strain energy in muscle and other tissues. *Nature*, 265(5590):114–117, 1977. URL https://www.scopus.com/inward/record.uri?eid=2-s2.0-0017338764&doi=10.1038%2F265114a0&partnerID=40&md5=1e1abd16ddee92cca4a7a8e6a33940f9. Cited By :466¡br/¿Export Date: 10 May 2020¡br/¿¡br/¿¡br/¿Cited By :466¡br/¿Export Date: 10 May 2020.

[59] Robert Full and Kenneth Meijer. *Metrics of Natural Muscle Function*, chapter Metrics of Natural Muscle Function, pages 73–89. SPIE, 3 2004. doi: 10.1117/3.547465.ch3. URL http://ebooks.spiedigitallibrary.org/content.aspx?doi=10.1117/3.547465.ch3.

[60] Mihai Duduta, Ehsan Hajiesmaili, Huichan Zhao, Robert J. Wood, and David R. Clarke. Realizing the potential of dielectric elastomer artificial muscles. *Proceedings of the National Academy of Sciences of the United States of America*, 116(30679271):2476–2481, February 2019. ISSN 0027-8424. doi: 10.1073/pnas.1815053116. URL https://www.pnas.

org/content/116/7/2476https://www.pnas.org/content/116/7/2476.abstracthttps://www.ncbi.nlm.nih.gov/pmc/articles/PMC6377461/. 30679271[pmid]¡br/¿PMC6377461[pmcid]¡br/¿¡br/¿¡br/¿30679271[pmid]¡br/¿PMC6377461[pmcid

[61] Nicholas P Smith, Christopher J Barclay, and Denis S Loiselle. The efficiency of muscle contraction. *Progress in Biophysics and Molecular Biology*, 88(1):1–58, 2005. ISSN 0079-6107. URL http://www.sciencedirect.com/science/article/pii/S0079610703001081.

[62] Archibald Vivian Hill. The heat of shortening and the dynamic constants of muscle. *Proceedings of the Royal Society of London. Series B - Biological Sciences*, 126(843):136–195, 1938. doi: 10.1098/rspb.1938.0050. URL https://royalsocietypublishing.org/doi/pdf/10.1098/rspb.1938.0050.

[63] Morufu Olusola Ibitoye, Nur Azah Hamzaid, Nazirah Hasnan, Ahmad Khairi Abdul Wahab, and Glen M. Davis. Strategies for rapid muscle fatigue reduction during fes exercise in individuals with spinal cord injury: A systematic review. *PloS one*, 11:e0149024, 2016.

[64] Milos R. Popovic and T. Adam Thrasher. Neuroprostheses. *Encyclopedia of Biomaterials and Biomedical Engineering*, 2004. doi: DOI: 10.1081/E-EBBE120013941. URL http://toronto-fes.ca/publications/2004Popovic.pdf.

[65] Knut Schmidt Nielsen. *Animal Physiology: Adaptation and Environment*. Cambridge University Press, 5 edition, 2002. ISBN 521 57098. URL https://books.google.co.nz/books?id=hcw2AAAAQBAJ&printsec=frontcover&redir_esc=y#v=onepage&q&f=false.

[66] Guangqiang Ma, Xiaojun Wu, Lijin Chen, Xin Tong, and Weiwei Zhao. Characterization and optimization of elastomeric electrodes for dielectric elastomer artificial muscles. *Materials 2020, Vol. 13, Page 5542*, 13(1908508):5542, 12 2020. ISSN 1996-1944. doi: 10.3390/MA13235542. URL https://www.mdpi.com/1996-1944/13/23/5542/htmhttps://www.mdpi.com/1996-1944/13/23/5542.

[67] Daniel Segalman, Walter Witkowski, D Adolf, and Mohsen Shahinpoor. Theory and application of electrically controlled polymeric gels. *Smart Materials and Structures*, 1:95, 1 1999.

[68] Mohsen Shahinpoor. *Ionic Polymer Metal Composites (IPMCs)*. Smart Materials Series. The Royal Society of Chemistry, 2016. ISBN 978-1-78262-720-3.

[69] Masahiro Homma and Yoshio Nakano. Development of electro-driven polymer gel/platinum composite membranes. *Kagaku Kogaku Ronbunshu*, 25(6):1010–1014, 1999. ISSN 13499203. doi: 10.1252/kakoronbunshu.25.1010.

[70] Raymond Liu. In situ electrode formation on a nafion membrane by chemical platinization. *Journal of The Electrochemical Society*, 139(1):15, 1992. ISSN 0013-4651. URL http://dx.doi.org/10.1149/1.2069162.

[71] James D Carrico, Nicklaus W Traeden, Matteo Aureli, and Kam K Leang. Fused filament 3d printing of ionic polymer-metal composites (ipmcs). *Smart Materials and Structures*, 24(12):125021, 11 2015. doi: 10.1088/0964-1726/24/12/125021. URL https://doi.org/10.1088%2F0964-1726%2F24%2F12%2F125021.

[72] Mohsen Shahinpoor and Kwang J. Kim. Ionic polymer-metal composites: Iii. modeling and simulation as biomimetic sensors, actuators, transducers, and artificial muscles. *Smart Materials and Structures*, 13(6):1362–1388, 12 2004. ISSN 09641726. doi: 10.1088/0964-1726/13/6/009. URL https://www.scopus.com/inward/record.uri?eid=2-s2.0-10444275650&doi=10.1088%2f0964-1726%2f13%2f6%2f009&partnerID=40&md5=87202eb3f7394ab27e1da783d00c7386.

[73] Barbar Akle and Donald J. Leo. Electromechanical transduction in multilayer ionic transducers. *Smart Materials and Structures*, 13(5):1081–1089, 10 2004. ISSN 09641726. doi: 10.1088/0964-1726/13/5/014. URL https://www.scopus.com/inward/record.uri?eid=2-s2.0-5744242938&doi=10.1088%2f0964-1726%2f13%2f5%2f014&partnerID=40&md5=65de150f898f2264f18c2ad0633e2f74.

[74] Yan Xu, Gang Zhao, Changshun Ma, and Zhuangzhi Sun. Research on preparation and stacking performance of ipmc. *Journal of Biomimetics, Biomaterials and Biomedical Engineering*, 21(1):45–53, 2014. ISSN 22969845. doi: 10.4028/www.scientific.net/JBBBE.21.45. URL https://www.scopus.com/inward/record.uri?eid=2-s2.0-84906851147&doi=10.4028%2fwww.scientific.net%2fJBBBE.21.45&partnerID=40&md5=ab1a439c97294fbd8d0bcf59ad4d5edb.

[75] Shuxiang Guo, T Fukuda, K Kosuge, F Arai, K Oguro, and M Negoro. Micro catheter system with active guide wire-structure, experimental results and characteristic evaluation of active guide wire catheter using icpf actuator. In *1994 5th International Symposium on Micro Machine and Human Science Proceedings*, page 191, 1994.

[76] Akio Kodaira, Kinji Asaka, Tetsuya Horiuchi, Gen Endo, Hiroyuki Nabae, and Koichi Suzumori. Ipmc monolithic thin film robots fabricated using a multi-layer casting process. *IEEE Robotics and Automation Letters*, 4(2):1335–1342, 4 2019. ISSN 23773766. doi: 10.1109/LRA.2019.2895398.

[77] Yi Chu Chang and Won Jong Kim. Aquatic ionic-polymer-metal-composite insectile robot with multi-dof legs. *IEEE/ASME Transactions on Mechatronics*, 18(2): 547–555, April 2013. ISSN 10834435. doi: 10.1109/TMECH.2012.2210904.

[78] Joel J. Hubbard, Maxwell Fleming, Viljar Palmre, David Pugal, Kwang J. Kim, and Kam K. Leang. Monolithic ipmc fins for propulsion and maneuvering in bioinspired underwater robotics. *IEEE Journal of Oceanic Engineering*, 39(3): 540–551, July 2014. ISSN 03649059. doi: 10.1109/JOE.2013.2259318.

[79] Jasim Khawwaf, Jinchuan Zheng, Hai Wang, and Zhihong Man. Practical model-free robust control design for an underwater ipmc actuator. In *2019 Chinese Control Conference (CCC)*, volume 2019-July, pages 3214–3219. IEEE Computer Society, 7 2019. ISBN 9789881563972. doi: 10.23919/ChiCC.2019.8866467.

[80] E. Acome, S. K. Mitchell, T. G. Morrissey, M. B. Emmett, C. Benjamin, M. King, M. Radakovitz, and C. Keplinger. Hydraulically amplified self-healing electrostatic actuators with muscle-like performance. *Science*, 359(6371):61–65, 1 2018. ISSN 10959203. doi: 10.1126/science.aao6139. URL http://science.sciencemag.org/.

[81] Hyunwoo Yuk, Teng Zhang, German Alberto Parada, Xinyue Liu, and Xuanhe Zhao. Skin-inspired hydrogel-elastomer hybrids with robust interfaces and functional microstructures. *Nature communications*, 7:12028, 6 2016.

[82] Christoph Keplinger, Tiefeng Li, Richard Baumgartner, Zhigang Suo, and Siegfried Bauer. Harnessing snap-through instability in soft dielectrics to achieve giant voltage-triggered deformation. *Soft Matter*, 8(2):285–288, 1 2012. ISSN 1744683X. doi: 10.1039/c1sm06736b. URL www.rsc.org/advances.

[83] Charles Manion, Dinesh Patel, Mark Fuge, and Sarah Bergbrieter. Modeling and evaluation of additive manufacturedhasel actuators. n.d. URL https://softcontrol.mit.edu/sites/default/files/documents/SRMCIROS18_paper_13.pdf.

[84] Shane K Mitchell, Xingrui Wang, Eric Acome, Trent Martin, Khoi Ly, Nicholas Kellaris, Vidyacharan Gopaluni Venkata, and Christoph Keplinger. An easy-to-implement toolkit to create versatile and high-performance hasel actuators for untethered soft robots. *Advanced Science*, 6(14):1900178, 7 2019. ISSN 2198-3844. doi: 10.1002/advs.201900178. URL https://doi.org/10.1002/advs.201900178. doi: 10.1002/advs.201900178.

[85] Mark R Jolly, J David Carlson, Beth C Munoz, and Todd A Bullions. The magnetoviscoelastic response of elastomer composites consisting of ferrous particles embedded in a polymer matrix. *Journal of Intelligent Material Systems and Structures*, 7(6):613–622, 11 1996. ISSN 1045-389X. doi: 10.1177/1045389x9600700601. URL https://doi.org/10.1177/1045389X9600700601. doi: 10.1177/1045389X9600700601.

[86] Holger Bose, Raman Rabindranath, and Johannes Ehrlich. Soft magnetorheological elastomers as new actuators for valves. *Journal of Intelligent Material Systems and Structures*, 23(9):989–994, 1 2012. ISSN 1045-389X. doi: 10.1177/1045389x11433498. URL https://doi.org/10.1177/1045389X11433498. doi: 10.1177/1045389X11433498.

[87] Hannes Krueger, Mohammad Vaezi, and Shoufeng Yang. 3d printing of magnetorheological elastomers(mres)smart materials. volume 0, pages 213–218. Pro-AM, May 2014. ISBN 9789810904463. doi: 10.3850/978-981-09-0446-3_088.

[88] Yakub F. Ismail M. A. Unuh H, Muhamad P and Z. Tanasta. Experimental validation to a prototype magnetorheological (mr) semi-active damper for c-class vehicle. *IJAME*, 16(3):7034–7047, 2019.

[89] Bing Chen, Xuan Zhao, Hao Ma, Ling Qin, and Wei-Hsin Liao. Design and characterization of a magneto-rheological series elastic actuator for a lower extremity exoskeleton. *Smart Materials and Structures*, 26(10):105008, 2017. ISSN 1361-665X. URL http://dx.doi.org/10.1088/1361-665X/aa8343.

[90] Gregory J. Hiemenz, Young Tai Choi, and Norman M. Wereley. Semi-active control of vertical stroking helicopter crew seat for enhanced crashworthiness. *Journal of Aircraft*, 44(3):1031–1034, 5 2007. ISSN 15333868. doi: 10.2514/1.26492. URL https://arc.aiaa.org/doi/abs/10.2514/1.26492.

[91] Yang Liu, Meng Gao, Shengfu Mei, Yanting Han, and Jing Liu. Ultra-compliant liquid metal electrodes with in-plane self-healing capability for dielectric elastomer

actuators. *Applied Physics Letters*, 103:64101, 8 2013. ISSN 0003-6951. URL https://ui.adsabs.harvard.edu/abs/2013ApPhL.103f4101L.

[92] John A Rogers. A clear advance in soft actuators. *Science*, 341:968–969, 8 2013. ISSN 0036-8075. URL https://ui.adsabs.harvard.edu/abs/2013Sci...341..968R.

[93] A Bele, C Tugui, M Asandulesa, D Ionita, L Vasiliu, G Stiubianu, M Iacob, C Racles, and M Cazacu. Conductive stretchable composites properly engineered to develop highly compliant electrodes for dielectric elastomer actuators. *Smart Materials and Structures*, 27(105005), 2018. URL https://www.scopus.com/inward/record.uri?eid=2-s2.0-85054609457&doi=10.1088%2F1361-665X%2Faad977&partnerID=40&md5=37f280185c3e3f3c2bf1196fd522e256. Cited By :1 Export Date: 8 May 2020.

[94] Jose Enrico Q Quinsaat, Mihaela Alexandru, Frank A Nuesch, Heinrich Hofmann, Andreas Borgschulte, and Dorina M Opris. Highly stretchable dielectric elastomer composites containing high volume fractions of silver nanoparticles. *Journal of Materials Chemistry A*, 3(28):14675–14685, 2015. ISSN 2050-7488. URL http://dx.doi.org/10.1039/C5TA03122B.

[95] S. Hau, G. Rizzello, and S. Seelecke. A novel dielectric elastomer membrane actuator concept for high-force applications. *Extreme Mechanics Letters*, 23:24–28, 2018. ISSN 2352-4316. URL http://www.sciencedirect.com/science/article/pii/S2352431618301019.

[96] G. Kovacs, L. During, S. Michel, and G. Terrasi. Stacked dielectric elastomer actuator for tensile force transmission. *Sensors and Actuators A: Physical*, 155(2):299–307, 2009. ISSN 0924-4247. URL http://www.sciencedirect.com/science/article/pii/S0924424709004002.

[97] F. Carpi and D. De Rossi. Small-strain modeling of helical dielectric elastomer actuators. *IEEE/ASME Transactions on Mechatronics*, 17(5706367):318–325, 2012. URL https://www.scopus.com/inward/record.uri?eid=2-s2.0-84856316362&doi=10.1109%2fTMECH.2010.2100403&partnerID=40&md5=8aa3bd1f53656c405a8280ab884c829f.

[98] S. Pfeil, K. Katzer, A. Kanan, J. Mersch, M. Zimmermann, M. Kaliske, and G. Gerlach. A biomimetic fish fin-like robot based on textile reinforced silicone. *Micromachines*, 11(298):1–16, 2020. URL https://www.scopus.com/inward/record.uri?eid=2-s2.0-85082725099&doi=10.3390%2fmi11030298&partnerID=40&md5=db2d25c45e87089b0ce501ad2e885d2a.

[99] M. Ghilardi, H. Boys, P. Torok, J. J. C. Busfield, and F. Carpi. Smart lenses with electrically tuneable astigmatism. *Scientific Reports*, 9(16127), 2019. URL https://www.scopus.com/inward/record.uri?eid=2-s2.0-85074625641&doi=10.1038%2fs41598-019-52168-8&partnerID=40&md5=8fc861d90be73fbb8e0c212a2800ca84.

[100] H. Amin and S. F. M. Assal. Design methodology of a spring roll dielectric elastomer-based actuator for a hand rehabilitation system. In *2018 IEEE International Conference on Mechatronics and Automation (ICMA)*, pages 997–1002, 2018.

[101] J. H. Park, A. El Atrache, D. Kim, and E. Divo. Optimization of helical dielectric elastomer actuator with additive manufacturing. volume 10594, 2018. URL https://www.scopus.com/inward/record.uri?eid=2-s2.0-85050800758&doi=10.1117%2f12.2296720&partnerID=40&md5=89fe2bcddc403d953bb74c5cee2acad0.

[102] David McCoul, Samuel Rosset, Samuel Schlatter, and Herbert Shea. Inkjet 3d printing of uv and thermal cure silicone elastomers for dielectric elastomer actuators. *Smart Materials and Structures*, 26(12):125022, 2017. ISSN 1361665X. doi: 10.1088/1361-665X/aa9695. URL http://dx.doi.org/10.1088/1361-665X/aa9695.

[103] K. Jung, K. J. Kim, and H. R. Choi. A self-sensing dielectric elastomer actuator. *Sensors and Actuators, A: Physical*, 143(2):343–351, 2008. URL https://www.scopus.com/inward/record.uri?eid=2-s2.0-41349085167&doi=10.1016%2fj.sna.2007.10.076&partnerID=40&md5=93777dd3b85b4884763060bebeab2b4b.

[104] N. C. Goulbourne, E. M. Mockensturm, and M. I. Frecker. Electro-elastomers: Large deformation analysis of silicone membranes. *International Journal of Solids and Structures*, 44(9):2609–2626, 2007. ISSN 0020-7683. URL http://www.sciencedirect.com/science/article/pii/S002076830600312X.

[105] Lei Sun, Shuwen Jiang, Yao Xiao, and Wanli Zhang. Realization of flexible pressure sensor based on conductive polymer composite via using electrical impedance tomography. *Smart Materials and Structures*, 29:055004, 3 2020. ISSN 0964-1726. doi: 10.1088/1361-665X/AB75A3. URL https://iopscience-iop-org.ezproxy.canterbury.ac.nz/article/10.1088/1361-665X/ab75a3https://iopscience-iop-org.ezproxy.canterbury.ac.nz/article/10.1088/1361-665X/ab75a3/meta.

[106] Yun Lu, Weina He, Tai Cao, Haitao Guo, Yongyi Zhang, Qingwen Li, Ziqiang Shao, Yulin Cui, and Xuetong Zhang. Elastic, conductive, polymeric hydrogels and sponges. *Scientific Reports 2014 4:1*, 4:1–8, 7 2014. ISSN 2045-2322. doi: 10.1038/srep05792. URL https://www.nature.com/articles/srep05792.

[107] Michael E. Spahr, Raffaele Gilardi, and Daniele Bonacchi. *Carbon Black for Electrically Conductive Polymer Applications*, pages 375–400. Springer, Cham, 2017. doi: 10.1007/978-3-319-28117-9_32. URL https://link.springer.com/referenceworkentry/10.1007/978-3-319-28117-9_32.

[108] Patricia Hazelton, Mengguang Ye, and Xianfeng Chen. *Introduction to Conducting Polymers*. 2023. doi: 10.1021/bk-2023-1438.ch001. URL https://pubs.acs.org/sharingguidelines.

[109] Yong Lae Park, Carmel Majidi, Rebecca Kramer, Phillipe Brard, and Robert J. Wood. Hyperelastic pressure sensing with a liquid-embedded elastomer. *Journal of Micromechanics and Microengineering*, 20:125029, 11 2010. ISSN 0960-1317. doi: 10.1088/0960-1317/20/12/125029. URL https://iopscience.iop.org/article/10.1088/0960-1317/20/12/125029https://iopscience.iop.org/article/10.1088/0960-1317/20/12/125029/meta.

[110] Taekeon Jung and Sung Yang. Highly stable liquid metal-based pressure sensor integrated with a microfluidic channel. *Sensors 2015, Vol. 15, Pages*

11823-11835, 15:11823–11835, 5 2015. ISSN 1424-8220. doi: 10.3390/S150511823. URL https://www.mdpi.com/1424-8220/15/5/11823/htmhttps://www.mdpi.com/1424-8220/15/5/11823.

[111] Daehan Kim, Sung Hwan Kim, and Joong Yull Park. Floating-on-water fabrication method for thin polydimethylsiloxane membranes. *Polymers*, 11:1264, 8 2019. ISSN 20734360. doi: 10.3390/polym11081264. URL /pmc/articles/PMC6722912/?report=abstracthttps://www.ncbi.nlm.nih.gov/pmc/articles/PMC6722912/.

[112] K. Park, H. Yuk, M. Yang, J. Cho, H. Lee, and J. Kim. A biomimetic elastomeric robot skin using electrical impedance and acoustic tomography for tactile sensing. *Science Robotics*, 7:7187, 6 2022. ISSN 24709476. doi: 10.1126/SCIROBOTICS.ABM7187/SUPPL_FILE/SCIROBOTICS.ABM7187_MOVIES_S1_TO_S4.ZIP. URL https://www.science.org/doi/10.1126/scirobotics.abm7187.

[113] Haofeng Chen, Xuanxuan Yang, Jialu Geng, Gang Ma, and Xiaojie Wang. A skin-like hydrogel for distributed force sensing using an electrical impedance tomography-based pseudo-array method. *ACS Applied Electronic Materials*, 3 2023. ISSN 2637-6113. doi: 10.1021/ACSAELM.2C01394. URL https://pubs.acs.org/doi/abs/10.1021/acsaelm.2c01394.

[114] Shuoyan Xu, Zigan Xu, Ding Li, Tianrui Cui, Xin Li, Yi Yang, Houfang Liu, and Tianling Ren. Recent advances in flexible piezoresistive arrays: Materials, design, and applications. *Polymers 2023, Vol. 15, Page 2699*, 15:2699, 6 2023. ISSN 2073-4360. doi: 10.3390/POLYM15122699. URL https://www.mdpi.com/2073-4360/15/12/2699/htmhttps://www.mdpi.com/2073-4360/15/12/2699.

[115] Kyoseung Sim, Zhoulyu Rao, Zhanan Zou, Faheem Ershad, Jianming Lei, Anish Thukral, Jie Chen, Qing An Huang, Jianliang Xiao, and Cunjiang Yu. Metal oxide semiconductor nanomembrane-based soft unnoticeable multifunctional electronics for wearable human-machine interfaces. *Science advances*, 5, 8 2019. ISSN 2375-2548. doi: 10.1126/SCIADV.AAV9653. URL https://pubmed.ncbi.nlm.nih.gov/31414044/.

[116] Youcan Yan, Zhe Hu, Zhengbao Yang, Wenzhen Yuan, Chaoyang Song, Jia Pan, and Yajing Shen. Soft magnetic skin for super-resolution tactile sensing with force self-decoupling. *Science Robotics*, 6:8801, 2 2021. ISSN 24709476. doi: 10.1126/SCIROBOTICS.ABC8801/SUPPL_FILE/ABC8801_SM.PDF. URL https://www.science.org/doi/10.1126/scirobotics.abc8801.

[117] Gihun Lee, Hyunjin Kim, and Inkyu Park. A mini review of recent advances in optical pressure sensor. *Journal of Sensor Science and Technology*, 32:22–30, 2023. ISSN pISSN 1225-5475/eISSN 2093-7563. doi: http://dx.doi.org/10.46670/JSST.2023.32.1.22.

[118] Dana Hughes and Nikolaus Correll. Texture recognition and localization in amorphous robotic skin. *Bioinspiration Biomimetics*, 10:055002, 9 2015. ISSN 1748-3190. doi: 10.1088/1748-3190/10/5/055002. URL https://iopscience.iop.org/article/10.1088/1748-3190/10/5/055002https://iopscience.iop.org/article/10.1088/1748-3190/10/5/055002/meta.

[119] Di Wu, Mengni Wei, Rong Li, Tao Xiao, Shen Gong, Zhu Xiao, Zhenghong Zhu, and Zhou Li. A percolation network model to predict the electrical

property of flexible cnt/pdms composite films fabricated by spin coating technique. *Composites Part B: Engineering*, 174:107034, 2019. ISSN 13598368. doi: 10.1016/j.compositesb.2019.107034.

[120] L. Flandin, J. Y. Cavaille, Y. Brechet, and R. Dendievel. Characterization of the damage in nanocomposite materials by a.c. electrical properties: experiment and simulation. *Journal of Materials Science*, 34:1753–1759, 4 1999. ISSN 1573-4803. doi: 10.1023/A:1004546806226. URL https://link.springer.com/article/10.1023/A:1004546806226.

[121] Hwa Kim, Kwangsik Park, and Moo Yeol Lee. Biocompatible dispersion methods for carbon black. *Toxicological Research*, 28:209, 12 2012. ISSN 19768257. doi: 10.5487/TR.2012.28.4.209. URL /pmc/articles/PMC3834425//pmc/articles/PMC3834425/?report=abstracthttps://www.ncbi.nlm.nih.gov/pmc/articles/PMC3834425/.

[122] Sven Pegel, Petra Pötschke, Gudrun Petzold, Ingo Alig, Sergej M. Dudkin, and Dirk Lellinger. Dispersion, agglomeration, and network formation of multiwalled carbon nanotubes in polycarbonate melts. *Polymer*, 49:974–984, 2 2008. ISSN 0032-3861. doi: 10.1016/J.POLYMER.2007.12.024.

[123] Pan Song and Yong Zhang. Vertically aligned carbon nanotubes/graphene/cellulose nanofiber networks for enhancing electrical conductivity and piezoresistivity of silicone rubber composites. *Composites Science and Technology*, 222:109366, 5 2022. ISSN 0266-3538. doi: 10.1016/J.COMPSCITECH.2022.109366.

[124] Melika Eklund and Nellie Kjäll. Silicone-based carbon black composite for epidermal electrodes. 12 2019. URL http://uu.diva-portal.org/smash/get/diva2:1384429/FULLTEXT02.pdf.

[125] Yuanzhen Wang, Chensheng Xu, Timotheus Jahnke, Wolfgang Verestek, Siegfried Schmauder, and Joachim P. Spatz. Microstructural modeling and simulation of a carbon black-based conductive polymera template for the virtual design of a composite material. *ACS Omega*, 7:28820–28830, 8 2022. ISSN 24701343. doi: 10.1021/ACSOMEGA.2C01755/ASSET/IMAGES/LARGE/AO2C01755_0009.JPEG. URL https://pubs.acs.org/doi/full/10.1021/acsomega.2c01755.

[126] R. Neffati and J. M.C. Brokken-Zijp. Electric conductivity in silicone-carbon black nanocomposites: percolation and variable range hopping on a fractal. *Materials Research Express*, 6:125058, 11 2019. ISSN 2053-1591. doi: 10.1088/2053-1591/AB58FD. URL https://iopscience.iop.org/article/10.1088/2053-1591/ab58fdhttps://iopscience.iop.org/article/10.1088/2053-1591/ab58fd/meta.

[127] D. Bloor, A. Graham, E. J. Williams, P. J. Laughlin, and D. Lussey. Metal-polymer composite with nanostructured filler particles and amplified physical properties. *Applied Physics Letters*, 88:102103, 3 2006. ISSN 00036951. doi: 10.1063/1.2183359/902621. URL /aip/apl/article/88/10/102103/902621/Metal-polymer-composite-with-nanostructured-filler.

[128] Lingyan Duan, Sirui Fu, Hua Deng, Qin Zhang, Ke Wang, Feng Chen, and Qiang Fu. The resistivity–strain behavior of conductive polymer composites: stability and sensitivity. *Journal of Materials Chemistry A*, 2:17085–17098, 9 2014. ISSN 2050-7496. doi: 10.1039/C4TA03645J. URL https://pubs.rsc.org/en/content/articlehtml/2014/ta/c4ta03645jhttps://pubs.rsc.org/en/content/articlelanding/2014/ta/c4ta03645j.

[129] Rui Zhang, Mark Baxendale, and Ton Peijs. Universal resistivity-strain dependence of carbon nanotube/polymer composites. *Physical Review B - Condensed Matter and Materials Physics*, 76:195433, 11 2007. ISSN 10980121. doi: 10.1103/PHYSREVB.76.195433/FIGURES/6/MEDIUM. URL https://journals.aps.org/prb/abstract/10.1103/PhysRevB.76.195433.

[130] Leonel P. Madrid, Carlos A. Palacio, Arnaldo Matute, and Carlos A. Parra Vargas. Underlying physics of conductive polymer composites and force sensing resistors (fsrs) under static loading conditions. *Sensors (Basel, Switzerland)*, 17, 9 2017. ISSN 14248220. doi: 10.3390/S17092108. URL /pmc/articles/PMC5621037//pmc/articles/PMC5621037/?report=abstracthttps://www.ncbi.nlm.nih.gov/pmc/articles/PMC5621037/.

[131] Ning Hu, Yoshifumi Karube, Cheng Yan, Zen Masuda, and Hisao Fukunaga. Tunneling effect in a polymer/carbon nanotube nanocomposite strain sensor. *Acta Materialia*, 56:2929–2936, 8 2008. ISSN 1359-6454. doi: 10.1016/J.ACTAMAT.2008.02.030.

[132] C. Grimaldi and I. Balberg. Tunneling and nonuniversality in continuum percolation systems. *Physical Review Letters*, 96:066602, 2 2006. ISSN 10797114. doi: 10.1103/PHYSREVLETT.96.066602/FIGURES/2/MEDIUM. URL https://journals.aps.org/prl/abstract/10.1103/PhysRevLett.96.066602.

[133] M Lacasse, V Duchaine, and C Gosselin. Characterization of the electrical resistance of carbon-black-filled silicone: Application to a flexible and stretchable robot skin. pages 4842–4848, 5 2010. doi: 10.1109/ROBOT.2010.5509283.

[134] Jeong Hun Kim, Ji Young Hwang, Ha Ryeon Hwang, Han Seop Kim, Joong Hoon Lee, Jae Won Seo, Ueon Sang Shin, and Sang Hoon Lee. Simple and cost-effective method of highly conductive and elastic carbon nanotube/polydimethylsiloxane composite for wearable electronics. *Scientific Reports*, 8:54853, 12 2018. ISSN 20452322. doi: 10.1038/s41598-017-18209-w. URL www.nature.com/scientificreports.

[135] E. F.M. Henke, Katherine E. Wilson, and I. A. Anderson. Modeling of dielectric elastomer oscillators for soft biomimetic applications. *Bioinspiration and Biomimetics*, 13:046009, 6 2018. ISSN 17483190. doi: 10.1088/1748-3190/aac911. URL https://doi.org/10.1088/1748-3190/aac911.

[136] Yanju Liu, Liwu Liu, Zhen Zhang, and Jinsong Leng. Dielectric elastomer film actuators: Characterization, experiment and analysis. *Smart Materials and Structures*, 18:095024, 7 2009. ISSN 09641726. doi: 10.1088/0964-1726/18/9/095024. URL https://iopscience-iop-org.ezproxy.canterbury.ac.nz/article/10.1088/0964-1726/18/9/095024https://iopscience-iop-org.ezproxy.canterbury.ac.nz/article/10.1088/0964-1726/18/9/095024/meta.

[137] Federico Carpi, Stanisa Raspopovic, Gabriele Frediani, and Danilo De Rossi. Real-time control of dielectric elastomer actuators via bioelectric and biomechanical signals. *Polymer International*, 59:422–429, 3 2010. ISSN 09598103. doi: 10.1002/pi.2757. URL http://doi.wiley.com/10.1002/pi.2757.

[138] Yasuhiro Mouri, Yuta Murai, Yoshiko Yabuki, Takumi Kato, Hideki Ohmae, Yoshihiro Tomita, Shunta Togo, Yinlai Jiang, and Hiroshi Yokoi. Development of new flexible dry electrode for myoelectric sensor using conductive silicone. pages 478–482. Institute of Electrical and Electronics Engineers Inc., 1 2019. ISBN 9781538673553. doi: 10.1109/CBS.2018.8612280. URL https://ieeexplore-ieee-org.ezproxy.canterbury.ac.nz/document/8612280.

[139] S. L. Wang, P. Wang, and T. H. Ding. Development of wireless compressive/relaxation-stress measurement system integrated with pressure-sensitive carbon black-filled silicone rubber-based sensors. *Sensors and Actuators, A: Physical*, 157:36–41, 1 2010. ISSN 09244247. doi: 10.1016/j.sna.2009.11.037.

[140] Dinesh Maddipatla, Binu B. Narakathu, Mohammed M. Ali, Amer A. Chlaihawi, and Massood Z. Atashbar. Development of a novel carbon nanotube based printed and flexible pressure sensor. Institute of Electrical and Electronics Engineers Inc., 4 2017. ISBN 9781509032020. doi: 10.1109/SAS.2017.7894034.

[141] Luheng Wang and Yanyan Han. Compressive relaxation of the stress and resistance for carbon nanotube filled silicone rubber composite. *Composites Part A: Applied Science and Manufacturing*, 47:63–71, 4 2013. ISSN 1359835X. doi: 10.1016/j.compositesa.2012.11.018.

[142] C Racles, M Asandulesa, V Tiron, C Tugui, N Vornicu, Ciubotaru B, M Mičušík, M Omastova, A Vasiliu, and C Ciomaga. Elastic composites with pdms matrix and polysulfone-supported silver nanoparticles as filler. *Polymer*, 217, 3 2021. URL https://www-scopus-com.ezproxy.canterbury.ac.nz/record/display.uri?eid=2-s2.0-85100376139&origin=resultslist&sort=plf-f&src=s&st1=&st2=&sid=f91c46950ff68c208c50319781176f3e&sot=b&sdt=b&sl=37&s=TITLE-ABS-KEY+%28metal+silicone+sensor%29&relpos=4&citeCnt=0&s.

[143] Shoji Fukushima, Tatsuya Kasai, Yumi Umeda, Makoto Ohnishi, Toshiaki Sasaki, and Michiharu Matsumoto. Carcinogenicity of multi-walled carbon nanotubes: Challenging issue on hazard assessment. *Journal of Occupational Health*, 60:10–30, 2018. ISSN 13489585. doi: 10.1539/joh.17-0102-RA. URL /pmc/articles/PMC5799097//pmc/articles/PMC5799097/?report=abstracthttps://www.ncbi.nlm.nih.gov/pmc/articles/PMC5799097/.

[144] Zannatul Ferdous and Abderrahim Nemmar. Health impact of silver nanoparticles: A review of the biodistribution and toxicity following various routes of exposure. *International Journal of Molecular Sciences*, 21, 4 2020. ISSN 14220067. doi: 10.3390/ijms21072375. URL /pmc/articles/PMC7177798//pmc/articles/PMC7177798/?report=abstracthttps://www.ncbi.nlm.nih.gov/pmc/articles/PMC7177798/.

[145] L. J. Rausch, E. C. Bisinger, and A. Sharma. Carbon black should not be classified as a human carcinogen based on rodent bioassay data. *Regulatory Toxicology and Pharmacology*, 40:28–41, 8 2004. ISSN 02732300. doi: 10.1016/j.yrtph.2004.04.004.

[146] Tim Giffney, Estelle Bejanin, Agee S. Kurian, Jadranka Travas-Sejdic, and Kean Aw. Highly stretchable printed strain sensors using multi-walled carbon nanotube/silicone rubber composites. *Sensors and Actuators, A: Physical*, 259:44–49, 6 2017. ISSN 09244247. doi: 10.1016/j.sna.2017.03.005.

[147] Harish Devaraj, Tim Giffney, Adeline Petit, Mahtab Assadian, and Kean Aw. The development of highly flexible stretch sensors for a robotic hand. *Robotics*, 7, 9 2018. ISSN 22186581. doi: 10.3390/robotics7030054.

[148] J Kost, A Foux, and M Narkis. Quantitative model relating electrical resistance, strain, and time for carbon black loaded silicone rubber - proquest. *Polymer Engineering and Science*, 34:1628, 11 1994. ISSN 00323888. URL https://search-proquest-com.ezproxy.canterbury.ac.nz/docview/218606740/citation/EA6C174C0ED84FDAPQ/1?accountid=14499.

[149] Peng Wang, Feng Xu, Ding Tianhuai, and Qin Yuanzhen. Time dependence of electrical resistivity under uniaxial pressures for carbon black-/polymer composites. *Journal of Materials Science*, 39:4937–4939, 2004. URL http://search.proquest.com.ezproxy.canterbury.ac.nz/docview/2259673740?accountid=14499. ¡b¿From Duplicate 4 (¡i¿Time dependence of electrical resistivity under uniaxial pressures for carbon black/polymer composites¡/i¿ - Wang, Peng; Xu, Feng; Tianhuai, Ding; Yuanzhen, Qin)¡br/¿¡/b¿¡br/¿Copyright - Journal of Materials Science is a copyright of Springer, (2004). All Rights Reserved; Last updated - 2019-07-19.

[150] SmoothOn. Dragon skin™ 10 nv product information — smooth-on, inc., 2 2021. URL https://www.smooth-on.com/products/dragon-skin-10-nv/.

[151] ASTM. D412-16 standard test methods for vulcanized rubber and thermoplastic elastomers—tension, 2020. URL https://compass.astm.org/EDIT/html_annot.cgi?D412+16.

[152] VishayPG. Strain gage selection: Criteria, procedures, recommendations - tech note, 5 2018. URL www.micro-measurements.com.

[153] Hui Xu, Li Xiu Gong, Xu Wang, Li Zhao, Yong Bing Pei, Gang Wang, Ya Jun Liu, Lian Bin Wu, Jian Xiong Jiang, and Long Cheng Tang. Influence of processing conditions on dispersion, electrical and mechanical properties of graphene-filled-silicone rubber composites. *Composites Part A: Applied Science and Manufacturing*, 91:53–64, 12 2016. ISSN 1359835X. doi: 10.1016/j.compositesa.2016.09.011.

[154] Laura Wegener Parfrey, Daniel J.G. Lahr, Andrew H. Knoll, and Laura A. Katz. Estimating the timing of early eukaryotic diversification with multigene molecular clocks. *Proceedings of the National Academy of Sciences of the United States of America*, 108:13624–13629, 8 2011. ISSN 00278424. doi: 10.1073/PNAS.1110633108/-/DCSUPPLEMENTAL. URL /pmc/articles/PMC3158185//pmc/articles/PMC3158185/?report=abstracthttps://www.ncbi.nlm.nih.gov/pmc/articles/PMC3158185/.

[155] Kamkim Andre and Irina Kiseleva. *Mechanosensitivity of the Nervous System*. Springer Dordrecht, 1 edition, 9 2008. ISBN 978-1-4020-8716-5.

[156] Charles Molnar and Jane Gair. *Somatosensation*. OpenTextBC, 1 edition, 2015. ISBN 978-1-989623-99-2. URL https://opentextbc.ca/biology/chapter/17-2-somatosensation/.

[157] Richard Ellingham and Tim Giffney. Stress and resistance relaxation for carbon nanoparticle silicone rubber composite large-strain sensors. *Volume 7: 17th IEEE/ASME International Conference on Mechatronic and Embedded Systems and Applications (MESA)*, 11 2021. doi: 10.1115/DETC2021-69206. URL https://asmedigitalcollection.asme.org/IDETC-CIE/proceedings/IDETC-CIE2021/85437/V007T07A046/1128153.

[158] B. F. Gonçalves, J. Oliveira, P. Costa, V. Correia, P. Martins, G. Botelho, and S. Lanceros-Mendez. Development of water-based printable piezoresistive sensors for large strain applications. *Composites Part B: Engineering*, 112:344–352, 3 2017. ISSN 1359-8368. doi: 10.1016/J.COMPOSITESB.2016.12.047.

[159] Philipp Loew, Marius Brill, Gianluca Rizzello, and Stefan Seelecke. Development of a nonintrusive pressure sensor for polymer tubes based on dielectric elastomer membranes. *Sensors and Actuators A: Physical*, 292:1–10, 6 2019. ISSN 0924-4247. doi: 10.1016/J.SNA.2019.03.006.

[160] David Silvera-Tawil, David Rye, Manuchehr Soleimani, and Mari Velonaki. Electrical impedance tomography for artificial sensitive robotic skin: A review. *IEEE Sensors Journal*, 15:2001–2016, 4 2015. doi: 10.1109/JSEN.2014.2375346.

[161] Jaehyuk Lee, Jaehyung Kim, Yujin Shin, and Inhwa Jung. Ultra-robust wide-range pressure sensor with fast response based on polyurethane foam doubly coated with conformal silicone rubber and cnt/tpu nanocomposites islands. *Composites Part B: Engineering*, 177:107364, 11 2019. ISSN 1359-8368. doi: 10.1016/J.COMPOSITESB.2019.107364.

[162] Golezar Gilanizadehdizaj, Kean C. Aw, Jonathan Stringer, and Debes Bhattacharyya. Facile fabrication of flexible piezo-resistive pressure sensor array using reduced graphene oxide foam and silicone elastomer. *Sensors and Actuators A: Physical*, 340:113549, 6 2022. ISSN 0924-4247. doi: 10.1016/J.SNA.2022.113549.

[163] Yuting Zhu, Kean Aw, and Tim Giffney. Dielectric elastomer-based multi-location capacitive sensor. pages 84–95, 12 2021. URL https://researchspace.auckland.ac.nz/handle/2292/60603.

[164] Richard Bayford. *Basic Electrical Impedance Tomography*, pages 29–44. Springer, Cham, 3 2018. doi: 10.1007/978-3-319-74388-2_3. URL https://link-springer-com.ezproxy.canterbury.ac.nz/chapter/10.1007/978-3-319-74388-2_3.

[165] William R. B. Lionheart. Eit reconstruction algorithms: Pitfalls, challenges and recent developments. *Physiological Measurement*, 25:125–142, 10 2003. doi: 10.1088/0967-3334/25/1/021. URL http://arxiv.org/abs/physics/0310151http://dx.doi.org/10.1088/0967-3334/25/1/021.

[166] Thiago de Castro Martins, André Kubagawa Sato, Fernando Silva de Moura, Erick Dario León Bueno de Camargo, Olavo Luppi Silva, Talles Batista Rattis Santos, Zhanqi Zhao, Knut Möeller, Marcelo Brito Passos Amato, Jennifer L. Mueller, Raul Gonzalez Lima, and Marcos de Sales Guerra Tsuzuki. A review of electrical impedance tomography in lung applications: Theory and algorithms for absolute images. *Annual Reviews in Control*, 48:442–471, 1 2019. ISSN 1367-5788. doi: 10.1016/J.ARCONTROL.2019.05.002.

[167] Andy Adler and David Holder. *Electrical Impedance Tomography*. CRC Press, 2 edition, 11 2021. ISBN 9780429399886. doi: 10.1201/9780429399886.

[168] Andy Adler, John H. Arnold, Richard Bayford, Andrea Borsic, Brian Brown, Paul Dixon, Theo J.C. Faes, Inéz Frerichs, Hervé Gagnon, Yvo Gärber, Bartłomiej Grychtol, Günter Hahn, William R.B. Lionheart, Anjum Malik, Robert P. Patterson, Janet Stocks, Andrew Tizzard, Norbert Weiler, and Gerhard K. Wolf. Greit: a unified approach to 2d linear eit reconstruction of lung images. *Physiological measurement*, 30, 2009. ISSN 0967-3334. doi: 10.1088/0967-3334/30/6/S03. URL https://pubmed.ncbi.nlm.nih.gov/19491438/.

[169] Francesco Visentin, Paolo Fiorini, and Kenji Suzuki. A deformable smart skin for continuous sensing based on electrical impedance tomography. *Sensors 2016, Vol. 16, Page 1928*, 16:1928, 11 2016. ISSN 1424-8220. doi: 10.3390/S16111928. URL https://www.mdpi.com/1424-8220/16/11/1928/htmhttps://www.mdpi.com/1424-8220/16/11/1928.

[170] Tyler N. Tallman and Danny J. Smyl. Structural health and condition monitoring via electrical impedance tomography in self-sensing materials: a review. *Smart Materials and Structures*, 29:123001, 10 2020. ISSN 0964-1726. doi: 10.1088/1361-665X/ABB352. URL https://iopscience.iop.org/article/10.1088/1361-665X/abb352https://iopscience.iop.org/article/10.1088/1361-665X/abb352/meta.

[171] Alirezaei Hassan, Akihiko Nagakubo, and Yasuo Kuniyoshi. A tactile distribution sensor which enables stable measurement under high and dynamic stretch. *3DUI - IEEE Symposium on 3D User Interfaces 2009 - Proceedings*, pages 87–93, 2009. doi: 10.1109/3DUI.2009.4811210.

[172] Yo Kato, Toshiharu Mukai, Tomonori Hayakawa, and Tetsuyoshi Shibata. Tactile sensor without wire and sensing element in the tactile region based on eit method. *Proceedings of IEEE Sensors*, pages 792–795, 2007. doi: 10.1109/ICSENS.2007.4388519.

[173] Marc Ramuz, Benjamin C.K. Tee, Jeffrey B.H. Tok, and Zhenan Bao. Transparent, optical, pressure-sensitive artificial skin for large-area stretchable electronics. *Advanced Materials*, 24:3223–3227, 6 2012. ISSN 1521-4095. doi: 10.1002/ADMA.201200523. URL https://onlinelibrary.wiley.com/doi/full/10.1002/adma.201200523https://onlinelibrary.wiley.com/doi/abs/10.1002/adma.201200523https://onlinelibrary.wiley.com/doi/10.1002/adma.201200523.

[174] Sho Shimadera, Kei Kitagawa, Koyo Sagehashi, Yoji Miyajima, Tomoaki Niiyama, and Satoshi Sunada. Speckle-based high-resolution multimodal soft sensing. *Scientific Reports 2022 12:1*, 12:1–11, 7 2022. ISSN 2045-2322. doi: 10.1038/s41598-022-17026-0. URL https://www.nature.com/articles/s41598-022-17026-0.

[175] Jonathan Rossiter and Toshiharu Mukai. A novel tactile sensor using a matrix of leds operating in both photoemitter and photodetector modes. *Proceedings of IEEE Sensors*, 2005:994–997, 2005. doi: 10.1109/ICSENS.2005.1597869.

[176] Ya Fei Fu, Feng Lian Yi, Jin Rui Liu, Yuan Qing Li, Ze Yu Wang, Gang Yang, Pei Huang, Ning Hu, and Shao Yun Fu. Super soft but strong e-skin based on

carbon fiber/carbon black/silicone composite: Truly mimicking tactile sensing and mechanical behavior of human skin. *Composites Science and Technology*, 186: 107910, 1 2020. ISSN 0266-3538. doi: 10.1016/J.COMPSCITECH.2019.107910.

[177] Kun Yang, Xinkai Xia, Fan Zhang, Huanzhou Ma, Shengbo Sang, Qiang Zhang, and Jianlong Ji. Implementation of a sponge-based flexible electronic skin for safe human–robot interaction. *Micromachines*, 13:1344, 8 2022. ISSN 2072666X. doi: 10.3390/MI13081344/S1. URL https://www.mdpi.com/2072-666X/13/8/1344/htmhttps://www.mdpi.com/2072-666X/13/8/1344.

[178] Guanhao Liang, Yancheng Wang, Deqing Mei, Kailun Xi, and Zichen Chen. Flexible capacitive tactile sensor array with truncated pyramids as dielectric layer for three-axis force measurement. *Journal of Microelectromechanical Systems*, 24: 1510–1519, 10 2015. ISSN 10577157. doi: 10.1109/JMEMS.2015.2418095.

[179] R.A. Knight and R.T. Lipczynski. The use of eit techniques to measure interface pressure. pages 2307–2308. Institute of Electrical and Electronics Engineers (IEEE), 8 1990. doi: 10.1109/IEMBS.1990.692299. URL https://doi-org.ezproxy.canterbury.ac.nz/10.1109/IEMBS.1990.692299.

[180] Akihiko Nagakubo, Hassan Alirezaei, and Yasuo Kuniyoshi. A deformable and deformation sensitive tactile distribution sensor. *2007 IEEE International Conference on Robotics and Biomimetics, ROBIO*, pages 1301–1308, 2007. doi: 10.1109/ROBIO.2007.4522352.

[181] Stefania Russo, Samia Nefti-Meziani, Nicola Carbonaro, and Alessandro Tognetti. A quantitative evaluation of drive pattern selection for optimizing eit-based stretchable sensors. *Sensors*, 17, 2017. doi: 10.3390/s17091999. URL www.mdpi.com/journal/sensors.

[182] Sang Ho Yoon, Ke Huo, Yunbo Zhang, Guiming Chen, Luis Paredes, Subramanian Chidambaram, and Karthik Ramani. isoft: A customizable soft sensor with real-time continuous contact and stretching sensing. *Proceedings of the 30th Annual ACM Symposium on User Interface Software and Technology*, pages 665–678, 10 2017. doi: 10.1145/3126594. URL https://doi.org/10.1145/3126594.3126654.

[183] Niccolo Biasi, Andrea Gargano, Lucia Arcarisi, Nicola Carbonaro, and Alessandro Tognetti. Physics-based simulation and machine learning for the practical implementation of eit-based tactile sensors. *IEEE Sensors Journal*, 2022. ISSN 15581748. doi: 10.1109/JSEN.2022.3144038.

[184] Panagiotis E. Chatzistergos, David Allan, Nachiappan Chockalingam, and Roozbeh Naemi. Shore hardness is a more representative measurement of bulk tissue biomechanics than of skin biomechanics. *Medical Engineering Physics*, 105: 103816, 7 2022. ISSN 1350-4533. doi: 10.1016/J.MEDENGPHY.2022.103816.

[185] Barry McDermott, Brian McGinley, Katarzyna Krukiewicz, Brendan Divilly, Marggie Jones, Manus Biggs, Martin O'Halloran, and Emily Porter. Stable tissue-mimicking materials and an anatomically realistic, adjustable head phantom for electrical impedance tomography. *Biomedical Physics Engineering Express*, 4:015003, 11 2017. ISSN 2057-1976. doi: 10.1088/2057-1976/AA922D. URL https://iopscience.iop.org/article/10.1088/2057-1976/aa922dhttps://iopscience.iop.org/article/10.1088/2057-1976/aa922d/meta.

[186] Matthew E. D'Asaro, Michael S. Otten, Stephanie Chen, and Jeffrey H. Lang. Multidimensional characterization of piezoresistive carbon black silicone rubber composites. *Journal of Applied Polymer Science*, 134, 5 2017. ISSN 10974628. doi: 10.1002/app.44773. URL http://doi.wiley.com/10.1002/app.44773.

[187] Shuying Shang, Yujuan Yue, and Xiaoer Wang. Piezoresistive strain sensing of carbon black /silicone composites above percolation threshold. *Review of Scientific Instruments*, 87:123910, 12 2016. ISSN 10897623. doi: 10.1063/1.4973274/916719. URL /aip/rsi/article/87/12/123910/916719/Piezoresistive-strain-sensing-of-carbon-black.

[188] Shuai Dong and Xiaojie Wang. Alignment of carbon iron into polydimethylsiloxane to create conductive composite with low percolation threshold and high piezoresistivity: experiment and simulation. *Smart Materials and Structures*, 26:045027, 3 2017. ISSN 0964-1726. doi: 10.1088/1361-665X/AA62D2. URL https://iopscience-iop-org.ezproxy.canterbury.ac.nz/article/10.1088/1361-665X/aa62d2https://iopscience-iop-org.ezproxy.canterbury.ac.nz/article/10.1088/1361-665X/aa62d2/meta.

[189] Heng Yang, Lin Hui Gong, Zhong Zheng, and Xue Feng Yao. Highly stretchable and sensitive conductive rubber composites with tunable piezoresistivity for motion detection and flexible electrodes. *Carbon*, 158:893–903, 2020. ISSN 0008-6223. doi: https://doi.org/10.1016/j.carbon.2019.11.079. URL http://www.sciencedirect.com/science/article/pii/S0008622319312126.

[190] Yu Cheng Ju, Donyau Chiang, Ming Yen Tsai, Hao Ouyang, and Sanboh Lee. Stress relaxation behavior of poly(methyl methacrylate)/graphene composites: Ultraviolet irradiation. *Polymers*, 14, 10 2022. ISSN 20734360. doi: 10.3390/POLYM14194192/S1.

[191] Junhui Zhao, Kun Dai, Chenggang Liu, Guoqiang Zheng, Bo Wang, Chuntai Liu, Jingbo Chen, and Changyu Shen. A comparison between strain sensing behaviors of carbon black/polypropylene and carbon nanotubes/polypropylene electrically conductive composites. *Composites Part A: Applied Science and Manufacturing*, 48:129–136, 5 2013. ISSN 1359-835X. doi: 10.1016/J.COMPOSITESA.2013.01.004.

[192] Shailesh Vidhate, Jaycee Chung, Vijay Vaidyanathan, and Nandika Anne D'Souza. Resistive–conductive transitions in the time-dependent piezoresponse of pvdf-mwcnt nanocomposites. *Polymer Journal 2010 42:7*, 42:567–574, 5 2010. ISSN 1349-0540. doi: 10.1038/pj.2010.44. URL https://www.nature.com/articles/pj201044.

[193] D. H. Griffiths and R. D. Barker. Two-dimensional resistivity imaging and modelling in areas of complex geology. *Journal of Applied Geophysics*, 29:211–226, 4 1993. ISSN 09269851. doi: 10.1016/0926-9851(93)90005-J.

[194] Liangqi Yuan, Student Member, Yuan Wei, Jia Li, and Senior Member. Smart pressure e-mat for human sleeping posture and dynamic activity recognition. *arxiv*, 5 2023. URL https://arxiv.org/abs/2305.11367v1.

[195] Samuel Rosset, Oluwaseun A. Ararom, Samuel Schlatter, and Herbert R. Shea. Fabrication process of silicone-based dielectric elastomer actuators. *Journal of*

Visualized Experiments, page 53423, 2 2016. ISSN 1940087X. doi: 10.3791/53423. URL www.jove.comurl:https://www.jove.com/video/53423.

[196] Ehsan Hajiesmaili and David R. Clarke. Dielectric elastomer actuators. *Journal of Applied Physics*, 129:151102, 4 2021. ISSN 0021-8979. doi: 10.1063/5.0043959. URL https://aip-scitation-org.ezproxy.canterbury.ac.nz/doi/abs/10.1063/5.0043959.

[197] Yaguang Guo, Liwu Liu, Yanju Liu, and Jinsong Leng. Review of dielectric elastomer actuators and their applications in soft robots. *Advanced Intelligent Systems*, 3:2000282, 10 2021. ISSN 2640-4567. doi: 10.1002/AISY.202000282. URL https://onlinelibrary.wiley.com/doi/full/10.1002/aisy.202000282https://onlinelibrary.wiley.com/doi/abs/10.1002/aisy.202000282https://onlinelibrary.wiley.com/doi/10.1002/aisy.202000282.

[198] William H McKnight and Wayne C. McGinnis. Energy-harvesting device using electrostrictive polymers, 1 2002. URL http://www.patentbuddy.com/Patent/6433465.

[199] Federico Carpi, Danilo De Rossi, Roy Kornbluh, Ronald Pelrine, and Peter Sommer-Larsen. Dielectric elastomers as electromechanical transducers: Fundamentals, materials, devices, models and applications of an emerging electroactive polymer technology. *Dielectric Elastomers as Electromechanical Transducers*, page 329, 7 2008. doi: 10.1016/B978-0-08-047488-5.X0001-9. URL http://www.sciencedirect.com:5070/book/9780080474885/dielectric-elastomers-as-electromechanical-transducers.

[200] Soo Jin Adrian Koh, Xuanhe Zhao, and Zhigang Suo. Maximal energy that can be converted by a dielectric elastomer generator. *Applied Physics Letters*, 94, 2009. URL http://imechanica.org/files/MaximalEnergyAPL.pdf.

[201] Guggi Kofod, Peter Sommer-Larsen, Roy Kornbluh, and Ron Pelrine. Actuation response of polyacrylate dielectric elastomers. *http://dx.doi.org/10.1177/104538903039260*, 14:787–793, 12 2003. ISSN 1045389X. doi: 10.1177/104538903039260. URL https://journals.sagepub.com/doi/10.1177/104538903039260.

[202] Hyouk Ryeol Choi, Kwangmok Jung, Nguyen Huu Chuc, Minyoung Jung, Igmo Koo, Jachoon Koo, Joonho Lee, Jonghoon Lee, Jaedo Nam, Misuk Cho, Youngkwan Lee, Hyouk Ryeol Choi, Kwangmok Jung, Nguyen Huu Chuc, Minyoung Jung, Igmo Koo, Jachoon Koo, Joonho Lee, Jonghoon Lee, Jaedo Nam, Misuk Cho, and Youngkwan Lee. Effects of prestrain on behavior of dielectric elastomer actuator. *Proceedings of the SPIE*, 5759:283–291, 5 2005. ISSN 0277-786X. doi: 10.1117/12.599363. URL https://ui.adsabs.harvard.edu/abs/2005SPIE.5759..283C/abstract.

[203] Michael Wissler and Edoardo Mazza. Electromechanical coupling in dielectric elastomer actuators. *Sensors and Actuators A: Physical*, 138:384–393, 8 2007. ISSN 0924-4247. doi: 10.1016/J.SNA.2007.05.029.

[204] Yunwei Mao and Lallit Anand. Fracture of elastomeric materials by crosslink failure. *Journal of Applied Mechanics, Transactions ASME*, 85, 8 2018. ISSN 15289036. doi: 10.1115/1.4040100.

[205] Huichan Zhao, Aftab M. Hussain, Mihai Duduta, Daniel M. Vogt, Robert J. Wood, and David R. Clarke. Compact dielectric elastomer linear actuators. *Advanced Functional Materials*, 28, 10 2018. ISSN 1616301X. doi: 10.1002/adfm.201804328. URL http://doi.wiley.com/10.1002/adfm.201804328.

[206] P ; Thummala, L ; Huang, Z ; Zhang, and M A E Andersen. Analysis of dielectric electro active polymer actuator and its high voltage driving circuits. *Proceedings of the International Power Modulator Symposium and High Voltage Workshop*, 2012. doi: 10.1109/IPMHVC.2012.6518779. URL https://doi.org/10.1109/IPMHVC.2012.6518779.

[207] Chongjing Cao and Andrew T. Conn. Performance optimization of a conical dielectric elastomer actuator. *Actuators*, 7:32, 6 2018. ISSN 2076-0825. doi: 10.3390/act7020032. URL http://www.mdpi.com/2076-0825/7/2/32.

[208] Krunal Koshiya, Sebastian Gratz-Kelly, Paul Motzki, and Gianluca Rizzello. An embedded self-sensing motion control system for a strip-shaped dielectric elastomer actuators. volume 12482, pages 147–155. SPIE, 4 2023. ISBN 9781510660717. doi: 10.1117/12.2657131. URL https://www.spiedigitallibrary.org/conference-proceedings-of-spie/12482/124820I/An-embedded-self-sensing-motion-control-system-for-a-strip/10.1117/12.2657131.fullhttps://www.spiedigitallibrary.org/conference-proceedings-of-spie/12482/124820I/An-embedded-self-sensing-motion-control-system-for-a-strip/10.1117/12.2657131.short.

[209] Canh Toan Nguyen, Hoa Phung, Tien Dat Nguyen, Hosang Jung, and Hyouk Ryeol Choi. Multiple-degrees-of-freedom dielectric elastomer actuators for soft printable hexapod robot. *Sensors and Actuators A: Physical*, 267:505–516, 11 2017. ISSN 0924-4247. doi: 10.1016/J.SNA.2017.10.010.

[210] Yang Zhang, Yong Huang, Wenjie Sun, Hang Jin, Jinhui Zhang, Lida Xu, Shuai Dong, Zhenjin Xu, Bin Zhu, Jinrong Li, and Dezhi Wu. A multi-electrode electroelastomer cylindrical actuator for multimodal locomotion and its modeling. *International Journal of Mechanical Sciences*, 266:108964, 3 2024. ISSN 0020-7403. doi: 10.1016/J.IJMECSCI.2024.108964.

[211] Jiang Zou, Shakiru Olajide Kassim, Jieji Ren, Vahid Vaziri, Sumeet S. Aphale, and Guoying Gu. A generalized motion control framework of dielectric elastomer actuators: Dynamic modeling, sliding-mode control and experimental evaluation. *IEEE Transactions on Robotics*, 2023. ISSN 19410468. doi: 10.1109/TRO.2023.3338973.

[212] Qibing Pei, Marcus Rosenthal, Scott Stanford, Harsha Prahlad, and Ron Pelrine. Multiple-degrees-of-freedom electroelastomer roll actuators. *Smart Materials and Structures*, 13:N86, 9 2004. ISSN 0964-1726. doi: 10.1088/0964-1726/13/5/N03. URL https://iopscience.iop.org/article/10.1088/0964-1726/13/5/N03https://iopscience.iop.org/article/10.1088/0964-1726/13/5/N03/meta.

[213] Federico Carpi, Iain Anderson, Siegfried Bauer, Gabriele Frediani, Giuseppe Gallone, Massimiliano Gei, Christian Graaf, Claire Jean-Mistral, William Kaal, Guggi Kofod, Matthias Kollosche, Roy Kornbluh, Benny Lassen, Marc

Matysek, Silvain Michel, Stephan Nowak, Benjamin O'Brien, Qibing Pei, Ron Pelrine, Björn Rechenbach, Samuel Rosset, and Herbert Shea. Standards for dielectric elastomer transducers. *Smart Materials and Structures*, 24:105025, 9 2015. ISSN 0964-1726. doi: 10.1088/0964-1726/24/10/105025. URL https://iopscience.iop.org/article/10.1088/0964-1726/24/10/105025https://iopscience.iop.org/article/10.1088/0964-1726/24/10/105025/meta.

[214] Jianjian Huang, Fang Wang, Li Ma, Zhiqiang Zhang, Erchao Meng, Chao Zeng, Hao Zhang, and Dongjie Guo. Vinylsilane-rich silicone filled by polydimethylsiloxane encapsulated carbon black particles for dielectric elastomer actuator with enhanced out-of-plane actuations. *Chemical Engineering Journal*, 428:131354, 1 2022. ISSN 1385-8947. doi: 10.1016/J.CEJ.2021.131354.

[215] Hiroki Shigemune, Shigeki Sugano, Jun Nishitani, Masayuki Yamauchi, Naoki Hosoya, Shuji Hashimoto, and Shingo Maeda. Dielectric elastomer actuators with carbon nanotube electrodes painted with a soft brush. *Actuators*, 7:51, 8 2018. ISSN 2076-0825. doi: 10.3390/ACT7030051. URL https://www.mdpi.com/2076-0825/7/3/51/htmhttps://www.mdpi.com/2076-0825/7/3/51.

[216] Leipeng Liu, Yanfei Huang, Yihe Zhang, Elshad Allahyarov, Zhongbo Zhang, Fengzhu Lv, and Lei Zhu. Understanding reversible maxwellian electroactuation in a 3m vhb dielectric elastomer with prestrain. *Polymer*, 144:150–158, 5 2018. ISSN 0032-3861. doi: 10.1016/J.POLYMER.2018.04.048.

[217] Alexander Helal, Marc Doumit, and Robert Shaheen. Biaxial experimental and analytical characterization of a dielectric elastomer. *Applied Physics A: Materials Science and Processing*, 124:1–11, 1 2018. ISSN 14320630. doi: 10.1007/S00339-017-1422-3/TABLES/3. URL https://link.springer.com/article/10.1007/s00339-017-1422-3.

[218] Deng Pan and Adrian Koh Soo Jin. Uniaxial prestretch dependence of dielectric permittivity in polyacrylate elastomers, 7 2015. URL http://dengpan.ca/reports/vhb.pdf.

[219] Federico Carpi, Piero Chiarelli, Alberto Mazzoldi, and Danilo De Rossi. Electromechanical characterisation of dielectric elastomer planar actuators: comparative evaluation of different electrode materials and different counterloads. *Sensors and Actuators A: Physical*, 107:85–95, 10 2003. ISSN 0924-4247. doi: 10.1016/S0924-4247(03)00257-7.

[220] Florian M. Weiss, Frederikke B. Madsen, Tino Töpper, Bekim Osmani, Vanessa Leung, and Bert Müller. Molecular beam deposition of high-permittivity polydimethylsiloxane for nanometer-thin elastomer films in dielectric actuators. *Materials and Design*, 105:106–113, 2016. ISSN 18734197. doi: 10.1016/j.matdes.2016.05.049.

[221] Musthafa O. Mavukkandy, Samantha A. McBride, David M. Warsinger, Nadir Dizge, Shadi W. Hasan, and Hassan A. Arafat. Thin film deposition techniques for polymeric membranes– a review. *Journal of Membrane Science*, 610:118258, 9 2020. ISSN 18733123. doi: 10.1016/j.memsci.2020.118258.

[222] Julie Diani, Bruno Fayolle, and Pierre Gilormini. A review on the mullins effect. *European Polymer Journal*, 45:601–612, 3 2009. ISSN 0014-3057. doi: 10.1016/J.EURPOLYMJ.2008.11.017.

[223] Junshi Zhang, Lei Liu, and Hualing Chen. Electromechanical properties of soft dissipative dielectric elastomer actuators influenced by electrode thickness and conductivity. *Journal of Applied Physics*, 127:184902, 5 2020. ISSN 10897550. doi: 10.1063/5.0001580/280844. URL /aip/jap/article/127/18/184902/280844/Electromechanical-properties-of-soft-dissipative.

[224] Neil Savage. Squishy power generators - ieee spectrum. *IEEE Spectrum*, 12 2012. URL https://spectrum.ieee.org/squishy-power-generators.

[225] COMSOL. Comsol multiphysics, 2022.

[226] Ivica Smolic and Bruno Klajn. Capacitance matrix revisited. *Progress in Electromagnetics Research B*, 92:1–18, 3 2021. URL https://www.jpier.org/ac_api/download.php?id=21011501.

[227] Catherine Redmond. Winning the battle against latch-up in cmos analog switches. *ADI Analog Dialogue*, 10 2001. URL https://analog.com/media/en/analog-dialogue/volume-35/number-1/articles/winning-the-battle-against-latchup.pdf.

[228] Sunjoo Hong, Kwonjoon Lee, Unsoo Ha, Hyunki Kim, Yongsu Lee, Youchang Kim, and Hoi Jun Yoo. A 4.9 m-sensitivity mobile electrical impedance tomography ic for early breast-cancer detection system. *IEEE Journal of Solid-State Circuits*, 50: 245–257, 1 2015. ISSN 00189200. doi: 10.1109/JSSC.2014.2355835.

[229] Jaehyuk Lee, Surin Gweon, Kwonjoon Lee, Soyeon Um, Kyoung Rog Lee, Kwantae Kim, Jihee Lee, and Hoi Jun Yoo. A 9.6 mw/ch 10 mhz wide-bandwidth electrical impedance tomography ic with accurate phase compensation for breast cancer detection. *Proceedings of the Custom Integrated Circuits Conference*, 2020-March, 3 2020. ISSN 08865930. doi: 10.1109/CICC48029.2020.9075950. URL https://doaj.org/article/2c43b707327d45f8b141ee0b6dbe3433.

[230] Yang Li, Nan Wang, Li Feng Fan, Peng Fei Zhao, Jin Hai Li, Lan Huang, and Zhong Yi Wang. Robust electrical impedance tomography for biological application: A mini review. *Heliyon*, 9:e15195, 4 2023. ISSN 2405-8440. doi: 10.1016/J.HELIYON.2023.E15195.

[231] Ji Hoon Suh, Haidam Choi, Yoontae Jung, Sein Oh, Hyungjoo Cho, Nahmil Koo, Seong Joong Kim, Chisung Bae, Sohmyung Ha, and Minkyu Je. A synchronous-sampling impedance-readout ic with baseline-cancellation-based two-step conversion for fast neural electrical impedance tomography. *2022 IEEE Asian Solid-State Circuits Conference, A-SSCC 2022 - Proceedings*, 2022. doi: 10.1109/A-SSCC56115.2022.9980820.

[232] Yang Zhang and Chris Harrison. Tomo. volume 119, pages 167–173. Association for Computing Machinery (ACM), 11 2015. ISBN 9781450337793. doi: 10.1145/2807442.2807480. URL https://dl.acm.org/doi/10.1145/2807442.2807480.

[233] Yang Zhang, Junhan Zhou, Gierad Laput, and Chris Harrison. Skintrack: Using the body as an electrical waveguide for continuous finger tracking on the skin. *Conference on Human Factors in Computing Systems - Proceedings*, pages 1491–1503, 5 2016. doi: 10.1145/2858036.2858082. URL https://dl.acm.org/doi/10.1145/2858036.2858082.

[234] Yang Zhang, Gierad Laput, and Chris Harrison. Electrick: Low-cost touch sensing using electric field tomography. volume 2017-May, pages 1–14. Association for Computing Machinery, 5 2017. ISBN 9781450346559. doi: 10.1145/3025453.3025842. URL https://dl.acm.org/doi/10.1145/3025453.3025842.

[235] David Silvera Tawil, David Rye, and Mari Velonaki. Improved image reconstruction for an eit-based sensitive skin with multiple internal electrodes. *IEEE Transactions on Robotics*, 27:425–435, 6 2011. ISSN 15523098. doi: 10.1109/TRO.2011.2125310.

[236] Hua Xu, Shixong Zhang, Steven M. Anlage, Liangbing Hu, and George Grüner. Frequency- and electric-field-dependent conductivity of single-walled carbon nanotube networks of varying density. *Physical Review B - Condensed Matter and Materials Physics*, 77:075418, 2 2008. ISSN 10980121. doi: 10.1103/PHYSREVB.77.075418/FIGURES/6/MEDIUM. URL https://journals.aps.org/prb/abstract/10.1103/PhysRevB.77.075418.

[237] T. L. Rodgers and A. Kowalski. An electrical resistance tomography method for determining mixing in batch addition with a level change. *Chemical Engineering Research and Design*, 88:204–212, 2 2010. ISSN 0263-8762. doi: 10.1016/J.CHERD.2009.08.003.

[238] F. Lux. Models proposed to explain the electrical conductivity of mixtures made of conductive and insulating materials, 1 1993. ISSN 00222461.

[239] Francisco Zamora-Arellano, Oscar Roberto López-Bonilla, Enrique Efrén García-Guerrero, Jesús Everardo Olguín-Tiznado, Everardo Inzunza-González, Didier López-Mancilla, and Esteban Tlelo-Cuautle. Development of a portable, reliable and low-cost electrical impedance tomography system using an embedded system. *Electronics 2021, Vol. 10, Page 15*, 10:15, 12 2020. doi: 10.3390/ELECTRONICS10010015. URL https://www.mdpi.com/2079-9292/10/1/15/htmhttps://www.mdpi.com/2079-9292/10/1/15.

[240] Zainab Husain, Nadya Abdel Madjid, and Panos Liatsis. Tactile sensing using machine learning-driven electrical impedance tomography. *IEEE Sensors Journal*, 21:11628–11642, 5 2021. ISSN 15581748. doi: 10.1109/JSEN.2021.3054870.

[241] David Sherry, Archie McCulloch, Qing Liang, al, Jian Wu, Pranav Garg, Suxing Pan, Andy Adler, and William R B Lionheart. Uses and abuses of eidors: an extensible software base for eit. *Physiological Measurement*, 27:S25, 4 2006. ISSN 0967-3334. doi: 10.1088/0967-3334/27/5/S03. URL https://iopscience-iop-org.ezproxy.canterbury.ac.nz/article/10.1088/0967-3334/27/5/S03https://iopscience-iop-org.ezproxy.canterbury.ac.nz/article/10.1088/0967-3334/27/5/S03/meta.

[242] Tianhuai Ding, Luheng Wang, and Peng Wang. Changes in electrical resistance of carbon-black-filled silicone rubber composite during compression. *Journal of Polymer Science Part B: Polymer Physics*, 45:2700–2706, 10 2007. ISSN 08876266. doi: 10.1002/polb.21272. URL http://doi.wiley.com/10.1002/polb.21272.

[243] Andriy Buketov, Serhii Smetankin, Eduard Lysenkov, Kyrylo Yurenin, Oleksandr Akimov, Serhii Yakushchenko, and Iryna Lysenkova. Electrophysical properties of epoxy composite materials filled with carbon black nanopowder. *Advances in*

Materials Science and Engineering, 2020, 2020. ISSN 16878442. doi: 10.1155/2020/6361485.

[244] John H. Zhang, Andre Obenaus, David S. Liebeskind, Jiping Tang, Richard Hartman, and William J. Pearce. Recanalization, reperfusion, and recirculation in stroke. *Journal of Cerebral Blood Flow and Metabolism*, 37:3818–3823, 2017. ISSN 15597016. doi: 10.1177/0271678X17732695.